



Title	UV photocatalysis with aluminum nanoparticles
Author(s)	本田, 光裕
Citation	大阪大学, 2014, 博士論文
Version Type	VoR
URL	<a href="https://doi.org/10.18910/34458">https://doi.org/10.18910/34458</a>
rights	
Note	

*The University of Osaka Institutional Knowledge Archive : OUKA*

<https://ir.library.osaka-u.ac.jp/>

The University of Osaka

Doctoral Dissertation

UV photocatalysis with aluminum  
nanoparticles

Mitsuhiro Honda

December 2013

Graduate School of Engineering,  
Osaka University

# Contents

## Introduction

### Chapter 1. Photocatalysis

- 1.1 Titanium dioxide
- 1.2 Photocatalysis on titanium dioxide
- 1.3 Enhancement of photocatalysis

### Chapter 2. Plasmonic nanoparticle

- 2.1 Localized surface plasmon
- 2.2 Nanoscale heating by plasmonic nanoparticles
- 2.3 Aluminum as a plasmonic material in UV range

### Chapter 3. Photocatalysis with aluminum nanoparticles

- 3.1 Nanosphere lithography
- 3.2 Rate equation in photocatalysis
- 3.3 Experiment of photocatalysis with aluminum nanoparticles
- 3.4 Photocatalysis with and without aluminum nanoparticles
- 3.5 Irradiation wavelength dependence and enhancement mechanism

### Chapter 4. Oblique angle deposition for aluminum nanoparticles

- 4.1 The method of oblique angle deposition
- 4.2 Experiment
- 4.3 Discussion of experimental results: Effects by near-field and multiple scattering

## Conclusion

## List of publications

## Acknowledgements

## Introduction

The concept of my research is to keep the light staying at the surface of photocatalyst. Since the reaction of the photocatalysis concentrate only at the surface, the efficiency becomes the highest when all the incident light is confined at the surface. It has been known that the light is localized in the vicinity of metal nanoparticles. Based on this idea, I propose to enhance photocatalysis. (See Figure 1)

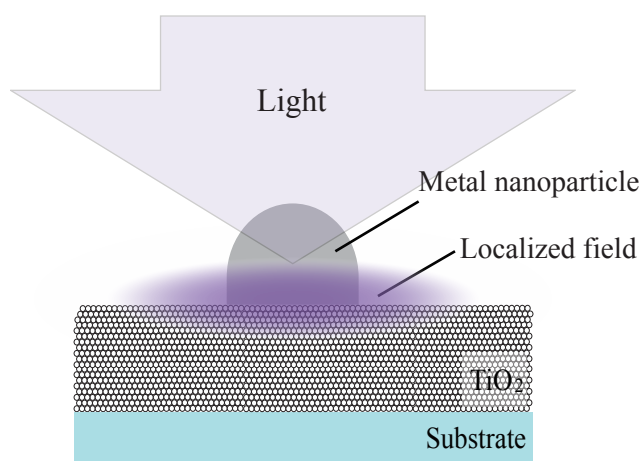


Figure 1 Concept of my research. Photocatalysis is enhanced because the light is trapped at the surface of  $\text{TiO}_2$  owing to the metallic nanoparticle.

UV Photocatalysis is a function to chemically harness the energy from the UV light. A photocatalyst traps photons to generate electron-hole pairs and subsequently induce chemical reactions at the surface. Titanium dioxide ( $\text{TiO}_2$ ) is the most common photocatalyst, which has been already used in our daily life owing to its strong redox power as well as physical and chemical stability, low cost and safety toward both human and environment. For example, toxic organic compounds can be decomposed into small compounds, e.g.  $\text{CO}_2$  and  $\text{H}_2\text{O}$ . Hydrogen is produced from water as a clean and renewable energy. Therefore, the field of UV photocatalysis

is an important research area that could provide fundamental solutions to many of green- and energy-related problems facing humankind.

The earliest work of photocatalysis on  $\text{TiO}_2$  is decomposition of dyes ("chlorazol sky blue") reported in 1938 by Goodeve and Kitchener. In order to measure the photocatalytic activity, the quantum yield was also determined in the report. After that, they proposed photo-induced oxidation as the mechanism of photocatalysis. Because the development of photocatalysis shifted to zinc oxide and CdS for the purpose of getting higher activity, the study on  $\text{TiO}_2$  fell behind until the 1950s. In 1972, A. Fujishuima and K. Honda reported the generation of hydrogen from water. Because of the historical background, oil crisis in the 1970s,  $\text{TiO}_2$  and photo-electrochemical behavior came under the spotlight, and accordingly predominant number of studies related to photocatalysis were reported. In 1977, A.J. Bard et al. developed a system for hydrogen generation by supporting platinum onto  $\text{TiO}_2$ .

Photocatalysis on  $\text{TiO}_2$  has been tried to use in a variety of environmental applications such as self-cleaning surface, disinfection, and air purification. In order to make it a practical solution for many of green- and energy issues, the activity of photocatalysis needs to be improved. There are two ways for improvement of photocatalysis. One is efficient generation of electron-hole pairs. For example, the sensitivity of  $\text{TiO}_2$  is shifted to the visible region because the sunlight has more photons in visible range than in UV range. The other is efficient use of the generated electrons and holes. Supporting Pt on  $\text{TiO}_2$  and decreasing defects in  $\text{TiO}_2$  suppress the recombination of electron-hole pairs, and consequently improved the efficiency.

My approach is utilizing localized surface plasmons (LSPs) for storing UV light at the surface of  $\text{TiO}_2$ . Because reactions induced by photocatalysis occur at the surface of  $\text{TiO}_2$ , the energy of the light absorbed at the deeper part of  $\text{TiO}_2$  is hardly used for photocatalysis. When a plasmonic metal nanoparticle is placed at the surface of  $\text{TiO}_2$ , energy of incident light localized at the surface as shown in Figure 1. As a result, with utilizing LSP, the energy of UV light is more likely to induce photocatalytic reactions in photocatalysis.

I use aluminum as a plasmonic material for the enhanced photocatalysis. In the past, typical materials used for plasmonics are noble metals (Ag, Au, Cu) because of small energy losses. However those metals does not exhibit plasmonic property in UV range. Recently poor metals are found to exhibit plasmonic property in UV range. Aluminum works as a plasmonic material in UV range judging from its dielectric function. In addition to the fact, aluminum is protected

from surrounding environment due to immediate oxidation of its surface. Furthermore, plenty of aluminum exists in the earth, and aluminum is friendly to human and easier to handling than other poor metals.

In this dissertation, I discuss enhancement of UV photocatalysis on TiO<sub>2</sub>. Firstly I confirmed the enhancement of photocatalysis with using aluminum nanoparticles. Al nanostructures were fabricated on a TiO<sub>2</sub> layer by nanosphere lithography technique. After that, observation of photocatalysis with and without aluminum nanoparticles was conducted through monitoring the absorbance of methylene blue applied on the TiO<sub>2</sub>. The size and irradiation wavelength dependence were observed. To discuss the enhancement mechanism, simulations by discrete dipole approximation (DDA) method for aluminum nanoparticles were conducted. Finally, Oblique angle deposition of Al was employed to increase enhanced area.

## References

- [1] S. Kawata, Y. Inouye, P. Verma, "Plasmonics for near-field nano-imaging and superlensing", *Nature Photonics* 3, 388 (2009)
- [2] M. Ni, M.K.H. Leung, D.Y.C. Leung, K. Sumathy, "A review and recent developments in photocatalytic water-splitting using TiO<sub>2</sub> for hydrogen production", *Renewable and Sustainable Energy Reviews*, 11, 401–425 (2007)
- [3] A.L. Linsebigler, G. Lu, J.T. Yates, "Photocatalysis on TiO<sub>2</sub> Surfaces: Principles, Mechanisms, and Selected Results", *Chem. Rev.*, 95, 3, 735–758 (1995)
- [4] K. Hashimoto, H. Irie and A. Fujishima, "TiO<sub>2</sub> Photocatalysis: A Historical Overview and Future Prospects", *Jpn. J. Appl. Phys.*, 44, 8269-8285 (2005)
- [5] A. Fujishima, T.N. Rao, D.A. Tryk, "Titanium dioxide photocatalysis", *Journal of Photochemistry and Photobiology C: Photochemistry Reviews*, 1, 1–21 (2000)
- [6] S. Hamad, C.R.A. Catlow, and S.M. Woodley, S. Lago, J.A. Mejías, "Structure and Stability of Small TiO<sub>2</sub> Nanoparticles", *J. Phys. Chem. B*, 109, 33, 15741–15748 (2005)
- [7] A. Wold, "Photocatalytic properties of titanium dioxide (TiO<sub>2</sub>)", *Chem. Mater.*, 5, 3, 280–283 (1993)
- [8] R.W. Matthews, "Kinetics of photocatalytic oxidation of organic solutes over titanium

- dioxide", *Journal of Catalysis*, 111, 2, 264–272 (1988)
- [9] K. Maeda and K. Domen, "Photocatalytic Water Splitting: Recent Progress and Future Challenges", *J. Phys. Chem. Lett.*, 1, 18, 2655–2661 (2010)
- [10] K. Maeda, K. Teramura, D. Lu, T. Takata, N. Saito, Yasunobu Inoue and Kazunari Domen, "Photocatalyst releasing hydrogen from water", *Nature* 440, 295 (2006)
- [11] C.F. Goodeve, J. A. Kitchener, "Photosensitisation by titanium dioxide", *Trans. Faraday Soc.*, 34, 570-579 (1938)
- [12] C.F. Goodeve, J.A. Kitchener, "The mechanism of photosensitisation by solids", *Trans. Faraday Soc.*, 34, 902–908. (1938)
- [13] R.E. Stephens, B. Ke, D. Trivich, "The Efficiencies of Some Solids as Catalysts for the Photosynthesis of Hydrogen Peroxide", *J. Phys. Chem.*, 59, 966–969 (1955)
- [14] A. Fujishima, K. Honda, "Electrochemical Photolysis of Water at a Semiconductor Electrode", *Nature* 238, 37–38 (1972)
- [15] A. Fujishima, X. Zhang, D.A. Tryk, "TiO<sub>2</sub> photocatalysis and related surface phenomena", *Surface Science Reports*, 63, 515–582 (2008)
- [16] S.N. Frank, A.J. Bard, "Heterogeneous photocatalytic oxidation of cyanide ion in aqueous solutions at titanium dioxide powder", *J. Am. Chem. Soc.* 99, 303–304 (1977)
- [17] S.N. Frank, A.J. Bard, "Heterogeneous photocatalytic oxidation of cyanide and sulfite in aqueous solutions at semiconductor powders", *J. Phys. Chem.* 81, 1484–1488 (1977)
- [18] M.R. Hoffmann, S.T. Martin, W. Choi, D.W. Bahnemann, "Environmental Applications of Semiconductor Photocatalysis", *Chem. Rev.*, 95, 1, 69–96 (1995)
- [19] S. Kawata, "Plasmonics: Future Outlook", *Jpn. J. of Appl. Phys.*, 52, 010001 (2013)
- [20] J.M. McMahon, G.C. Schatz, S.K. Gray, "Plasmonics in the ultraviolet with the poor metals Al, Ga, In, Sn, Tl, Pb, and Bi", *Phys. Chem. Chem. Phys.*, 15, 5415 (2013)
- [21] C. Langhammer, M. Schwind, B. Kasemo, I. Zorić, "Localized Surface Plasmon Resonances in Aluminum Nanodisks", *Nano Lett.*, 2008, 8, 5, 1461–1471 (2008)

# Chapter 1. Photocatalysis

Titanium dioxide ( $\text{TiO}_2$ ) is the most common photocatalyst for practical applications. This chapter introduces the fundamental properties of  $\text{TiO}_2$ , the mechanism of photocatalytic reaction, and its importance in environmental applications. At last in this chapter, past studies on enhancement of the photocatalytic activity are described.

## 1.1 Titanium dioxide

The crystal phases of  $\text{TiO}_2$  are categorized into three, that is, anatase, rutile and brookite. [1] Generally, anatase and rutile structures are used as photocatalyst. [2] Figure 1-1 shows the unit cell of anatase and rutile phases. In the unit cell of both, one titanium atom is surrounded by six oxygen atoms.

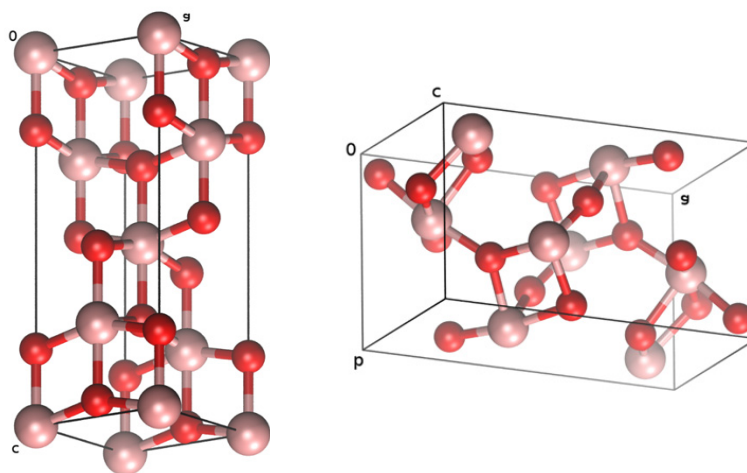


**Figure 1-1.** Crystal structures of anatase (left) and rutile (right) phases.

Pink and red spheres mean titanium and oxygen atoms, respectively. [2]

The crystal structures of rutile and anatase are tetragonal. Anatase has more asymmetric

structure than rutile because the distance of Ti-Ti and Ti-O bonds in anatase is shorter and longer than those in rutile, respectively. Anatase phase starts to transform into the rutile phase by annealing at 550 °C. [3] Figure 1-2 shows the electronic density of states of anatase TiO<sub>2</sub>. [6] Ti and O have electronic structures of [Ar]3d<sup>2</sup> 4s<sup>2</sup> and [He]2s<sup>2</sup> 2p<sup>4</sup>, respectively. When atoms gather to molecules, some bands are generated from atomic orbitals. In both anatase and rutile phase, the valence band consists of mainly the 2p orbital of oxygen and the 3d orbital of titanium, while the conduction band comes from 3d orbitals of titanium. In the Figure 1-2, the parts colored by blue and red display the valence band and the conduction band. The top of the energy level in the valence band is fixed as 0 eV. The red dotted lines show the bandgap in the band structure of TiO<sub>2</sub>. The energy of the bandgap is 3.2 eV, which corresponds to the energy of UV light. Anatase phase TiO<sub>2</sub> is considered to bring higher photocatalytic activity because it has the larger energy of the bandgap, more reactive sites than the rutile phase TiO<sub>2</sub>. [7] For this reason, I focus on the anatase TiO<sub>2</sub> in this research.

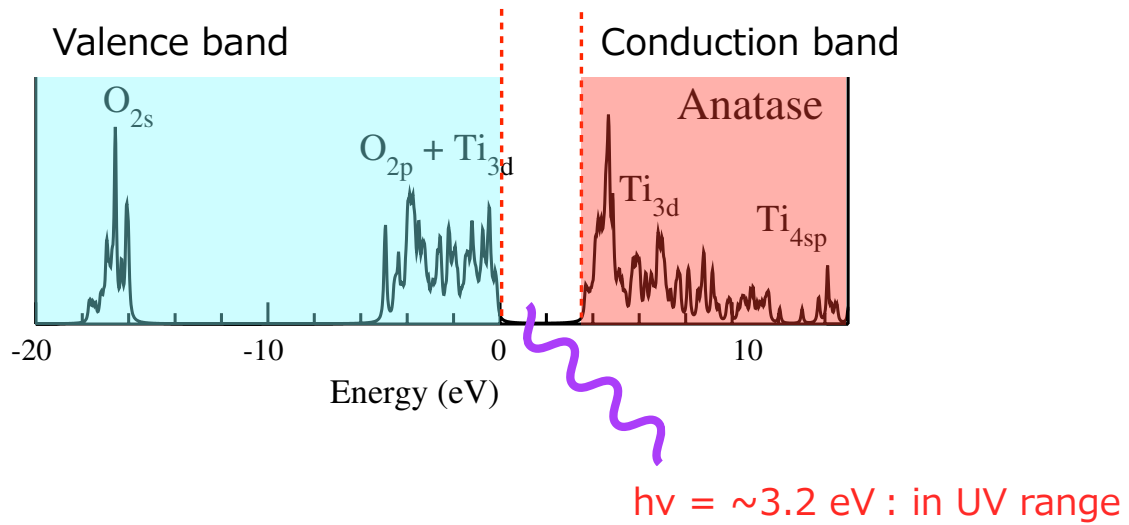


**Figure 1-2.** The electronic density of state of TiO<sub>2</sub> of the anatase phase. The highest occupied molecular orbital (HOMO) is derived from p orbital of oxygen, p and s orbital of titanium. The lowest unoccupied molecular orbital (LUMO) consists of mostly d orbital of titanium. [6] The difference of the energy between HOMO and LUMO is ~3.2 eV. 3.2 eV corresponds to the energy of UV light.

## 1.2 Photocatalysis on titanium dioxide

In the previous section, I introduced the crystal structures and the energy of bandgap in  $\text{TiO}_2$ . In this section, I explain the mechanism of photocatalysis and show important applications with  $\text{TiO}_2$ .

The mechanism of photocatalytic reaction on titanium dioxide is being studied by photovoltage spectroscopy, electron paramagnetic resonance (EPR), chemiluminescence method, infrared spectroscopy, and time-resolved spectroscopy. [8-14] According to these studies, the process of photocatalytic reaction has been clarified. When  $\text{TiO}_2$  is irradiated with UV light whose energy is more than energy of its bandgap, electrons in the valence band excited to the conduction band. The excited electrons and holes move to the surface of  $\text{TiO}_2$ . While or after the excited electrons and holes move to the surface, some of them are recombined to generate heat or emit light. The others are used in the reactions at the surface.

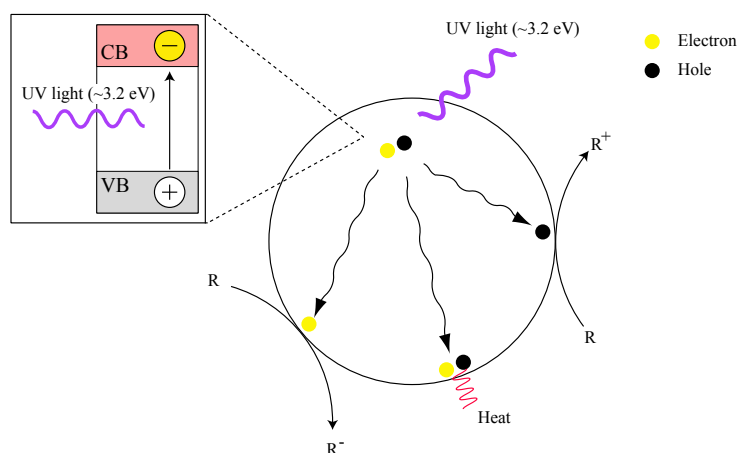
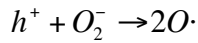
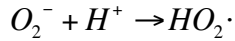


**Figure 1-3.** Process in  $\text{TiO}_2$  after UV irradiation. Electrons in the valence band are excited by UV light. Some of the excited electrons and holes move to the surface of  $\text{TiO}_2$ , and some are recombined to generate heat or emit light. The excited electrons and holes at the  $\text{TiO}_2$  surface are used for oxidation and reduction.

The reactions in photocatalysis occur through the interaction between electrons or holes and chemical species adsorbed on the  $\text{TiO}_2$  surface. Generally the reactions in photocatalysis are written by:



In these equations, R is the reactant at the surface of TiO<sub>2</sub>. HO<sub>2</sub>·, OH· and O· are radicals. In the oxidation reaction, the reactant accepts an electron to generate R<sup>-</sup>, and otherwise, HO<sub>2</sub>· is created after oxygen gets an electron. In the reduction reaction, the reactant discharges an electron to be reduced, and otherwise, OH· or O· are generated.

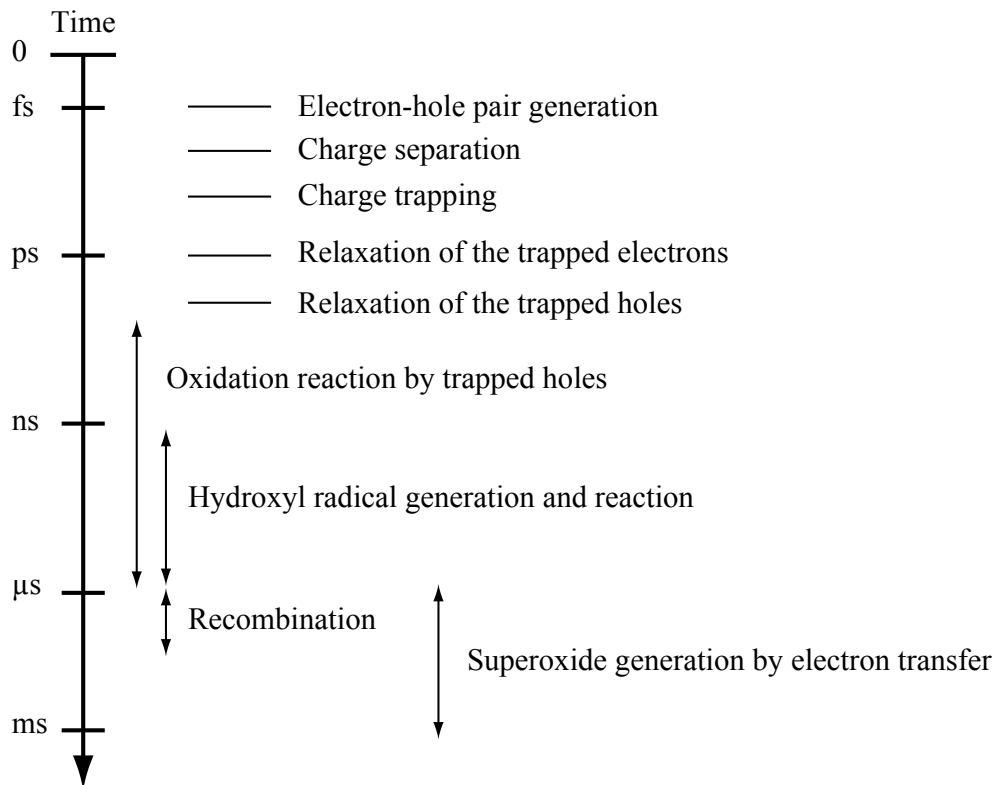


**Figure 1-4.** Time scales in photocatalysis. [22]

The time scale in photocatalysis is summarized in Figure 1-4. After TiO<sub>2</sub> is excited by UV light, excitation of electrons in TiO<sub>2</sub> occurs within 100 fs. [15] Excited electrons transfer to the surface of TiO<sub>2</sub> in picosecond-nanosecond region. [16] The time for chemical reactions at the surface depends on chemical species. For example, 2-propanol is oxidized in 100 ns. [17] At the same time as charge transfer, recombination of electron-hole pairs occurs within the range of

1-25  $\mu$ s to generate heat or emit light. [18] In short, the reactions in photocatalysis occur within msec.

By utilizing photocatalysis, many important applications were reported. [19-22]  $\text{TiO}_2$  photocatalysis have been used in mostly environmental purification and production of clean energy. [23-25]

Water purification by photocatalysis was done in 1977. [26] Photocatalytic treatment of water has several advantages, under the condition of ordinary temperature and pressure, with only irradiation of UV light, and moreover without toxic intermediate products. Owing to these advantages, huge number of applications to clean the water environment has been reported to date, e.g. removal of organic pollutants, remediation of metal contamination and water disinfection. [27-35] In the wastewater treatment,  $\text{TiO}_2$  photocatalyst works only under the low concentration of contaminants (0.1 ppm ~ 100 ppm) and strong UV light exposure. For the solar decontamination of industrial and agricultural wastewater, increasing the photocatalytic activity is required.

Air purification is also an important application because volatile organic compounds and air contaminated with bacteria and fungi may lead to the diseases. [36-40] Air cleaners with photocatalyst are already available on the market and being used in any locations such as hospitals, smoking rooms or food manufactures. So far, the photocatalytic activity is high enough to purify the air pollutants because the concentration of air pollutants that can be efficiently decomposed is low, which is the range from 0.01 ppm to 10 ppm. [41]

Photocatalysis is applied to produce hydrogen that is considered as a renewable energy source.  $\text{H}_2\text{O}$  is split to  $\text{H}_2$  and  $\text{O}_2$  by UV irradiation to  $\text{TiO}_2$ . [42] Because the decomposition reaction of  $\text{H}_2\text{O}$  is an uphill reaction as shown in the equation (1-2), energy of incident light is stored as the form of hydrogen molecules.



$\text{H}_2$  production by water splitting was achieved by supporting Pt on  $\text{TiO}_2$ . The band structure of  $\text{TiO}_2$  and Pt is shown in Figure 1-5. The electrons excited by UV irradiation move to the surface because the energy band is bent upward at the interface between  $\text{TiO}_2$  and water due to schottky barrier. When  $\text{TiO}_2$  contacts with Pt, hydrogen and oxygen are produced at the  $\text{TiO}_2$  and Pt

surface, respectively. The strong UV light sources like mercury lamps have been used for the test of hydrogen production to compensate for the low quantum yield. In order to utilize the sunlight for the energy production, improvement of production efficiency is necessary.

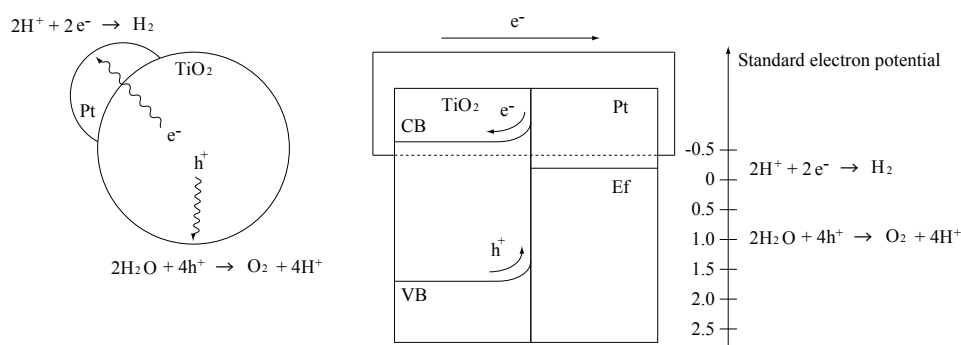


**Figure 1-5.** Schematic of the migration of electron-hole pairs (left), and band structures of TiO<sub>2</sub> and Pt. (right). At the surface of Pt, hydrogen generates and oxygen generates at the surface of TiO<sub>2</sub>. In the system for hydrogen production, excited electrons move to Pt due to gradient of potential. Oxidation and reduction powers are enough to generate hydrogen and oxygen simultaneously.

### 1.3 Enhancement of photocatalysis

As I emphasized in the 1.2, improving the photocatalytic activity of TiO<sub>2</sub> is needed because of mainly relatively low quantum efficiency and the limited flux of UV photons in the natural ambience. The attempts for the enhancement of photocatalytic activity that ever performed are categorized to mainly three, (1) increasing efficiency of excitation, (2) making higher mobility of electrons and holes, and (3) numbering up active sites. Researchers have tried in several ways since TiO<sub>2</sub> received attention. I show previous studies to explain the novelty of my way.

#### (1) Increasing excitation efficiency

Towards the use of TiO<sub>2</sub> under the sunlight, shift of the absorption edge to the visible region are attempted because more visible light is including in the sunlight than UV light. In order to make photocatalyst active to visible light, transition metal cations, metalloids and nitrogen ions are doped. The doped materials provide additional energy levels within the bandgap of TiO<sub>2</sub>. When TiO<sub>2</sub> absorbs visible light, excitation efficiency increases due to much light source in the sunlight. The remarkable visible-light photocatalyst is nitrogen-doped TiO<sub>2</sub> (TiO<sub>2-x</sub>N<sub>x</sub>) reported

by R. Arashi in 2001. [43] The active wavelength of visible-light photocatalyst was less than 500 nm. Figure 1-5 shows radiated spectrum of the sunlight. [44] At 480 nm, the irradiance of the sunlight takes the maximum value. Because much more visible photons are including in sunlight than UV photons, photocatalytic activity relatively got to be higher. Expanding absorption edge to 500 nm was consider to be improved the activity by ~4 times.

Utilization of plasmons for improving photocatalytic activity is a new way that started from 2008. [45] In plasmonics, the excitation of localized surface plasmons (LSP) on the surface of metallic nanostructures produces intense electric field amplitudes that can increase light absorption, thereby, improving the photocatalytic activities of TiO<sub>2</sub>. [46, 47] Typical materials utilized for plasmonics are noble metals (Au, Ag, and Cu) that exhibit high enhancements in the visible light region. [48] Although plasmonic photocatalysis has been demonstrated using Ag, the improvement effects were not sufficiently high because the plasmon resonance wavelength is out of the absorption band of TiO<sub>2</sub> (3.2 eV). As shown in Figure 1-5, in this research, I aimed to boost the UV light by plasmons in the UV range. Therefore, my research is also categorized here.

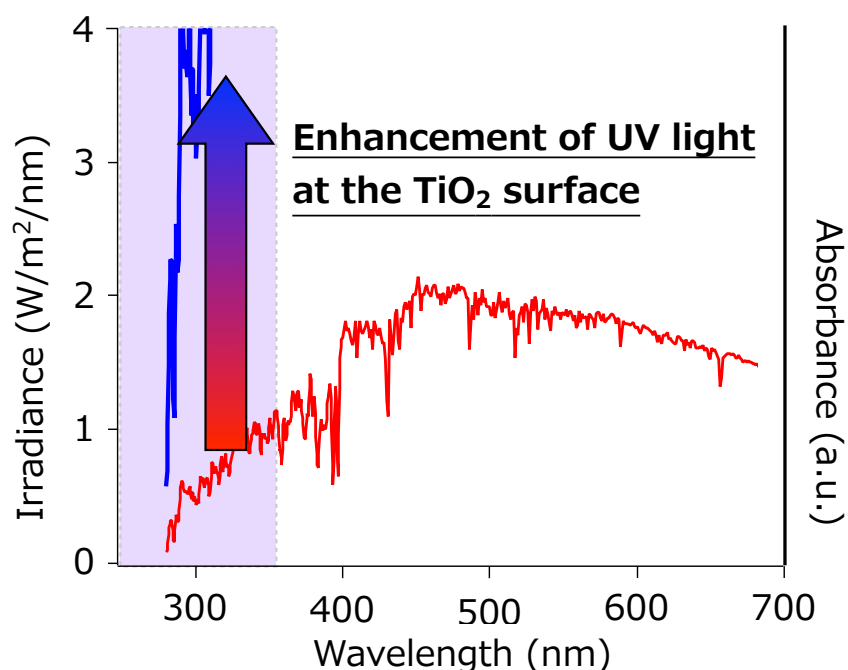


**Figure 1-6.** Radiated spectrum of the sunlight (red) and absorption spectrum of TiO<sub>2</sub> (black). This figure shows my aim.

## **(2) Making a higher mobility of electrons and holes**

Promotion of the charge separation to avoid recombination has been achieved by supporting metal such as Pt and Ni onto TiO<sub>2</sub>. [49, 50] As Metals are easy to capture the excited electrons, the flow of electrons induces separation of charge with suppressing the electron-hole recombination. While adding metals bring positive effect on photocatalytic activity, introduction of defects and cutoff of the incident light are induced. The balance between amount of TiO<sub>2</sub> and additive metals is important. At most, several percent of quantum efficiency of TiO<sub>2</sub> was improved to several tens by doping Pt.

The mobility of excited electrons and holes are improved by making higher crystalline of TiO<sub>2</sub>. Because defects trap the excited electrons or holes, and consequently induce recombination, high crystalline suppress the recombination, and as a result, leads higher mobility. [51] The crystallinity is tailored by conditions of synthesis process. Amorphous TiO<sub>2</sub> transformed to anatase and continuously rutile with increment of the anneal temperature.

## **(3) Numbering up active sites**

Although crystallization proceeds with reducing number of defects, the active sites for reaction get to decrease due to reduction of surface area. The balance of crystallinity and number of active sites is important. Figure 1-6 shows schematic of the relationship between crystallinity and number of active sites. To increase the active sites, the size of TiO<sub>2</sub> crystals is made smaller. Simultaneously, the bandgap energy becomes larger with smaller diameter of TiO<sub>2</sub>. (See Figure 1-8) Larger bandgap energy makes higher power of reduction and oxidization. [52] Furthermore, with decreasing sizes of TiO<sub>2</sub>, migration length of excited electrons and holes is getting to be small due to smaller distance between the surface and excited electrons. The size of ~ 6 nm is measured to be suit for photocatalysis. [53] In smaller TiO<sub>2</sub> than 6 nm, the number of defects at the surface goes up. Anatase phase TiO<sub>2</sub> with the diameter of ~ 6 nm is used in this research.

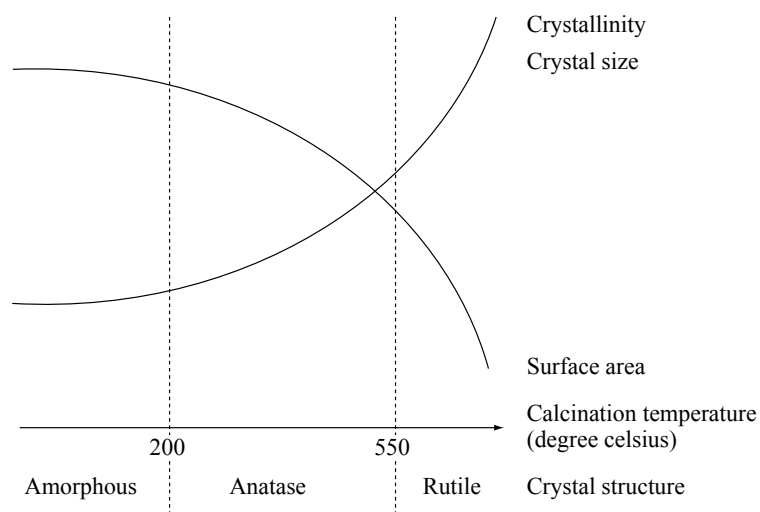


**Figure 1-7.** Relationship among crystallinity, surface area, and crystal phase with increasing temperature. When the amorphous of  $\text{TiO}_2$  is annealed, the phase of  $\text{TiO}_2$  changes to anatase and rutile with increasing the temperature. The rutile phase has high crystallinity. Therefore, The surface area and active sites are less than the other phases.

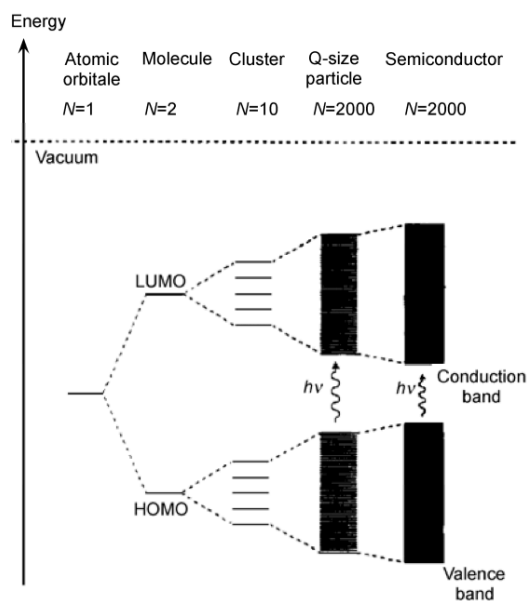


**Figure 1-8.** Narrowing bandgaps with decreasing the size of

## References

- [1] D. Reyes-Coronado, G. Rodríguez-Gattorno, M.E. Espinosa-Pesqueira, C. Cab, R. de Coss, G. Oskam, "Phase-pure TiO<sub>2</sub> nanoparticles: anatase, brookite and rutile", *Nanotechnology*, 19, 145605 (2008)
- [2] J. Moellmann, S. Ehrlich, R. Tonner, S. Grimme, "A DFT-D study of structural and energetic properties of TiO<sub>2</sub> modifications", *J. Phys.: Condens. Matter*, 24, 424206 (2012)
- [3] J. Zhang, M. Li, Z. Feng, J. Chen, C. Li, "UV Raman Spectroscopic Study on TiO<sub>2</sub>. I. Phase Transformation at the Surface and in the Bulk", *J. Phys. Chem. B*, 110, 2, 927–935 (2006)
- [4] X. Chen, S.S. Mao, "Titanium Dioxide Nanomaterials: Synthesis, Properties, Modifications, and Applications" *Chem. Rev.*, 107, 2891–2959 (2007)
- [5] H. Tang, H. Berger, P.E. Schmid, F. Levy, "OPTICAL PROPERTIES OF ANATASE (TiO<sub>2</sub>)", *Solid State Communications*, 92, 3, 267-271 (1994)
- [6] H. Wang, J.P. Lewis, " Second-generation photocatalytic materials: anion-doped TiO<sub>2</sub>", *J. Phys.: Condens. Matter*, 18, 421 (2006)
- [7] M. Xu, Y. Gao, E.M. Moreno, M. Kunst, M. Muhler, Y. Wang, H. Idriss, C. Wöll, "Photocatalytic Activity of Bulk TiO<sub>2</sub> Anatase and Rutile Single Crystals Using Infrared Absorption Spectroscopy", *Phys. Rev. Lett.* 106, 138302 (2011)
- [8] G. Schlichthörl, S.Y. Huang, J. Sprague, A.J. Frank, "Band Edge Movement and Recombination Kinetics in Dye-Sensitized Nanocrystalline TiO<sub>2</sub> Solar Cells: A Study by Intensity Modulated Photovoltage Spectroscopy", *J. Phys. Chem. B*, 101, 41, 8141–8155 (1997)
- [9] P.F. Schwarz, N.J. Turro, S.H. Bossmann, A.M. Braun, A.A. Abdel Wahab, H. Dürr, "A New Method To Determine the Generation of Hydroxyl Radicals in Illuminated TiO<sub>2</sub> Suspensions", *J. Phys. Chem. B*, 101, 36, 7127–7134 (1997)
- [10] D.M. Martino, H. van Willigen, M.T. Spitler, "FT-EPR Study of Photoinduced Electron Transfer at the Surface of TiO<sub>2</sub> Nanoparticles", *J. Phys. Chem. B*, 101, 44, 8914–8919 (1997)
- [11] K. Ishibashi, Y. Nosaka, K. Hashimoto, A. Fujishima, "Time-Dependent Behavior of Active Oxygen Species Formed on Photoirradiated TiO<sub>2</sub> Films in Air", *J. Phys. Chem. B*, 102, 12, 2117–2120 (1998)
- [12] B. Ohtani, K. Iwai, S. Nishimoto, S. Sato, "Role of Platinum Deposits on Titanium(IV) Oxide Particles: Structural and Kinetic Analyses of Photocatalytic Reaction in Aqueous Alcohol and Amino Acid Solutions", *J. Phys. Chem. B*, 101, 17, 3349–3359 (1997)
- [13] N.W. Duffy, K.D. Dobson, K.C. Gordon, B.H. Robinson, A.J. McQuillan, "In situ infrared

- spectroscopic analysis of the adsorption of ruthenium(II) bipyridyl dicarboxylic acid photosensitisers to TiO<sub>2</sub> in aqueous solutions", *Chemical Physics Letters*, 266, 451-455 (1997)
- [14] Y. Nakato, H. Akanuma, Y. Magari, S. Yae, J.-I. Shimizu, and H. Mori, "Photoluminescence from a Bulk Defect near the Surface of an n-TiO<sub>2</sub> (Rutile) Electrode in Relation to an Intermediate of Photooxidation Reaction of Water", *J. Phys. Chem. B*, 101, 25, 4934–4939 (1997)
- [15] D.P. Colombo Jr., K.A. Roussel, J. Saeh, D.E. Skinner, J.J. Cavaleri, R.M. Bowman, "Femtosecond study of the intensity dependence of electron-hole dynamics in TiO<sub>2</sub> nanoclusters", *Chem. Phys. Lett.*, 232, 207 (1995)
- [16] D.E. Skinner, D.P. Colombo Jr., J.J. Cavaleri, R.M. Bowman, "Femtosecond Investigation of Electron Trapping in Semiconductor Nanoclusters", *J. Phys. Chem.*, 99, 7853 (1995)
- [17] N. Serpone, D. Lawless, R. Khairutdinov, E. Pelizzetti, "Subnanosecond Relaxation Dynamics in TiO<sub>2</sub> Colloidal Sols (Particle Sizes  $R_p = 1.0-13.4$  nm). Relevance to Heterogeneous Photocatalysis", *J. Phys. Chem.*, 99, 45, 16655–16661 (1995)
- [18] G.P. Lepore, C.H. Langford, J. Víchová, A. Vlček Jr., "Photochemistry and picosecond absorption spectra of aqueous suspensions of a polycrystalline titanium dioxide optically transparent in the visible spectrum", *Journal of Photochemistry and Photobiology A: Chemistry*, 75, 1, 15, 67–75 (1993)
- [19] Y. Ohko, K. Hashimoto, A. Fujishima, "Kinetics of Photocatalytic Reactions under Extremely Low-Intensity UV Illumination on Titanium Dioxide Thin Films", *J. Phys. Chem. A*, 101, 8057-8062 (1997)
- [20] A.M. Peiró, C. Colombo, G. Doyle, J. Nelson, A. Mills, J.R. Durrant, "Photochemical reduction of oxygen adsorbed to nanocrystalline TiO<sub>2</sub> films: a transient absorption and oxygen scavenging study of different TiO<sub>2</sub> preparations", *J Phys Chem B.*, 110, 46, 23255-63 (2006)
- [21] T. Yoshihara, R. Katoh, A. Furube, Y. Tamaki, M. Murai, K. Hara, S. Murata, H. Arakawa, M. Tachiya, "Identification of Reactive Species in Photoexcited Nanocrystalline TiO<sub>2</sub> Films by Wide-Wavelength-Range (400–2500 nm) Transient Absorption Spectroscopy", *J. Phys. Chem. B*, 108, 12, 3817–3823 (2004)
- [22] A. Fujishima, X. Zhang, D.A. Tryk, "TiO<sub>2</sub> photocatalysis and related surface phenomena", *Surface Science Reports*, 63, 515–582 (2008)
- [23] A. Heller, "Chemistry and Applications of Photocatalytic Oxidation of Thin Organic Films", *Acc. Chem. Res.*, 28, 503–508 (1995)
- [24] T. Tatsuma, W. Kubo, A. Fujishima, "Patterning of Solid Surfaces by Photocatalytic

- Lithography Based on the Remote Oxidation Effect of TiO<sub>2</sub>", *Langmuir*, 18, 9632–9634 (2002)
- [25] Y. Ohko, T. Tatsuma, T. Fujii, K. Naoi, C. Niwa, Y. Kubota, A. Fujishima, "Multicolour photochromism of TiO<sub>2</sub> films loaded with silver nanoparticles", *Nature Mater.*, 2, 29–31 (2003)
- [26] G. Takei, T. Kitamori, H.-B. Kim, "Photocatalytic redox-combined synthesis of l-pipecolinic acid with a titania-modified microchannel chip", *Catal. Commun.*, 6, 357–360 (2005)
- [27] D.F. Ollis, E. Pelizzetti, N. Serpone, "Photocatalyzed destruction of water contaminants", *Environ. Sci. Technol.*, 25, 1522–1529 (1991)
- [28] A. Fujishima, X. Zhang, "Titanium dioxide photocatalysis: present situation and future approaches", *C. R. Chimie*, 9, 5–6, 750–760 (2006)
- [29] G.R. Deya, A.D. Belapurkar, K. Kishore, "Photo-catalytic reduction of carbon dioxide to methane using TiO<sub>2</sub> as suspension in water", *Journal of Photochemistry and Photobiology A: Chemistry*, 163, 3, 503–508 (2004)
- [30] J. Yu, L. Qi, M. Jaroniec, "Hydrogen Production by Photocatalytic Water Splitting over Pt/TiO<sub>2</sub> Nanosheets with Exposed (001) Facets"*J. Phys. Chem. C*, 114, 30, 13118–13125 (2010)
- [31] S.N. Frank, A.J. Bard, "Heterogeneous photocatalytic oxidation of cyanide ion in aqueous solutions at titanium dioxide powder", *J. Am. Chem. Soc.*, 99, 1, 303–304 (1977)
- [32] M.A. Fox, M.T. Dulay, "Heterogeneous photocatalysis", *Chem. Rev.*, 93, 1, 341–357 (1993)
- [33] A.A. Ismail, A.A. El-Midany, I.A. Ibrahim, H. Matsunaga, "Heavy metal removal using SiO<sub>2</sub>-TiO<sub>2</sub> binary oxide: experimental design approach", *Adsorption*, 14, 1, 21-29 (2008)
- [34] M.R. Prairie, L.R. Evans, S.L. Martinez, "Destruction of organics and removal of heavy metals in water via TiO<sub>2</sub>, photocatalysis in chemical oxidation: Technology for the nineties. In: Second International Symposium. Lancaster: Technomic Publishing Company (1994)
- [35] Y. Kikuchi, K. Sunada, T. Iyoda, K. Hashimoto, A. Fujishima, "Photocatalytic bactericidal effect of TiO<sub>2</sub> thin films: dynamic view of the active oxygen species responsible for the effect", *J. Photochem. Photobiol. A: Chem.*, 106, 51–56 (1997)
- [36] K. Sunada, T. Watanabe, K. Hashimoto, "Studies on photokilling of bacteria on TiO<sub>2</sub> thin film", *Journal of Photochemistry and Photobiology A: Chemistry*, 156, 227–233 (2003)
- [37] W.K. Jo, K.H. Park, "Heterogeneous photocatalysis of aromatic and chlorinated volatile organic compounds (VOCs) for non-occupational indoor air application", *Chemosphere*, 57, 555–565 (2004)

- [38] P. Pichat, J. Disdier, C. Hoang-Van, D. Mas, G. Goutailler, C. Gaysse, "Purification/deodorization of indoor air and gaseous effluents by TiO<sub>2</sub> photocatalysis", *Catal. Today*, 63, 363–369 (2000)
- [39] C.H. Ao, S.C. Lee, "Enhancement effect of TiO<sub>2</sub> immobilized on activated carbon filter for the photodegradation of pollutants at typical indoor air level", *Appl. Catal. B: Environ.*, 44, 191–205 (2003)
- [40] C.H. Ao, S.C. Lee, "Combination effect of activated carbon with TiO<sub>2</sub> for the photodegradation of binary pollutants at typical indoor air level", *J. Photochem. Photobiol. A: Chem.*, 161, 131–140 (2004)
- [41] S.A. Grinshpun, A. Adhikari, T. Honda, K.Y. Kim, M. Toivola, K.S. Ramchander-Rao, T. Reponen, "Control of Aerosol Contaminants in Indoor Air: Combining the Particle Concentration Reduction with Microbial Inactivation", *Environ. Sci. Technol.*, 41, 606–612 (2007)
- [42] M. Ashokkumar, "An overview on semiconductor particulate systems for photoproduction of hydrogen", *Int J Hydrogen Energy*, 23, 6, 427–38 (1998)
- [43] R. Asahi, T. Morikawa, T. Ohwaki, K. Aoki, Y. Taga, "Visible-Light Photocatalysis in Nitrogen-Doped Titanium Oxides", *Science*, 293, 5528, 269-271 (2001)
- [44] C. Gueymard, D. Myers, K. Emery, "Proposed reference irradiance spectra for solar energy systems testing", *Solar Energy*, 73, 6, 443-467 (2002)
- [45] K. Awazu, M. Fujimaki, C. Rockstuhl, J. Tominaga, H. Murakami, Y. Ohki, N. Yoshida, T. Watanabe, "A plasmonic photocatalyst consisting of silver nanoparticles embedded in titanium dioxide", *J. Am. Chem. Soc.* 130 1676 (2008)
- [46] P. Wang, B. Huang, Y. Dai, M.H. Whangbo, "Plasmonic photocatalysts: harvesting visible light with noble metal nanoparticles", *Phys. Chem. Chem. Phys.*, 14, 9813 (2012)
- [47] J. Xu, X. Xiao, F. Ren, W. Wu, Z. Dai, G. Cai, S. Zhang, J. Zhou, F. Mei, C. Jiang, "Enhanced photocatalysis by coupling of anatase TiO<sub>2</sub> film to triangular Ag nanoparticle island", *Nanoscale Research Letters* 7, 239 (2012)
- [48] S. Kawata, "Plasmonics: Future Outlook", *Jpn. J. Appl. Phys.* 52 (2013)
- [49] A.V. Rupa, D. Divakar, T. Sivakumar, "Titania and noble metals deposited titania catalysts in the photodegradation of tartrazine", *Catal Lett*, 132, 259–267 (2009)
- [50] W.K. Wong, M.A. Malati. "Doped TiO<sub>2</sub> for solar energy applications", *Sol Energy*, 36, 163–168 (1986)
- [51] A. Nakajima, S. Koizumi, T. Watanabe, K. Hashimoto, "Effect of repeated

photo-illumination on the wettability conversion of titanium dioxide", *Journal of Photochemistry and Photobiology A: Chemistry*, 146, 1–2, 129–132 (2001)

[52] G.S. Mital, T. Manoj, "A review of TiO<sub>2</sub> nanoparticles", *Chinese Sci Bull*, 56, 16 (2011)

[53] G. Cernuto, N. Masciocchi, A. Cervellino, G.M. Colonna, A. Guagliardi, "Size and Shape Dependence of the Photocatalytic Activity of TiO<sub>2</sub> Nanocrystals: A Total Scattering Debye Function Study.", *J. Am. Chem. Soc.*, 133, 3114 (2011)

## Chapter 2. Plasmonic nanoparticle

A surface plasmon is a wave of the electromagnetic charge density on the metals or its state. [1] The study of plasmons, including surface plasmons, is called plasmonics. The strong interest in the plasmonics is based on the amplification of incident and scattering light, confinement of light in the nanoscale region and high sensitivity to surrounding medium. Plasmonic properties open many applications such as surface-enhanced Raman and fluorescence spectroscopy, sensitizing sensors and microscopy beyond the diffraction limit. [2-5] When the metal nanoparticles smaller than the incident wavelength are irradiated by light, the incident amplification becomes much higher because the energy of incident light is localized in the nanoparticles. The surface plasmon in metal nanoparticles is referred to as localized surface plasmon (LSP). In this chapter, I introduce fundamentals of LSP firstly. Afterwards, LSPs of aluminum (Al) nanoparticles in the UV range will be theoretically explained because the target of the optical range is UV region (<400 nm) in this dissertation. Soon after, fabrication and observation of Al nanoparticles will be shown.

### 2.1 Localized surface plasmon

The optical response of materials is determined by their dielectric function,  $\varepsilon$ . It is written as

$$\varepsilon = \varepsilon_r + i\varepsilon_i \quad (2-1)$$

Here,  $\varepsilon_r$  and  $\varepsilon_i$  represent real and imaginary part of the dielectric function. The absolute values of the real part mean the strength of polarization. Positive and negative values of the real part mean the same and opposite phase shift of electrons' oscillation, respectively. The imaginary part of the dielectric function exhibits the loss or absorption during the optical interaction. In considering LSP, we deal with the dielectric functions of metals. The dielectric functions of metals are described by Drude-Sommerfeld model. [6] The resulting equation of the dielectric function is

$$\varepsilon(\omega) = \varepsilon_{\infty} - \frac{\omega_p^2}{\omega(\omega + i\gamma_0)} \approx \varepsilon_{\infty} - \frac{\omega_p^2}{\omega^2} + i \frac{\gamma_0 \omega_p^2}{\omega^3} \quad (2-2)$$

with  $\omega_p$  plasma frequency and  $\gamma_0$  the damping rate.  $\varepsilon_{\infty}$  includes the contribution of the bound electrons to the polarizability and should be 1 when only the free electrons contribute to the dielectric function. The plasma frequency is given by  $\omega_p = \sqrt{\frac{ne^2}{\varepsilon_0 m^*}}$  with  $n$  and  $m^*$  being the density and effective mass of the conduction electrons, respectively. The relaxation time ( $\tau$ ) of the oscillating electrons can be calculated from the conductivity  $\sigma$  by  $\tau = \sigma m^* / ne^2$ . Since most metals have a negative dielectric constant in a real part at optical frequency due to free electrons, LSPs in metallic nanoparticles are excited in the opposite phase to the external electric field ( $E_{ext}$ ). (See Figure 2-1) Generally, LSP is described by two manners, the quasistatic approximation method and Mie theory. [7, 8] The quasistatic approximation is useful for us to capture the feature of LSP. As shown in Figure 2-1, free electrons in a metallic nanoparticle get closer to one end of the nanoparticle when the nanoparticle is exposed in the external field. Then, a polarization is generated in the nanoparticle. Accordingly, this simple model gives us the polarizability  $P$  of the nanoparticle embedded in the medium as:

$$P = \varepsilon_1 \alpha E_0$$

$$\alpha = 4\pi r^3 \frac{\varepsilon_1 - \varepsilon_2}{\varepsilon_1 + 2\varepsilon_2} \quad (2-3)$$

In the equation 2-3,  $\varepsilon_1$  and  $\varepsilon_2$  represent dielectric functions of metal and surrounding medium.  $r$  is the diameter of the metallic particle. From this equation, the condition to excite LSP can be easily given as:

$$\text{Re}(\varepsilon_1 + 2\varepsilon_2) = 0 \quad (2-4)$$

Then, scattering and absorption cross sections are

$$C_{abs} = k \text{Im}(\alpha)$$

$$C_{sca} = \frac{k^4}{6\pi} |\alpha|^2 \quad (2-5).$$

In equation (2-2), it is found that the energy loss is described as the damping rate of electrons in metals. The energy loss due to plasmon damping is attributed to the interband transition, scattering caused by lattice defects and surface of metals, electron-electron interactions and

electron-phonon interactions. [9] For efficient excitation of plasmons, the imaginary parts of dielectric functions in metals need to be as small as possible.

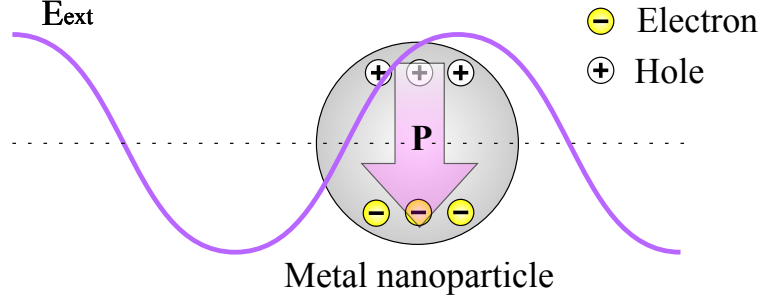


**Figure 2-1.** Schematic illustration of localized surface plasmon from the viewpoint of the quasistatic approximation. When the metal nanoparticle is exposed in the external field, electrons in the nanoparticle respond quickly and move to one side. Then, the polarization is generated inside the nanoparticle.

When the size of the nanoparticles is larger than several tens of nanometers, the phase of electrons' oscillations on the opposite side to incidence becomes delayed. The delay of the oscillation phase is called retardation. Mie theory gives us the precise solution while quasi-static approximation gives the solution without careful thought of the retardation. In Mie theory, scattering and absorption cross-sections are obtained by solving Maxwell equations with boundary conditions. [10] Extinction and scattering cross sections for a spherical particle are given as:

$$C_{ext} = \frac{2\pi}{k^2} \sum_{n=1}^{\infty} (2n+1) \text{Re} \left\{ |a_n|^2 + |b_n|^2 \right\} \quad (2-6)$$

$$C_{sca} = \frac{2\pi}{k^2} \sum_{n=1}^{\infty} (2n+1) (|a_n|^2 + |b_n|^2)$$

$$a_n = \frac{m\psi_n(mx) \psi_n'(x) - \psi_n(x) \psi_n'(mx)}{m\psi_n(mx) \xi_n'(x) - \xi_n(x) \psi_n'(mx)} \quad (2-7)$$

$$b_n = \frac{\psi_n(mx) \psi_n'(x) - m\psi_n(x) \psi_n'(mx)}{\psi_n(mx) \xi_n'(x) - m\xi_n(x) \psi_n'(mx)}$$

$\psi_n(\rho) = \rho j_n(\rho)$  and  $\xi_n(\rho) = \rho h_n^{(1)}(\rho)$  are Riccati-Bessel functions.  $x$  is called size parameter, and  $m$  is the relative refractive index. Those are written as:

$$x = ka = \frac{2\pi Na}{\lambda} \quad (2-8)$$

$$m = \frac{k_1}{k} = \frac{N_1}{N}$$

$N_1$  and  $N$  are the refractive indices of a metallic nanoparticle and surrounding medium, respectively.  $a$  is the radius of a metallic particle.

In Mie theory, structures are limited to the simple geometries of spheres and ellipsoids. In the case of arbitrarily shaped particles, discrete dipole approximation (DDA) is used for obtaining scattering, absorption and extinction spectra. E.M. Purcell developed DDA in 1973. [11] The program of DDSCAT for DDA calculations was released by Flatau and Drain. [12] The principle of DDA calculation is simple. The arbitrarily shaped particles are assumed to be divided into  $N$  domains. Here,  $N$  is the number of dipoles. Each domain has the polarizability. When the electric field is applied, the output of the electric field is described as the summation of electric field that is produced by each domain resulting from interactions between dipoles. Each dipole moment at each dipole is written by:

$$P_i = \alpha E_{loc}(r_i) \quad (2-10)$$

$$E_{loc}(r_i) = E_{ext}(r_i) - \sum_{j \neq i} A_{ij} P_j \quad (2-11)$$

$P_i$  is the dipole moment, and  $\alpha$  is the polarizability at the position  $i$ .  $E_{loc}$  is the local electric field at the position  $i$ .  $r_i$  is the positional vector.  $A_{ij}$  is a square matrix of size three, which exhibits the interaction between the dipoles at  $r_i$  and others. For ease of explanation, I just show  $C_{ext}$  and  $C_{abs}$  as follows. [13]

$$C_{ext} = \frac{4\pi k}{|E_0|^2} \sum_{j=1}^N \text{Im}(E_{ext}^*(r_j) \cdot P_j) \quad (2-12)$$

$$C_{abs} = \frac{4\pi k}{|E_0|^2} \sum_{j=1}^N \text{Im} \left\{ \left[ P_j \cdot (\alpha_j^{-1})^* P_j^* \right] - \frac{2}{3} k^3 |P_j|^2 \right\}$$

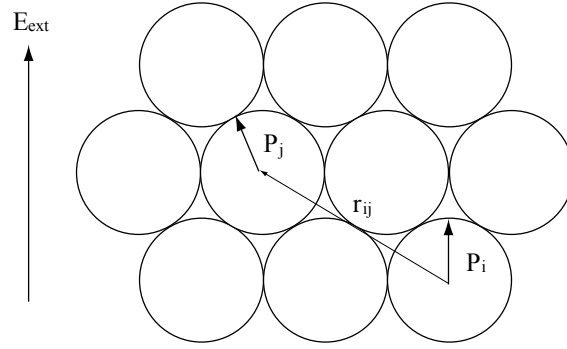


**Figure 2-2.** Alignment of dipoles for DDA simulation.  $E_{ext}$  is the external electric field.  $P_i$  and  $P_j$  are dipole moments at positions,  $i$  and  $j$ .  $r_{ij}$  is the displacement vector between dipoles,  $P_i$  and  $P_j$ .

For calculation by DDA, we need to determine three parameters, dielectric functions of elements, the range of wavelength, the distance between dipoles. The distance between dipoles determines the accuracy of calculation. It should be under the condition of

$$d < \frac{\lambda}{2\pi|n|} \quad (2-13)$$

, where  $d$  is the distance between adjacent dipoles,  $\lambda$  is a wavelength of incident light, and  $n$  is the refractive index of the particle. When dielectric functions of metals and values of spatial pitch are given, DDA calculation can be conducted.

The field intensity outside and inside nanoparticles is also calculated by the method proposed by Flatau and Draine. [13] The distribution of field intensity is obtained with utilization of the same program, DDSCAT.

## 2.2 Nanoscale heating by plasmonic nanoparticles

Metal nanoparticles exposed to incident laser irradiation at wavelengths close to the surface plasmon resonance efficiently couple the optical energy and generate heat in the process of plasmon's damping. The heat induced by the laser-irradiated metal nanoparticles is considered to be localized near the nanoparticles, and due to the small scale, becomes difficult to measure. The heating of nanoparticles in liquid environments where the nanoparticle temperature may rise significantly and then pass on the heat to molecules in the immediate vicinity is of particular interest since gold nanoparticles are entering wide use in biomedical fields. Emerging applications build on the biocompatible, or relatively nontoxic, nature of the particle, combined

with some unique optical physics that allows plasmonic photothermal therapy, photoacoustic tomography, photothermal imaging, and surface enhanced Raman spectroscopy [14–20]. For the successful application of gold nanoparticles, the investigation of the localized heating effects must be carried out in order to firstly understand the influence on the biological samples, and subsequently preclude unwanted thermal effects. The difficulty of such local temperature measurement lies in the fact that a thermal contrast mechanism as well as a spatial resolution of several nanometers is necessary to selectively observe the near-field heating of the nanoparticle. Several techniques for nanoscale thermometry have been reported, such as nanolithographic, nanomaterial-based, fluorescent materials, and nanoscale superstructure thermometry method [21–24]. In these methods, temperature probes such as a silicon tip, carbon nanotubes, terbium doped silica glass and CdTe nanoparticles were used. The thermal effect of the probe itself, either as a light absorber, or heat sink/source may be comparable to that of single nanoparticles. As a result, those techniques need careful evaluation before being applied to the measurement of single gold nanoparticles. Nevertheless, several works have been reported on nanoscale thermometry for gold nanoparticles. In 2006, gold nanoparticles embedded in an ice matrix were observed by Raman spectroscopy [25]. The sample was irradiated with laser and heat generation was inferred from the melting of the ice matrix. In 2008, the temperature elevation of gold nanoparticles was monitored using photoacoustic signals during photothermal therapy [26]. Both measurements were successful with relatively low spatial resolution. I aim to measure the temperature at the local area within several nanometers from the surface of gold nanoparticles, and measure in a range approximately ~40 degrees, which is critical to many biomaterials such as proteins [27].

I have investigated the local temperature of a laser irradiated single nanoparticle by white light scattering spectroscopy. White light scattering spectroscopy is a powerful method to measure the dielectric constant of the nanomaterial. [28] In the method I proposed here, the temperature can then be estimated through the surface plasmon peak shift due to the refractive index change of the surrounding medium. Although it is possible to observe a temperature-dependent spectral peak shift in uncoated nanoparticles at temperatures of 100 degrees or higher, the range of temperature measurement of interest in our experiment (approximately room temperature) does not allow the observation of a peak shift with uncoated particles. Gold nanoparticles were therefore coated by thermo-responsive polymer, poly(N-isopropylacrylamide) (pNIPAM) so that the surrounding medium was sensitive to nanoparticle

temperature. The heating effect was monitored by measuring the peak scattering wavelength derived from the surface plasmon of gold nanoparticles, which varied with the refractive index of the surrounding polymer. The scattering occurs predominantly from the gold-polymer interface, allowing a measurement of the gold nanoparticle temperature, and the gold nanoparticle temperature is assumed to be homogenous in the nanoparticle due to thermal conductivity. For nanoscale temperature measurement, pNIPAM-coated gold nanoparticles were fixed on a glass cover slip, immersed in water, and illuminated by continuous laser. The sensitivity of the measurement results from the scattering spectra sensitivity to the refractive index change at the boundary of the metal surface and coated polymer. The measurement spatial resolution is then predominantly limited by the size of the nanoparticle itself, which in these experiments was 40 nm. Temperatures were calibrated by then using a temperature controlled cell to heat a bulk sample of nanoparticles and measuring the temperature dependent peak shift by UV-VIS absorption spectroscopy. The heating effect of single gold nanoparticles under different laser powers and wavelengths are measured and discussed.

### **Calculated scattering property and heat generation of a gold nanoparticle**

Elastic scattering spectroscopy for local temperature measurement is based on the plasmonic property of metal nanoparticles, and the scattering efficiency of gold nanoparticles was calculated on the basis of Mie theory. [29] The calculation was done with a wavelength range of 200 nm to 1800 nm in 1.6 nm steps. The complex permittivity values for gold at different wavelengths were obtained from the work by Johnson and Christy. [30]

Calculations were performed for different nanoparticle sizes including diameters of 40, 50, 60, and 70 nm. To first evaluate the nanoparticle size dependent scattering spectra, the surrounding media was set to water, with a refractive index of  $1.33 + 0i$ . Figure 2-3(a) shows calculated absorption spectra for a gold nanoparticle with the diameter of 40 nm and with the surrounding refractive index of 1.33. In Fig. 2-3(a), blue dotted lines indicate illumination wavelengths, 488 and 532 nm. Figure 2-3(b) shows the calculated scattering spectra of different sized gold nanoparticles. The maximum value is then taken to be the scattering peak wavelength. As shown in Fig. 2-3(b), the peak wavelength changes from 533 nm to 546 nm as the particle size increases. In the case of a pNIPAM-coated gold nanoparticle, the real part of the surrounding refractive index varies from 1.33 to 1.42 [31], whereas the imaginary part is always 0. The scattering spectra calculated for a gold nanoparticle surrounded with different refractive indices

are shown in Fig. 2-3(c). A shift of around 8 nm was observed in Fig. 2-3(c). It has been reported that the refractive index of pNIPAM depends on the temperature, therefore, I expected that by monitoring the scattering peak shift, we can measure the local temperature of the particle.

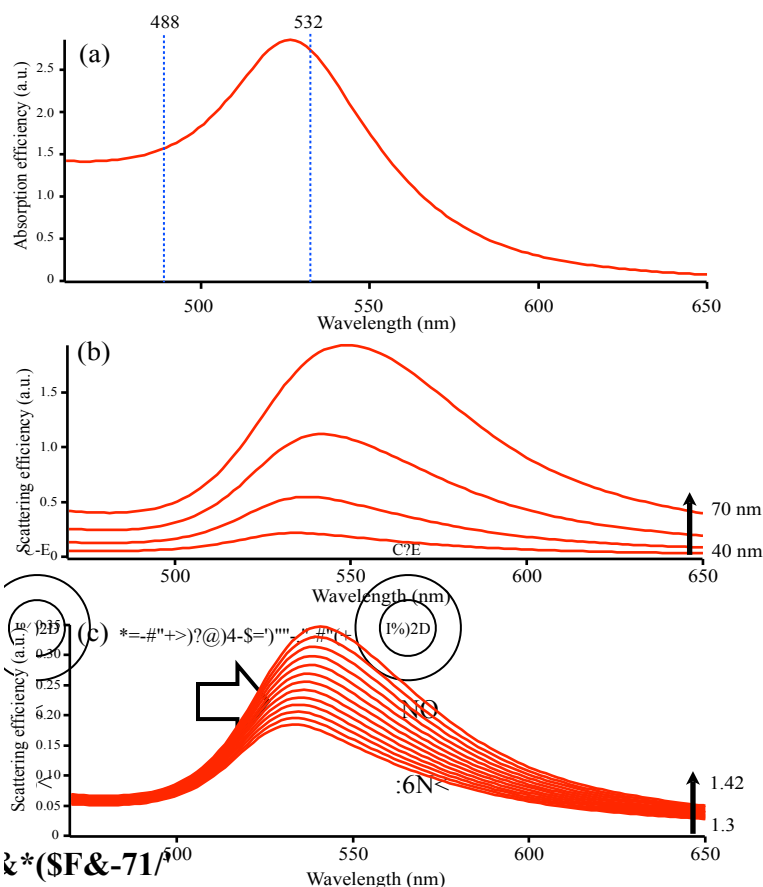


**Figure 2-3.** Calculated spectra showing (a) absorption spectra for a gold nanoparticle with diameter of 40 nm and surrounding refractive index of 1.33. Scattering spectra are shown in (b) for gold nanoparticles of different sizes. Figure (c) shows scattering spectra for “dielectric-a” coated gold nanoparticles (c) with different refractive indices. [55]

pNIPAM-coated gold nanoparticles were synthesized by the procedure as reported in Ref. 32. pNIPAM-coated gold nanoparticles were fixed on an aminosilane-modified glass cover slip by drop coating. Figure 2-4(a) and 2-4 (b) show scanning electron microscope (SEM) images of a pNIPAM-coated gold nanoparticle and an uncoated gold nanoparticle on a silicon substrate. The pNIPAM coating appeared with lower contrast around the solid gold core. Judging from the images, the typical size for the gold core was ~40 nm and the pNIPAM layer thickness was approximately 20 nm.

The optical setup for measuring nanoparticle scattering spectra and irradiating gold nanoparticles by laser is shown in Fig. 2-5. The white light source for scattering spectra was a xenon lamp and was spatially filtered through a 50  $\mu$  m pinhole. The light was collimated and introduced to an objective lens (100x, oil immersion) of 1.35 NA. Dark field illumination was realized by inserting a mask and an iris in the incident path (to block NA<1) and detection path (to block NA>1). The scattering signal was collected by the same objective lens, introduced to a spectrometer and detected by a Peltier cooled CCD camera. According to the Rayleigh scattering image on the entrance slit of the spectrometer, I selected the area of signal to extract only the scattering from a single pNIPAM-coated gold nanoparticle.

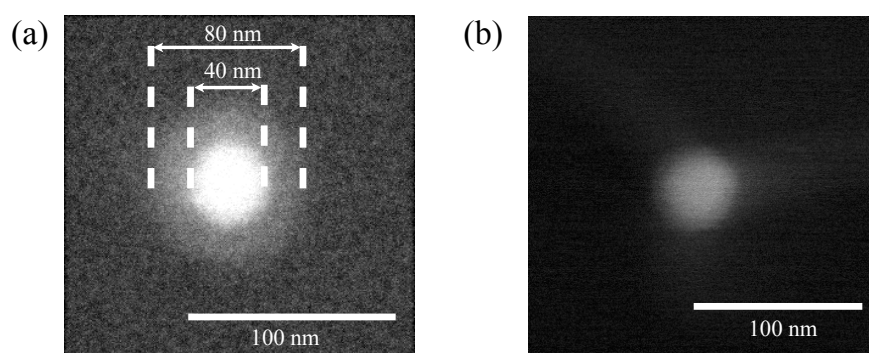


**Figure 2-4.** SEM Scanning electron microscope images of (a) pNIPAM-coated and (b) uncoated gold nanoparticles on a silicon substrate. The scale bar indicates 100 nm. [55]

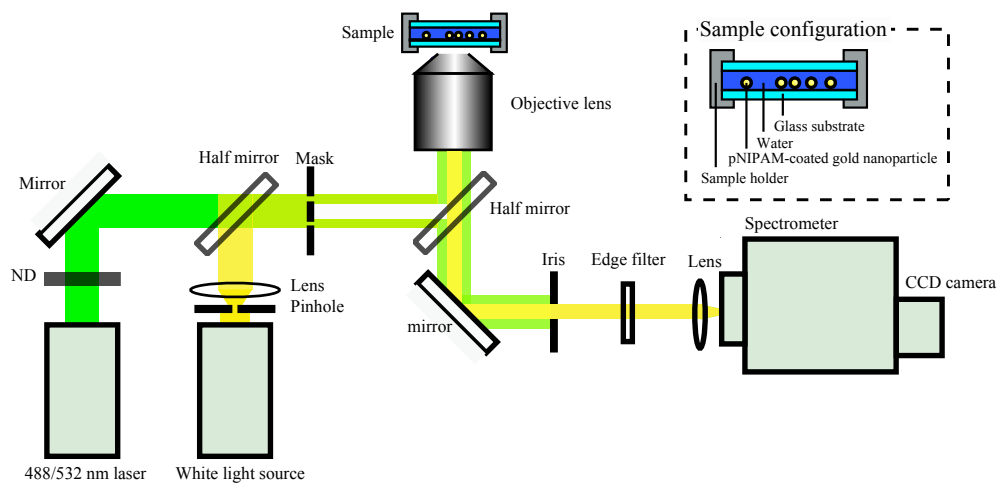


**Figure 2-5.** Optical setup for white light scattering spectroscopy and heating gold nanoparticles by laser. [55]

The laser for heating was provided by CW diode lasers of 488 nm and 532 nm wavelengths. The incident power was adjusted by an electrically controlled variable ND filter. The incident laser was expanded by 5 times and overlapped with the white light source. The Rayleigh scattering of laser irradiation was cut by an edge filter before entering the spectrometer. The white light scattering measurement of a laser-irradiated gold nanoparticles was performed with 60 sec acquisition times under continuous laser irradiation. Laser power was measured at the sample focus.

For precise calibration of scattering peak shift to temperature increase, it is optimal to obtain the calibration curve for each nanoparticle by observing how the scattering spectral peak shifts with temperature by measuring a single nanoparticle spectra while heating the entire sample holder on the microscope, however, it was not possible due to thermal drift of the stage. Instead, the bulk temperature of a water-based solution of pNIPAM-coated gold nanoparticles was measured by UV-VIS absorption spectrometer in a temperature-controlled cell to evaluate relationship between the temperature and the surface plasmon peak wavelength. The measurement was performed when the temperature-controlled cell had reached thermal equilibrium conditions.

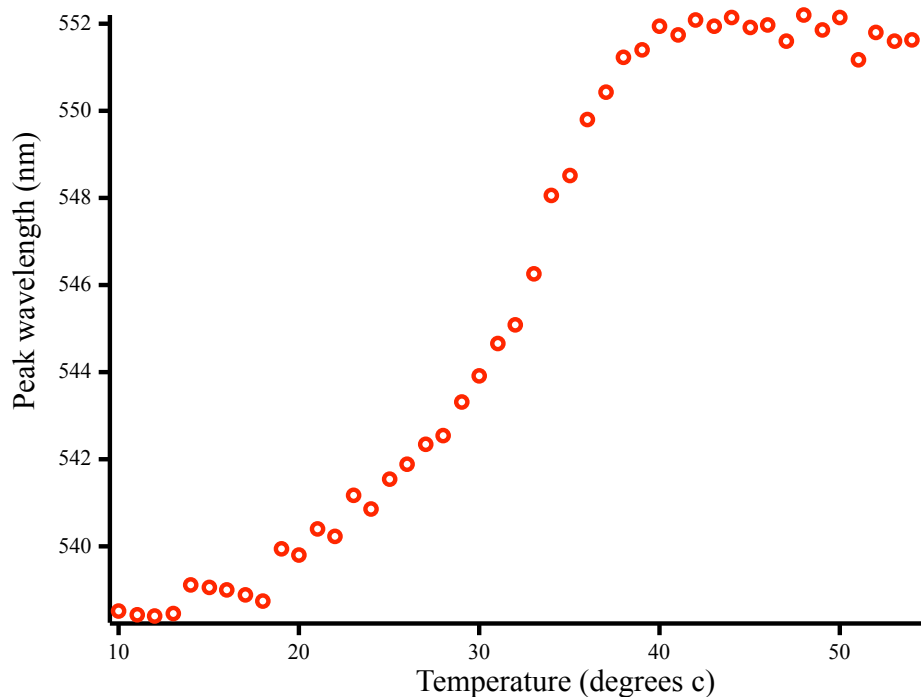


**Figure 2-6.** Response of a pNIPAM-coated gold nanoparticles nanoparticle solution to bulk temperature heating effects. Spectra are measured by UV-VIS absorption spectroscopy in a temperature controlled cell. The peak shift of surface plasmon absorption is evident. [55]

Figure 2-6 shows the scattering peak shift response of pNIPAM-coated gold nanoparticles to the bulk temperature. Peak wavelengths were obtained by Gaussian curve fitting of raw data. pNIPAM has a phase transition at ~35 degrees c and therefore the refractive index change is most sensitive to changes near this temperature [31]. Furthermore, it has been reported that the surface plasmon resonant peak wavelength is expected to undergo red shift with increasing temperature [32]. As Fig. 2-6 shows, the extinction peak predominantly shifts from 538 nm to 552 nm as the temperature rises from 10 to 40 degrees c. This result is consistent with previous works and showing that pNIPAM-coated gold nanoparticles which we prepared can be used for monitoring the localized heating effect, with particular emphasis on the temperature range which is relevant to biological cells. Cell lipid bilayer stability is known to change significantly in this temperature range with a rise of only several degrees. [33]

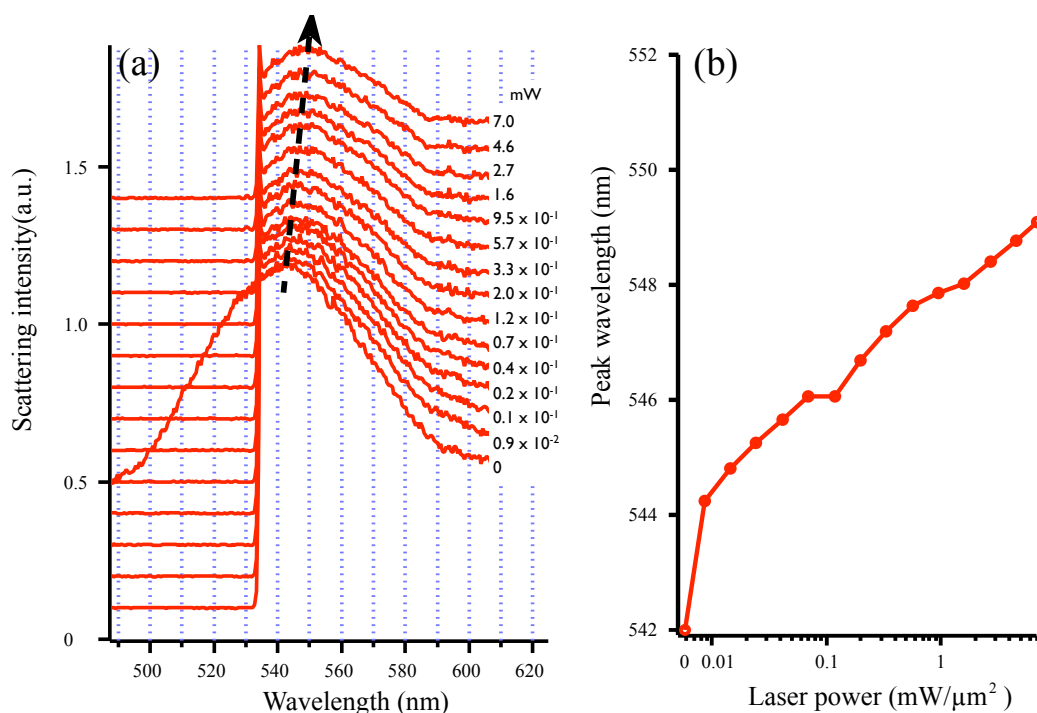


**Figure 2-7.** Scattering spectra of pNIPAM-coated gold nanoparticles irradiated with increasing laser at each power, and (b) the relationship between the scattering peak wavelength and laser power. Laser power was converted to that equivalent to the focal spot size. [55]

Following calibration, the local heating effect could then be measured for single gold nanoparticles under laser irradiation. pNIPAM-coated gold nanoparticles were fixed on a glass cover slip and immersed in water. A single pNIPAM-coated gold nanoparticle was irradiated with different laser powers, and scattering spectra were measured under each irradiating power. Figure 2-7(a) shows the spectra of a single pNIPAM-coated gold nanoparticle under 532 nm laser excitation, and Fig. 2-7(b) shows the relationship between the scattering peak wavelength and the laser power. In Fig. 2-8(a), the lowest spectrum shows an approximately Gaussian scattering curve. Since the peaks are close to the 532 nm excitation laser wavelength, spectra were generally taken with an edge filter which cut out a portion of the scattering spectra but left the peak intact, as shown in Fig. 2-7(a).

When the peak shifts are plotted against laser power in Fig. 2-7(b), the peak wavelength is observed to shift to progressively longer wavelengths as the laser power increased. Prior to laser irradiation, the scattering spectrum had a peak wavelength at 542 nm. This peak wavelength was longer than that in the calculated spectrum of 40 nm gold particles. Due to the measurement

of single nanoparticles, a range of different initial scattering peak wavelengths was observed. Some differences are likely to be due to minor variations in coating thickness and the glass substrate on which the particle rests [34]. When the laser irradiation started, the peak wavelength is seen shift to longer wavelengths, and by 1.2 mW, the peak reached 549 nm. Consequently, approximately 7 nm in total peak shift was observed. According to Fig. 4, a 7 nm peak shifts corresponds to a temperature increase of 10 degrees c. In this case, a single gold nanoparticle at room temperature (22 degrees c) was heated to 33 degrees c by a laser irradiation power of 1.2 mW. Such a small temperature increase at ~40 degrees c in the nanoscale region around the particle is very difficult to detect by conventional methods. I also note that the peak shift was caused by laser power rather than exposure time, since the nanoparticle can reach steady-state heating in a time scale of only nanoseconds [35]. The measurement time (60 seconds) was much longer than the thermal equilibrium time due to the requirement of collecting enough scattering signal to measure a single nanoparticle spectrum.

I observed several types of heating effect with 532 nm irradiation. In Fig. 2-9(a), 5 curves from different gold nanoparticles were shown. Each curve had different starting wavelengths since there are different distances between the gold nanoparticles and the glass substrate, differences in coated layer thickness, or in particle size. The data shown in Fig. 2-9(a) reveal that the heating effects appear to be different for each single particle. This makes it difficult to accurately predict the thermal heating of nanoparticles by laser, though most of the spectra show a shift to longer wavelengths with increasing laser power. It seems likely that the local heat generated and dissipated by a single nanoparticle is sensitive to its size, shape and local environment. This kind of variability is hidden by a collective measurement of bulk temperature in nanoparticle samples, and shows the limitations on the ability to measure a particular temperature rise for a particular nanoparticle in, for example, a live cell under laser irradiation. Even with the expected variability between particles which is highlighted by this measurement method, I still can predict tendencies of the laser heating effect. Figure 2-8(b) shows the scattering peak wavelength shift with increasing laser power under 488 nm laser irradiation. Compared to the 532 nm laser case, the 488 nm laser appears much less effective to heat a single gold nanoparticle. Most of the data exhibit almost no increase, though small fluctuations within ~2 nm are observable on close inspection. This suggests that ~3 mW was not strong enough to heat a single gold nanoparticle by 488 nm laser and plasmon absorption- based heating strongly depends on laser wavelength, as expected from Fig. 2-3(a). In the case of 532

nm irradiation, 4 out of 5 particles show a 10 degree C increment from the original temperature by a  $\sim 1$  mW illumination intensity.

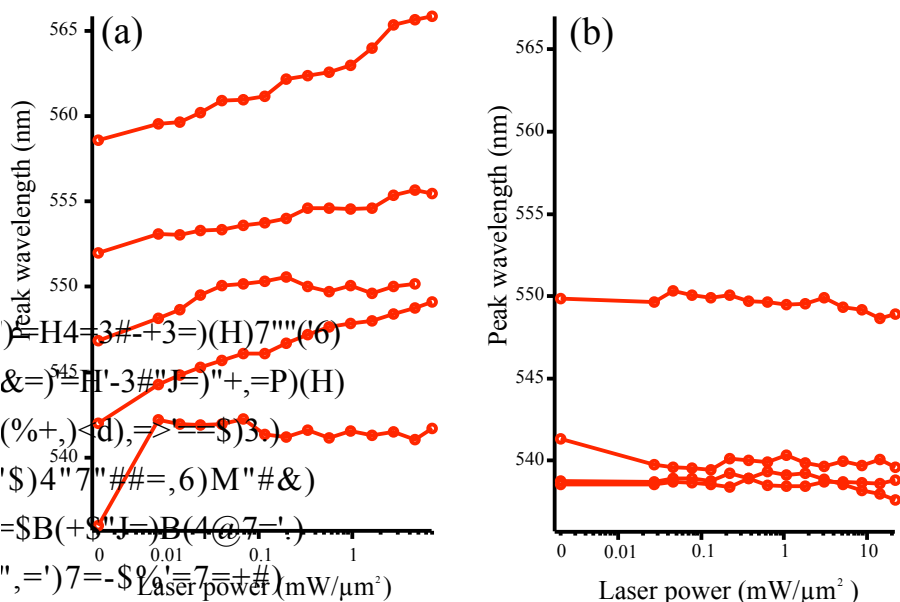


**Figure 2-8.** Relationship between peak wavelength and laser power with (a) 532 nm laser and (b) 488 nm laser. [55]

I discuss the effect of the surrounding environment and application of our data. Absorption of pNIPAM is much lower than that of gold nanoparticles in the visible range [36]. As a result, absorption of light by gold nanoparticles is dominant in our experiment. our results can be similarly applied. On the other hand, in experiments where the surrounding materials absorb light, especially near 540 nm, the relative absorption by gold nanoparticles will be reduced and the assumption of nanoparticle-dominated absorption will break down so that it becomes difficult to apply our results to these experiments. Furthermore, when the thermal conductivity and refractive index of the surrounding materials are similar to that of pNIPAM for example, proteins and other biological molecules, our results can directly be applied. If, however, the conductivity and refractive index are significantly different from pNIPAM, further calibration will be required before estimating the temperature effects.

Absorption of pNIPAM and water is small compared to plasmonic absorption of gold nanoparticles, hence, the temperature rise is mainly related to the absorption of gold. pNIPAM-coated gold nanoparticles are on a glass substrate and the distance between individual particles and the substrate is different due to variations in the polymer thickness. Heat diffusion from the gold nanoparticles therefore varies between individual single gold nanoparticles. As a

result, the equilibrium temperature is expected to vary and introduce some error in the measurements.

It is worth summarizing what these experiments predict for the use of nanoparticles as tags or contrast agents in live cells with laser irradiation. There are a wide range of nanoparticle types, sizes, and laser excitation conditions in current use. The laser wavelengths used with nanoparticles are often longer than 532 nm, and this method will allow experimental determination of upper power limits involving laser irradiation and nanoparticles. While I have used 532 nm for the experimental measurements in this paper, 532 nm is near the peak absorption of 50 nm nanoparticles, which is the most common size for surface-enhanced Raman measurements. For this reason, the 532 nm results are of value to experiments using other laser wavelengths in that they should indicate an upper limit on the thermal effect. Other wavelengths in the visible or near infrared range should result in lower heating of the particle. The measurement method used here is also most sensitive to temperature changes around 35 degrees Celsius. While this is limiting in terms of wide temperature range measurements, it is ideal for experiments using cultured cells with laser heating of nanoparticles since the cell temperature is usually maintained at 37 degrees.

As evident in Fig. 2-7(b) and Fig. 2-8, the application of even low power  $\sim 0.01$  mW resulted in a change in the scattering peak wavelength. By using the bulk temperature calibration data, I can estimate that the temperature can rise by several degrees around the nanoparticle. It is important to note that this measurement method results in very localized measurement of the temperature, on a scale of several tens of nanometers. Cells can survive brief exposure to localized plasma formation or complete ablation of sub-micron sized areas in the cytosol [37], and the nanoscale localized temperature increase is unlikely to manifest as an observable effect in the irradiated cell. Nevertheless it is necessary to understand if significant heating is occurring near the nanoparticle since this may affect protein folding, molecular binding, pH, or a number of other factors which may be of interest in the measurement.

## **Summary**

I have successfully observed the behavior of nanoscale localized heating of a laser irradiated single gold nanoparticle by white light scattering spectroscopy. The temperature increment of approximately 10 degrees C was observed by irradiating a gold nanoparticle by 532 nm laser at  $\sim 1$  mW. On the other hand, single gold nanoparticles irradiated by 488 nm did not display a

measurable temperature rise, which is consistent with the notion that the heating is dominated by absorption of the incoming light at the surface plasmon resonance wavelength. Even laser irradiation of 0.01 mW or less appeared to produce a temperature dependent shift in the scattering spectra peak wavelength. This has implications for the use of nanoparticles in cellular environments and shows that the heating effect of laser light on nanoparticles may not be negligible, and should be further studied, particularly at wavelengths longer than 532 nm. It was also found that the local heating effects for each nanoparticle were not uniform and fluctuations were observed in both on-resonant and off- resonant cases. This indicates that the localized heating itself may be unstable and susceptible to the immediate environment. The effects of nanoscale heat conduction and convection flows over the particle may be responsible for some of the observed instability. Such high sensitivity temperature measurement for a nanoparticle at room temperature range together with nanometer spatial resolution has not previously been achieved. The method will be useful to estimate the local temperature effects of laser irradiated nanoparticles in a variety of materials including particles in an inorganic matrix and endocytosed or injected nanoparticles in living cells.

### **2.3 Aluminum as a plasmonic material in UV range**

Metals such as Al, In, Ga, Sn, Tl, Pb and Bi, have been found to exhibit plasmonic properties in the UV range. [38] Among these metals, Al is the best choice in terms of practical use because of its low toxicity and high stability in air due to passive state of the surface. In this section, I will introduce theoretical description of the UV resonance of Al. Next I show the experimental results of LSP resonance wavelengths of Al in deep-UV range.

#### **Al resonant in the UV range**

The parameters of metals are summarized in table 1. [30, 39-43] Al has the larger value of plasma frequency than silver and gold. Judging from plasma frequency and damping rates of Al and noble metals, Al is considered to work efficiently as a plasmonic material as well as noble metals such as silver and gold. Next I focus on the resonant wavelength. Figure 2-10 shows dielectric functions of Al and silver. [44] Red and blue curves show Al and silver, respectively. Upper and lower figures are real and imaginary parts of dielectric functions. The range colored

by purple displays UV range. The black dotted line exhibits the condition of plasmon resonance. Silver is taken for instance because silver is one of the typical plasmonic materials that used in visible and near-UV range. The intersection of the dotted line and the real part in silver is seen at 370 nm. In UV range, silver does not exhibit plasmonic property because silver has absorption. On the other hand, Al has negative real part and small imaginary part in UV range. As a result, Al is possible to perform as a plasmonic material in near- to deep-UV.

**Table 2-1.** Drude parameters of aluminum, silver and gold. [39]  $\omega_p$  and  $\Gamma$  are plasma frequency and the total damping rate, respectively.  $\omega_{int}$  indicates the energy of onset for the interband transition.

	$\omega_p$ (eV)	$\Gamma$ (eV)	$\omega_{int}$ (eV)
Aluminum	12.7	0.13	1.41
Silver	9.2	0.02	3.9
Gold	8.9	0.07	2.3

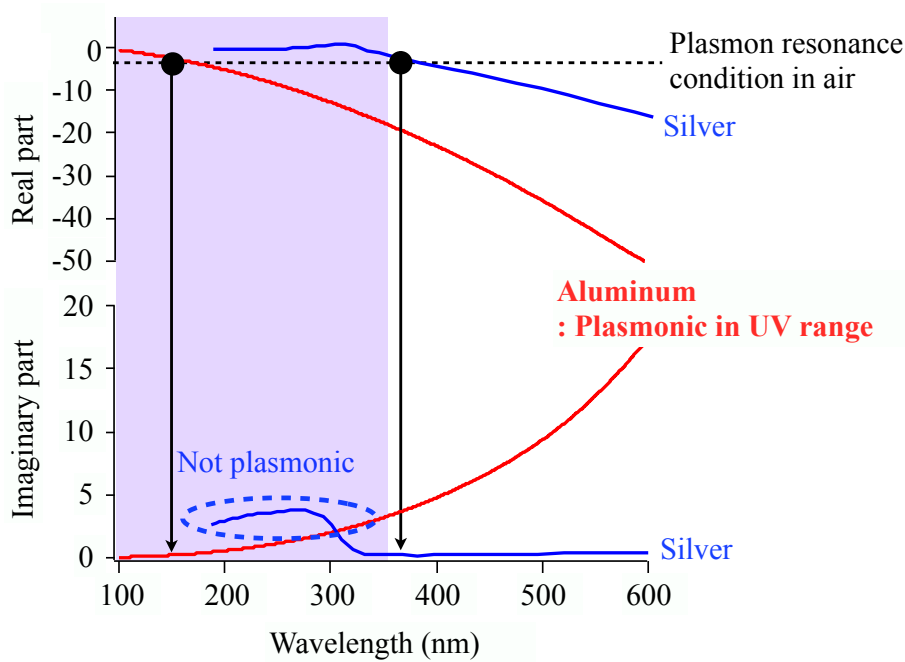


**Figure 2-9.** Dielectric functions of aluminum (red) and silver (blue). Upper and lower curves are real and imaginary parts of the dielectric functions, respectively.

In order to find the size for the most efficient excitation of plasmons in spherical Al nanoparticles, scattering spectra of Al nanoparticles were calculated by Mie theory. The dielectric function of Al in the ref. [44] was used for calculations. Fig 2-11 shows scattering spectra of Al nanoparticles with various diameters and relationship between diameter and scattering intensity at resonance. With increasing diameters, the scattering intensity at the resonant condition decreases with increasing the bandwidth. Increment of the bandwidth comes from loss due to absorption by mainly interband transitions. For smaller Al nanoparticles than 28 nm, scattering cross section was on the down slope by reduction of the particles' volume. When the diameter of Al nanoparticles is 28 nm, the scattering intensity becomes the largest. This indicates that the best size for plasmons in Al nanoparticles is 28 nm because the most efficient excitation of plasmons induces the strongest dipole with the largest radiation of light. By estimating from the mean free path of electrons in Al, 28 nm seems to be quite reasonable.

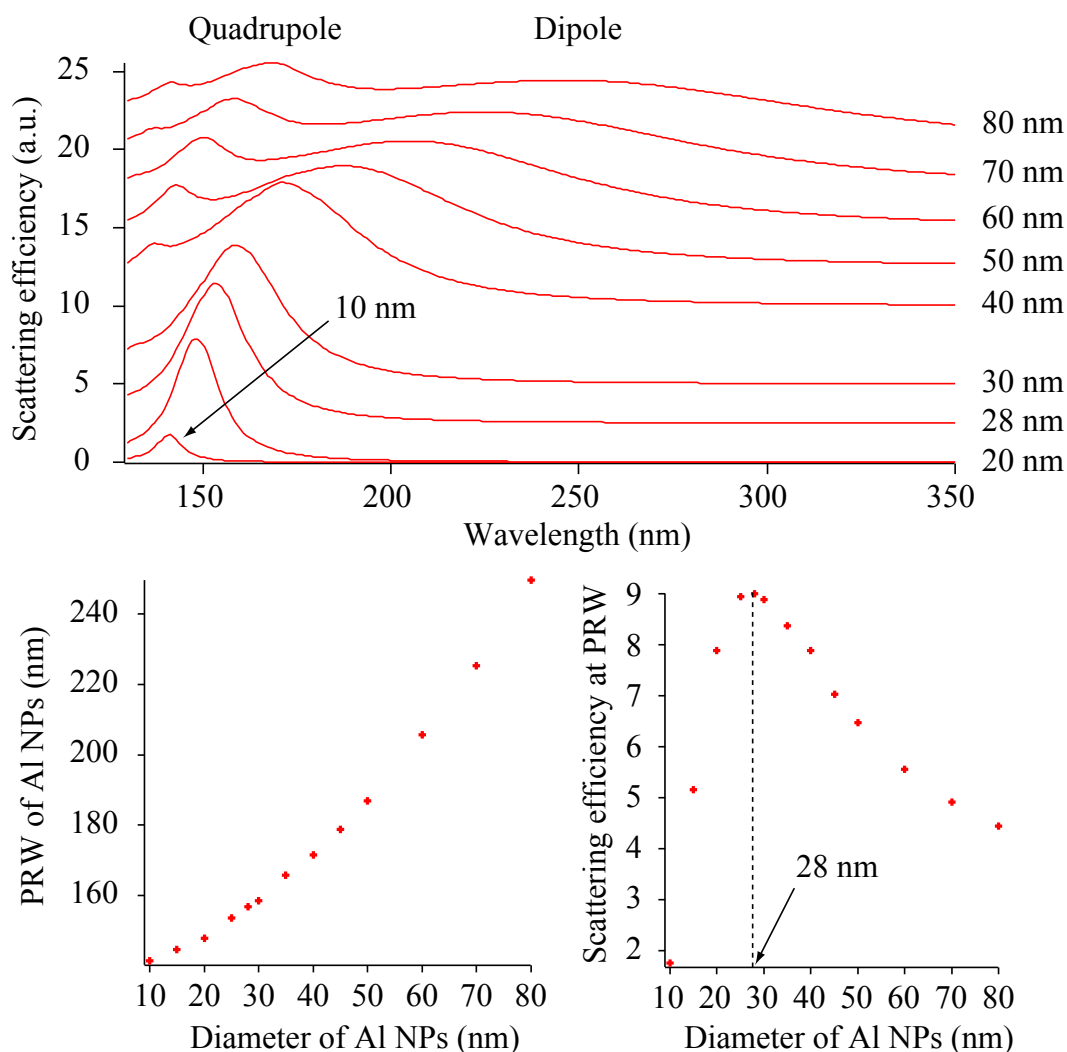


**Figure 2-10.** Scattering spectra of aluminum nanoparticles with the various sizes whose range were from 10 to 80 nm (top), relationship between the diameter and plasmon resonance wavelength (left bottom), and relationship between diameter and scattering efficiency at plasmon resonance wavelengths (right bottom).

Fabrication of Al nanoparticles has been attempted by mostly lithographic techniques because Al is quite reactive with water and organic matters. For the first time, in 2008, C. Langhammer et al. reported Al nanodisks that has resonant wavelength at 335 nm. [45] In the same year, G.H. Chan reported triangular Al nanoparticles that has the plasmon resonant wavelength at 390 nm. [46] In addition, Y. Ekinci et al. achieved 270 nm of plasmon resonant wavelength. [47] In 2012, A. Taguchi et al. also reported that plasmon resonance wavelength was obtained at 270 nm with developing nanosphere lithography. [48]

In the past, making plasmon resonance wavelength shorter has been directed toward

biological applications and UV photocatalysis. Plasmon resonance at 270 nm already opened applications of deep-UV surface enhanced Raman scattering spectroscopy and deep-UV tip-enhanced Raman scattering spectroscopy of adenine. [49, 50] However, much shorter plasmon resonance wavelengths are required for detecting biological molecules which have absorbance at deeper than 270 nm, e.g. tryptophan and Tyrosine. [51] Toward also the application of Al to TiO<sub>2</sub> photocatalysis, much shorter plasmon resonance wavelength is necessary because high refractive index of TiO<sub>2</sub> makes resonant wavelength longer, which does not correspond to the absorption edge of TiO<sub>2</sub>.

### **The shortest plasmon resonance wavelength: 244 nm**

We reported blue shifts in plasmon resonance wavelength by the control of Al nanoparticles' height in 2013. Finally, the shortest plasmon resonance wavelength of 244 nm was obtained for Al nanoparticles with the lateral size of 28 nm and the height of 14 nm. [52]

Nanosphere lithography (NSL) was employed for fabricating Al nanoparticles. I will explain the method of NSL in the chapter 3. At this time, I focus on the fabricated Al nanoparticles. Fig 2-11 displays the AFM images of Al nanoparticles on a quartz substrate. Those show honeycomb structures in nanometer scale. The average lateral sizes of the particles were 80, 40, and 28 nm shown in Fig. 2-11(a), (b), and (c), respectively. Fig 2-12 shows UV-VIS extinction spectra of Al nanoparticles for characterization of plasmon resonance wavelength (PRW). The lateral sizes of particles shown in Fig. 2-11(a), (b), and (c) correspond to 80, 40, 28 nm. In Fig 2-12 (a), particles' heights were 41, 27, and 22 nm. As the height of particles increase, blue shift of PRW was observed. In Fig 2-12 (b), PRWs are 299, 288 and 270 nm with particles heights of 10, 23, and 28 nm. As is the case with Fig 2-12 (a), blue shift was observed with increment of the particles' height. In Fig 2-12 (c), the particles' height changed from 10 to 14 nm with fixing the lateral size of 28 nm. Because of the technical issue in fabrication, the limitation was caused in the height. In Fig 2-12 (c), particles show tendency of blue shift with increasing the height.

DDA simulations for Al nanoparticles are conducted. The size of the distance between dipoles was fixed to 1 nm. Incident light with the polarization in-plane direction was assumed to irradiate the structure from the side of the Al structure. Output signals including transmitted and scattered light are detected at the side of a quartz substrate. The size and shape of Al structures were determined with using experimental values as shown in Fig. 2-13. There are the layers of

oxidized Al ( $\text{Al}_2\text{O}_3$ ) between Al and air. The thickness of the oxidized layer was assumed to be 2 nm. [54] Comparing to the PRW of bare Al nanoparticles, PRWs of Al nanoparticles covered with the  $\text{Al}_2\text{O}_3$  layer shift up due to higher refractive index of  $\text{Al}_2\text{O}_3$  than that of air. Al nanoparticles with the  $\text{Al}_2\text{O}_3$  layer is put on the quartz substrate with the thickness of 50 nm.

Figure 2-14 is relationship between LSPR wavelength and the structure's heights. The solid and dotted lines indicate experimental and simulation results. The blue shift with increasing particles' heights is observed in simulation results. LSP wavelengths in experimental results agree with simulation results except for the result with Al nanoparticles of 80-nm-diameter and 22-nm-height. When the diameters of Al nanoparticles are larger than 40 nm, the shape of the particles is closed to pyramidal. Furthermore, for thin Al nanoparticles, particles have sharp corners at edges. I calculated LSPR wavelength with assuming that the more thick oxidation layer was created at sharp corners. Then, 432 nm of LSPR wavelength was obtained as indicated as a star in Fig. 2-14. The simulation result of pyramidal nanoparticles is more consistent with experimental results than that of hemispherical particles. In conclusion, in the UV range, LSPR wavelengths of Al nanoparticles are confirmed to shift to shorter wavelengths with increasing heights. DDA simulation supported experimental results. 244 nm of the LSPR wavelength was observed. The tunable range of LSPR wavelength was from 244 to 450 nm. The blue shift by decreasing the lateral size of nanoparticles is attributed to LSP of Al nanoparticles. Blue shift was also observed by increasing the height with fixing the lateral size. This is similar to the behavior of LSP in silver reported in the past. [53] From also Mie theory, blue shift was expected with the structures getting close to a sphere from an oblate ellipsoid. [9] I explain the mechanism of the blue shift by increasing the particles' height. The number of electrons in Al nanoparticle increases by increasing particles' height. The range of oscillation is kept because the lateral sizes are fixed while the number of electrons increases. Then, the interaction between electrons and holes in higher Al nanoparticles becomes stronger than in lower ones. Because the larger dipole moment is induced in higher Al nanoparticles, the resonance wavelength shifts to the shorter wavelength.

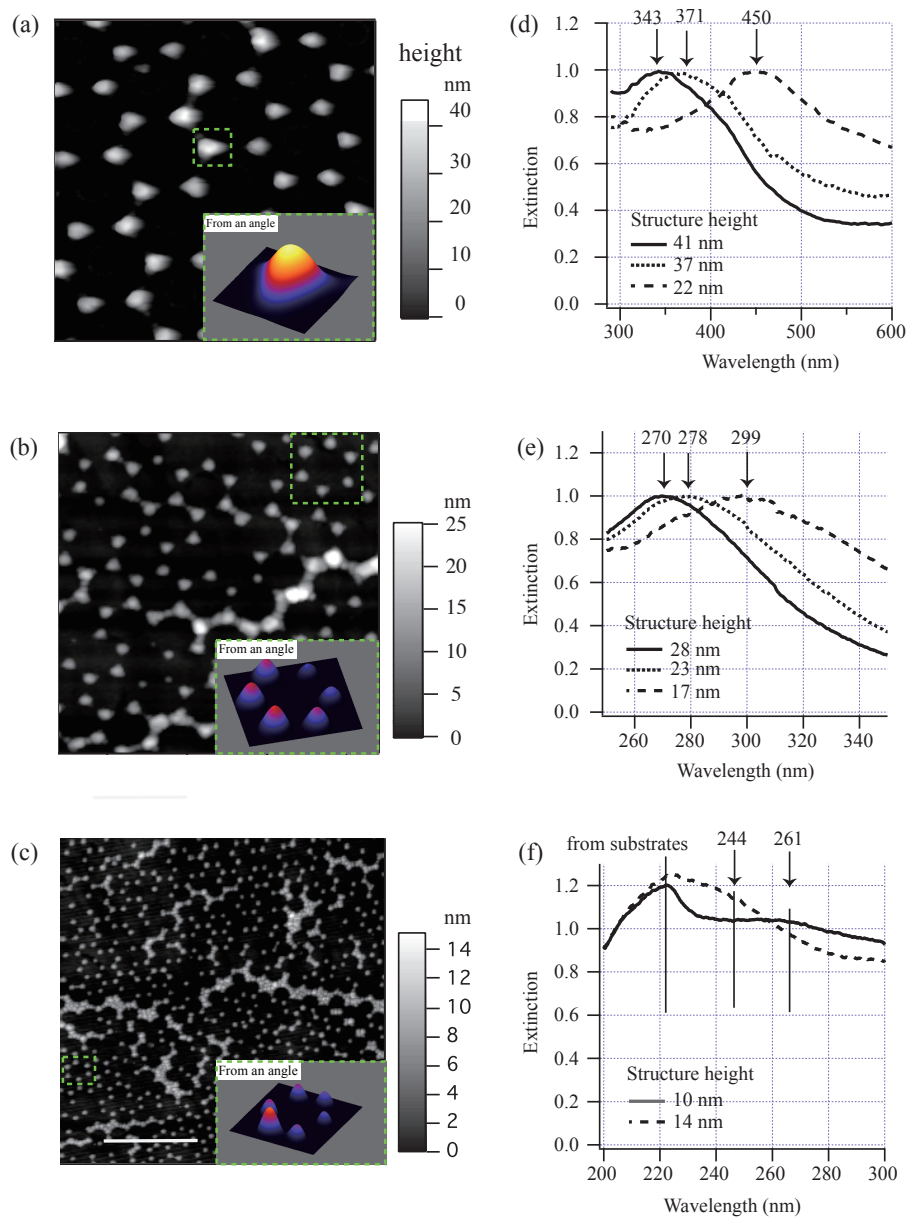


**Figure 2-11.** AFM images (left) and extinction spectra (right) of aluminum nanoparticles fabricated by Nanosphere lithography. Template bead diameters were (a) 300 nm, (b) 200 nm, and (c) 100 nm. The average lateral sizes of the nanostructure were 80 nm for (a), 40 nm for (b), and 28 nm for (c). (a) 80 nm average lateral size with heights of 41, 27, and 22 nm, (b) 40 nm average lateral size with heights of 17, 23, and 28 nm, and (c) 28 nm average lateral size with heights of 10 and 14 nm. The peak positions were determined by a curve fitting procedure. Blue shifts were observed by increasing the height. [52]

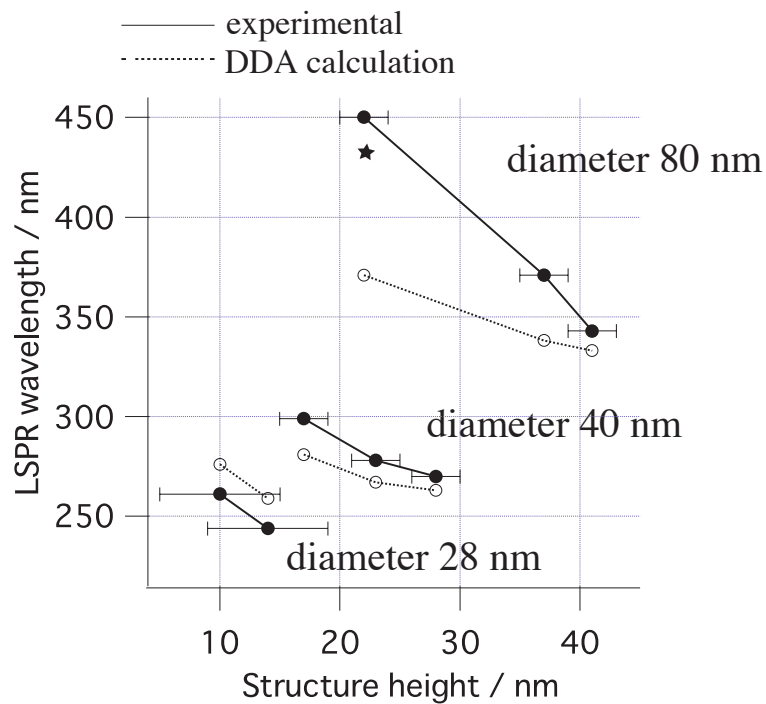


**Figure 2-12.** The relationship between the height of the aluminum nanostructure and the LSPR peak wavelength. The solid lines indicate the experimental results, and the dotted lines indicate the results of DDA calculations. Error bars indicate standard deviations of the measured height. Blue shifts with increasing height were observed both in the experimental and calculation results. The simulation model is illustrated in Fig. 2-13 (a). The star represents the result obtained using a different model shown in Fig. 2-13(b). [52]

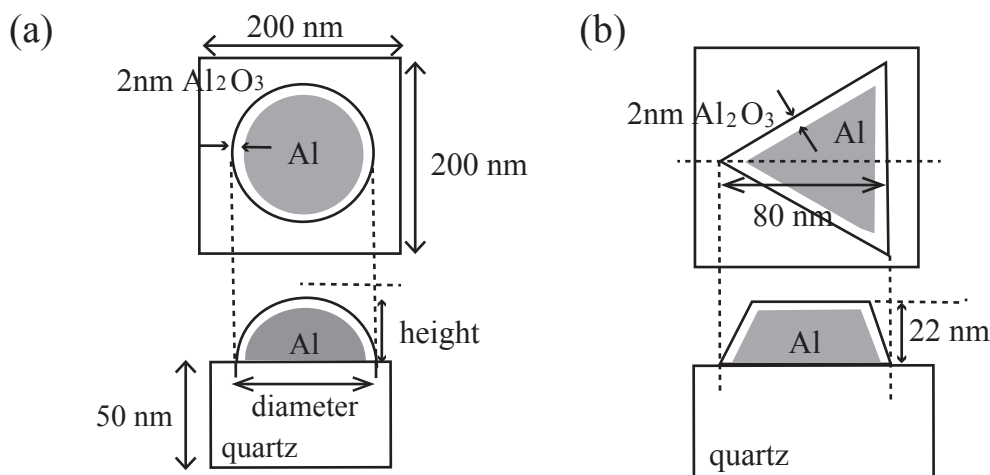


**Figure 2-13.** Simulation models. The height and diameter parameters were set with reference to the experimental results. (a) Hemisphere model, and (b) triangle model. [52]

## References

- [1] E. A. Stern, R.A. Ferrell, "Surface Plasma Oscillations of a Degenerate Electron Gas", *Phys. Rev.* 120, 130–136 (1960)
- [2] K.A. Willets, R.P. Van Duyne, "Localized Surface Plasmon Resonance Spectroscopy and Sensing", *Annual Review of Physical Chemistry*, 58, 267-297 (2007)
- [3] J.N. Anker, W. P. Hall, O. Lyandres, N.C. Shah, J. Zhao, R.P. Van Duyne, "Biosensing with plasmonic nanosensors", *Nat. Mater.* 7, 442 (2008).
- [4] S. Kawata, "Plasmonics for Nanoimaging and Nanospectroscopy", *Appl. Spectrosc.*, 67, 117 (2013)
- [5] Y. Okuno, Y. Saito, S. Kawata, and P. Verma, "Tip-enhanced Raman investigation of extremely localized semiconductor-to-metal transition of a carbon nanotube", *Phys. Rev. Lett.*, 111, 216101 (2013)
- [6] A.F. Palonpon, J. Ando, H. Yamakoshi, K. Dodo, M. Sodeoka, S. Kawata, K. Fujita, "Raman and SERS microscopy for molecular imaging of live cells," *Nat. Protoc.*, 8, 677-692

(2013)

- [7] K.L. Kelly, E. Coronado, L.L. Zhao, G.C. Schatz, "The Optical Properties of Metal Nanoparticles: The Influence of Size, Shape, and Dielectric Environment", *J. Phys. Chem. B*, 107, 3, 668–677 (2003)
- [8] C.F. Bohren, D.R. Huffman, "Absorption and Scattering of Light by Small Particles", New York: Wiley (1983)
- [9] S.A. Maier, "Plasmonics: fundamentals and Applications", Berlin: Springer (2007)
- [10] E.M. Purcell, C.R. Pennypacker, "Scattering and Absorption of Light by Nonspherical Dielectric Grains", *Astrophysical Journal*, 186, 705-714 (1973)
- [11] B.T. Draine, P.J. Flatau, "Discrete dipole approximation for scattering calculations", *J. Opt. Soc. Am. A*, 11, 1491-1499 (1994)
- [12] B.T. Draine, P.J. Flatau, "User Guide to the Discrete Dipole Approximation Code DDSCAT 7.2" (2012)
- [13] B.T. Draine, P.J. Flatau, "Fast near-field calculations in the discrete dipole approximation for regular rectilinear grids", *Optics Express*, 20, 1247-1252 (2012)
- [14] X. Huang, P.K. Jain, I.H. El-Sayed, M.A. El-Sayed, "Plasmonic photothermal therapy (PPTT) using gold nanoparticles," *Lasers Med. Sci.* 23, 3, 217–228 (2008).
- [15] A. Barhoumi, R. Huschka, R. Bardhan, M.W. Knight, N.J. Halas, "Light-induced release of DNA from Plasmon-resonant nanoparticles: Towards light-controlled gene therapy," *Chem. Phys. Lett.* 482, 4-6, 171–179 (2009)
- [16] R.R. Anderson, J.A. Parrish, "Selective photothermolysis: precise microsurgery by selective absorption of pulsed radiation," *Science* 220(4596), 524–527 (1983)
- [17] X.D. Wang, Y. Pang, G. Ku, X. Xie, G. Stoica, L.V. Wang, "Noninvasive laser-induced photoacoustic tomography for structural and functional in vivo imaging of the brain," *Nat. Biotechnol.*, 21, 7, 803–806 (2003)
- [18] D. Boyer, P. Tamarat, A. Maali, B. Lounis, M. Orrit, "Photothermal imaging of nanometer-sized metal particles among scatterers", *Science*, 297, 5584, 1160–1163 (2002)
- [19] K. Fujita, S. Ishitobi, K. Hamada, N. I. Smith, A. Taguchi, Y. Inouye, S. Kawata, "Time-resolved observation of surface-enhanced Raman scattering from gold nanoparticles during transport through a living cell", *J. Biomed. Opt.*, 14, 2, 024038 (2009)
- [20] X. X. Han, B. Zhao, Y. Ozaki, "Surface-enhanced Raman scattering for protein detection," *Anal. Bioanal. Chem.*, 394, 7, 1719–1727 (2009)
- [21] W. Haeberle, M. Pantea, and J.K.H. Hoerber, "Nanometer-scale heat-conductivity

- measurements on biological samples,” *Ultramicroscopy*, 106, 8-9, 678–686 (2006)
- [22] C.M. Tan, J. Jia, W. Yu, “Temperature dependence of the field emission of multiwalled carbon nanotubes,” *Appl. Phys. Lett.*, 86, 26, 263104 (2005)
- [22] H. Aizawa, T. Katsumata, S. Komuro, T. Morikawa, H. Ishizawa, E. Toba, “Fluorescence thermometer based on the photoluminescence intensity ratio in Tb doped phosphor materials”, *Sens. Actuators A Phys.*, 101, 1, 78–82 (2002)
- [23] J. Lee, A.O. Govorov, N.A. Kotov, “Nanoparticle assemblies with molecular springs: a nanoscale thermometer,” *Angew. Chem.*, 117, 45, 7605–7608 (2005)
- [24] C. Gota, K. Okabe, T. Funatsu, Y. Harada, S. Uchiyama, “Hydrophilic fluorescent nanogel thermometer for intracellular thermometry”, *J. Am. Chem. Soc.*, 131, 8, 2766–2767 (2009)
- [25] H.H. Richardson, Z.N. Hickman, A.O. Govorov, A.C. Thomas, W. Zhang, M.E. Kordesch, “Thermo-optical properties of gold nanoparticles embedded in ice: characterization of heat generation and melting,” *Nano Lett.*, 6, 4, 783–788 (2006)
- [26] J. Shah, S. Park, S. Aglyamov, T. Larson, L. Ma, K. Sokolov, K. Johnston, T. Milner, S.Y. Emelianov, “Photoacoustic imaging and temperature measurement for photothermal cancer therapy”, *J. Biomed. Opt.*, 13, 3, 034024 (2008)
- [27] X. He, W. F. Wolkers, J. H. Crowe, D. J. Swanlund, J. C. Bischof, “In situ thermal denaturation of proteins in dunning AT-1 prostate cancer cells: implication for hyperthermic cell injury”, *Ann. Biomed. Eng.*, 32, 10, 1384–1398 (2004)
- [28] M.Y. Sfeir, F. Wang, L. Huang, C.C. Chuang, J. Hone, S.P. O’Brien, T.F. Heinz, L. E. Brus, “Probing electronic transitions in individual carbon nanotubes by Rayleigh scattering”, *Science*, 306, 5701, 1540–1543 (2004)
- [29] S. Kawata, *Near-Field Optics and Surface Plasmon Polaritons* (Springer, 2001)
- [30] P.B. Johnson, R.W. Christy, “Optical constants of the noble metals”, *Phys. Rev. B*, 6, 12, 4370–4379 (1972)
- [31] B.W. Garner, T. Cai, S. Ghosh, Z. Hu, A. Neogi, “Refractive Index change due to volume-phase transition in polyacrylamide gel nanospheres for optoelectronics and bio-photonics”, *Appl. Phys. Express*, 2, 057001 (2009)
- [32] R. Contreras-Cáceres, J. Pacifico, I. Pastoriza-Santos, J. Perez-Juste, A. Fernandez-Barbero, and L.M. Liz-Marzan, “Au@pNIPAM thermosensitive nanostructures: control over shell cross-linking, overall dimensions, and core growth”, *Adv. Funct. Mater.*, 19, 19, 3070–3076 (2009)
- [33] R.M.J. Cotterill, *Biophysics* (Wiley, 2002)

- [34] T. Okamoto, I. Yamaguchi, "Field enhancement by a metallic sphere on dielectric substrates", *Opt. Rev.*, 6, 3, 211–214 (1999)
- [35] P. Keblinski, D.G. Cahill, A. Bodapati, C.R. Sullivan, T.A. Taton, "Limits of localized heating by electromagnetically excited nanoparticles", *J. Appl. Phys.*, 100, 5, 054305 (2006)
- [36] J. Hofkens, J. Hotta, K. Sasaki, H. Masuhara, K. Iwai, "Molecular assembling by the radiation pressure of a focused laser beam: poly(N-isopropylacrylamide) in aqueous solution", *Langmuir*, 13, 3, 414–419 (1997)
- [37] S. Iwanaga, N.I. Smith, K. Fujita, S. Kawata, "Slow Ca(2+) wave stimulation using low repetition rate femtosecond pulsed irradiation", *Opt. Express*, 14, 2, 717–725 (2006)
- [38] J.M. McMahon, G.C. Schatz, S.K. Gray, "Plasmonics in the ultraviolet with the poor metals Al, Ga, In, Sn, Tl, Pb, and Bi", *Phys. Chem. Chem. Phys.*, 15, 5415–5423 (2013)
- [39] P.R. West, S. Ishii, G.V. Naik, N.K. Emani, V.M. Shalaev, A. Boltasseva, "Searching for better plasmonic materials", *Laser & Photonics Reviews*, 4, 6, 795–808 (2010)
- [40] H. Ehrenreich, H. Philipp, B. Segall, "Optical Properties of Aluminum", *Phys. Rev.* 132, 1918–1928 (1963)
- [41] R. LaVilla, H. Mendlowitz, "Optical Constants of Aluminum in Vacuum Ultraviolet", *Phys. Rev. Lett.* 9, 149–150 (1962)
- [42] H. Ehrenreich, H.R. Philipp, "Optical properties of Ag and Cu", *Phys. Rev.* 128, 1622–1629 (1962)
- [43] B.R. Cooper, H. Ehrenreich, H.R. Philipp, "Optical Properties of Noble Metals. II.", *Phys. Rev* 138, 494–507 (1965)
- [44] E.D. Palik, "Handbook of Optical Constants of Solids", Academic Press: New York Vol. 1 (1985)
- [45] C. Langhammer, M. Schwind, B. Kasemo, Igor Zorić, "Localized Surface Plasmon Resonances in Aluminum Nanodisks", *Nano Lett.*, 2008, 8, 5, 1461–1471 (2008)
- [46] G.H. Chan, J. Zhao, G.C. Schatz, R.P. Van Duyne, "Localized Surface Plasmon Resonance Spectroscopy of Triangular Aluminum Nanoparticles", *J. Phys. Chem. C*, 112, 36, 13958–13963 (2008)
- [47] Y. Ekinici, H. H. Solak, J. F. Löffler, "Plasmon resonances of aluminum nanoparticles and nanorods", *J. Appl. Phys.* 104, 083107 (2008)
- [48] A. Taguchi, Y. Saito, K. Watanabe, S. Yijian, S. Kawata, "Tailoring plasmon resonances in the deep-ultraviolet by size-tunable fabrication of aluminum nanostructures," *Appl. Phys. Lett.*, 101, 081110 (2012)

- [49] S.K. Jha, Z. Ahmed, M. Agio, Y. Ekinici, J. F. Löffler, "Deep-UV Surface-Enhanced Resonance Raman Scattering of Adenine on Aluminum Nanoparticle Arrays", *J. Am. Chem. Soc.*, 134, 4, 1966–1969 (2012)
- [50] A. Taguchi, N. Hayazawa, K. Furusawa, H. Ishitobi, S. Kawata, "Deep-UV tip-enhanced Raman scattering", *J. Raman Spectrosc.* 40, 1324-1330 (2009)
- [51] Y. Kumamoto, "深紫外ラマン分光顕微鏡による細胞内生体分子分析", PhD thesis, Osaka University, Osaka, Japan, p12 (2011)
- [52] Y. Saito, M. Honda, K. Watanabe, A. Taguchi, Y. Song, S. Kawata, "Design of Aluminum Nanostructures for DUV Plasmonics: Blue Shifts in Plasmon Resonance Wavelength by Height Control" *J. Jpn. Inst. Met.*, 77, 1, 27-31 (2013)
- [53] J. Henson, J. DiMaria, R. Paiella, "Influence of nanoparticle height on plasmonic resonance wavelength and electromagnetic field enhancement in two-dimensional arrays", *J. Appl. Phys.* 106, 093111 (2009)
- [54] S.M. Edlou, A. Smajkiewicz, G. A., Al-Jumaily, "Optical properties and environmental stability of oxide coatings deposited by reactive sputtering", *Appl. Opt.*, 32, 5601-5605 (1993)
- [55] M. Honda, Y. Saito, N.I. Smith, K. Fujita, S. Kawata, "Nanoscale heating of laser irradiated single gold nanoparticles in liquid" *Optics Express*, 19, 12375 (2011)

## Chapter 3 Photocatalysis with aluminum nanoparticles

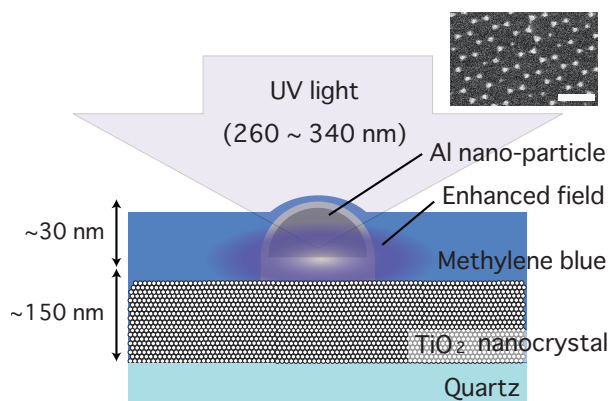


**Figure 3-1.** Schematic view of plasmon-enhanced photocatalyst. Al nanoparticles are placed on TiO<sub>2</sub> layer. The diameter of TiO<sub>2</sub> nanocrystal is ~6 nm. UV light illuminates the sample from the side of methylene blue layer. The enhanced field is generated in the vicinity of the Al nanoparticles. The shape of Al nanoparticles is approximated as either hemispherical or triangular. The inset shows a SEM image of hexagonally aligned Al nanoparticles. The scale bar indicates 500 nm. [1]

In the previous chapter, I showed LSPR wavelength of aluminum (Al) nanoparticles in the deep-UV range. For enhancement of photocatalysis, I aimed to use plasmonic enhancement in the deep-UV range. As a plasmonic material in UV range, Al was used because of physical stability derived from the oxidized layer. Figure 3-1 illustrates the concept of plasmon-enhanced photocatalysis. Briefly, a thin film of TiO<sub>2</sub> was deposited on a quartz substrate. Hexagonal patterns of Al nanoparticles were then formed on the surface of the TiO<sub>2</sub> film as shown in the inset using a lithographic method. To evaluate the photocatalytic activity, a test sample of methylene blue (MB) was applied to the substrate. By irradiating UV light from above the substrate, an enhanced field is generated in the vicinity of the Al nanoparticles, exciting the TiO<sub>2</sub> with an accelerated reaction. In this chapter, I firstly introduce nanosphere lithography

(NSL) as a fabrication technique of Al nanoparticles. For fabrication of aluminum, NSL is suitable in terms of difficulty in chemical synthesis of Al nanostructures due to its high ionization tendency. Then, I explain a rate reaction and experimental procedures. Finally I will show experimental results and discuss the mechanisms of enhancement.

### 3.1 Nanosphere lithography

Nanosphere lithography (NSL) originates from "Natural lithography" which was proposed in 1982. [2] In 1994, R. Van Duyne's group started to expand upon the technique. [3] His group developed into a fast and low cost fabrication method for the LSPR studies and SERS applications. [4-7] Then the technique was referred to as "Nanosphere lithography". NSL is a physical fabrication process of nanostructures with high resolution, low cost, and over large areas. Various patterns of nanostructures are produced by NSL, such as triangles, rings, pillars, disks, and crescents. [8]

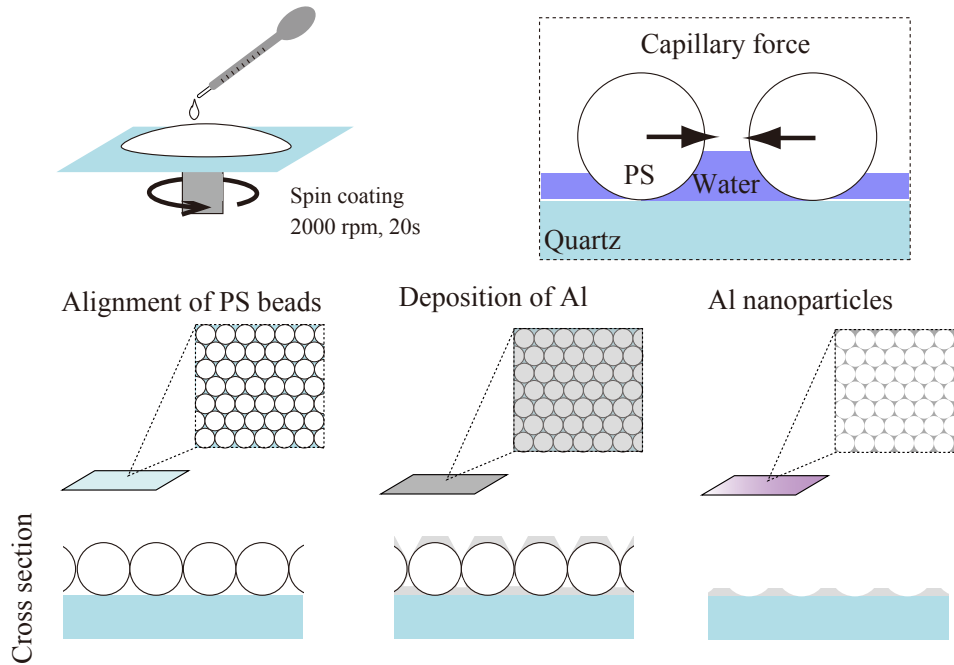
#### Mechanism of Nanosphere lithography

Figure 3-2 displays a schematic of NSL process. At first, polystyrene (PS) beads are aligned into hexagonal close-packing arrangement on to the substrate. Since the surface of PS beads is modified with negative charged groups ( $\text{COO}^-$  and  $\text{SO}_4^-$ ), the substrate is preliminarily washed in the piranha solution for being hydrophilicity of the substrate's surface. When the solvent of the PS solutions evaporates, the capillary force pushes PS beads each other and PS beads are self-assembled in the form of close packing. (See Figure 3-2) [9] The metals are evaporated from the above of PS beads under high vacuum. After removing PS beads, only metal nanostructures left. The shape of the nanostructures is equal to that of interspaces of PS beads. Therefore, the size of metal nanostructures depends on the diameters of PS beads and deposition thickness of metals. The length on a side and distance between corners are calculated from geometrics of NSL shown in Fig 3-3. They are written as:

$$\begin{aligned} AC &= (4 - 2\sqrt{3})d \\ BD &= (2\sqrt{3} - 3)d \end{aligned} \tag{3-1}$$

Here, AC is the distance on a side of triangle. BD is the height of the triangle.  $d$  is the diameter of PS beads. For example, when the diameter of PS beads is 320 nm, 85.74 nm and 74.26 nm for AC and BD are obtained. As seen in Figure 2-12, it was demonstrated that the

sizes of Al nanoparticles fabricated by NSL agree with those as expected. For precise control of the size of metallic nanostructures, I employed the NSL technique.



**Figure 3-2.** Experimental procedure of Nanosphere lithography and principle of self-assembly of PS beads. For self-assembly of PS beads, the solution of PS beads are dropped onto the substrate and spin-coated. When water is evaporated, each PS bead attaches each other by the capillary force. After aluminum is evaporated onto the template of PS beads and template is removed, Al nanostructures are left.

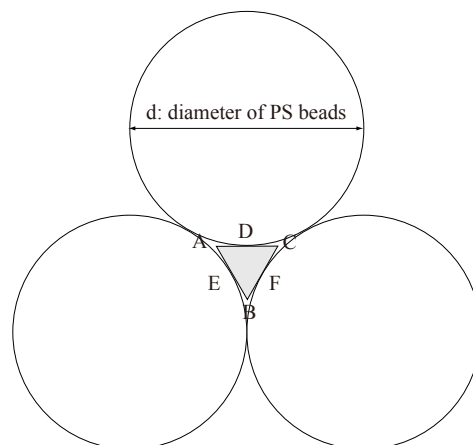


**Figure 3-3.** Geometries of typical NSL.

## Experimental procedure of NSL

At the beginning, quartz substrates are washed in piranha solution that is a mixture of  $\text{H}_2\text{O}_2$  and  $\text{H}_2\text{SO}_4$  with same mole. For investigation of photocatalysis, firstly, the  $\text{TiO}_2$  thin film was prepared by spin-coating anatase  $\text{TiO}_2$  nanocrystals (Titania Coating, Tayca Corporation, suspended in water) with a diameter of 6 nm on a quartz substrate. The spin-coating speed and time were 7000 rpm and 30 s, respectively. This process formed a  $\text{TiO}_2$  film with a thickness of  $\sim 150$  nm as shown in Figure 3-4. Polystyrene (PS) beads were aligned into a hexagonal close-packing arrangement on the  $\text{TiO}_2$  film by spin-coating. PS beads with diameters of  $107 \pm 2$  nm,  $147 \pm 7$  nm, and  $336 \pm 8$  nm (Microparticles GmbH) were used to investigate the size effect of the Al nanoparticles on plasmon resonance. [10] As shown in Figure 3-5, PS beads are well aligned on the  $\text{TiO}_2$  film because the surface of  $\text{TiO}_2$  is hydrophilic. Though some parts of PS beads are misaligned due to large roughness of  $\text{TiO}_2$  film, almost of all PS beads are well aligned. After that, Al was deposited on the substrate by thermal evaporation of an Al wire (99.99% purity) in vacuum conditions ( $\sim 2 \times 10^{-4}$  Pa). The evaporation speed was adjusted to 0.1 Å/s monitored with a quartz oscillator. The deposition thickness was 30 nm. The PS beads were then removed by sonication in toluene for 1 minute. With the 107 nm and 147 nm diameter PS beads, the shapes of the structures were hemispherical, and with the 336 nm diameter PS beads, the shape of the structure was triangular. The maximum widths were 28, 34, and 80 nm in ascending order of the PS bead size. Finally, to monitor the speed of the reactions, MB aqueous solution (200 mM) was spin-coated on the substrate at 7000 rpm for 30 s. The thickness of MB was estimated from its absorbance. The value of thickness was  $\sim 100$  nm.

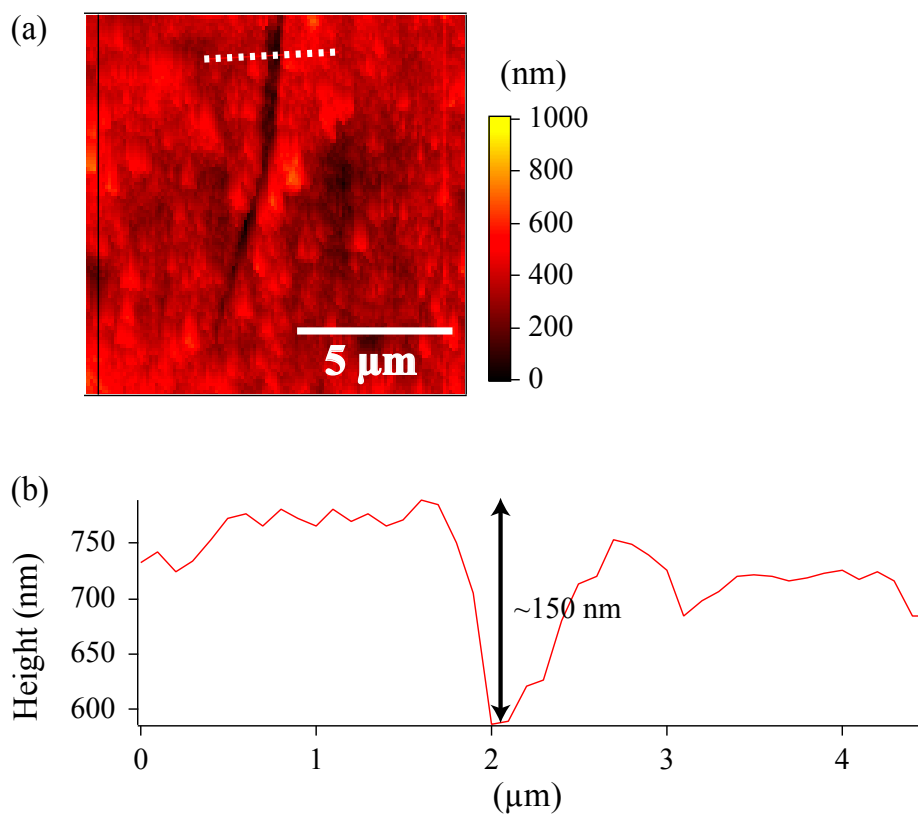


**Figure 3-4.** (a) An AFM image of the TiO<sub>2</sub> film. (b) Line profile at the white dotted line indicated in the AFM image. The spatial resolution of the atomic force microscope (AFM) is ~10 nm. Since the distance at the bottom shown in Figure 3-4 was 300 nm, measurement of the thickness was considered to be correctly performed.

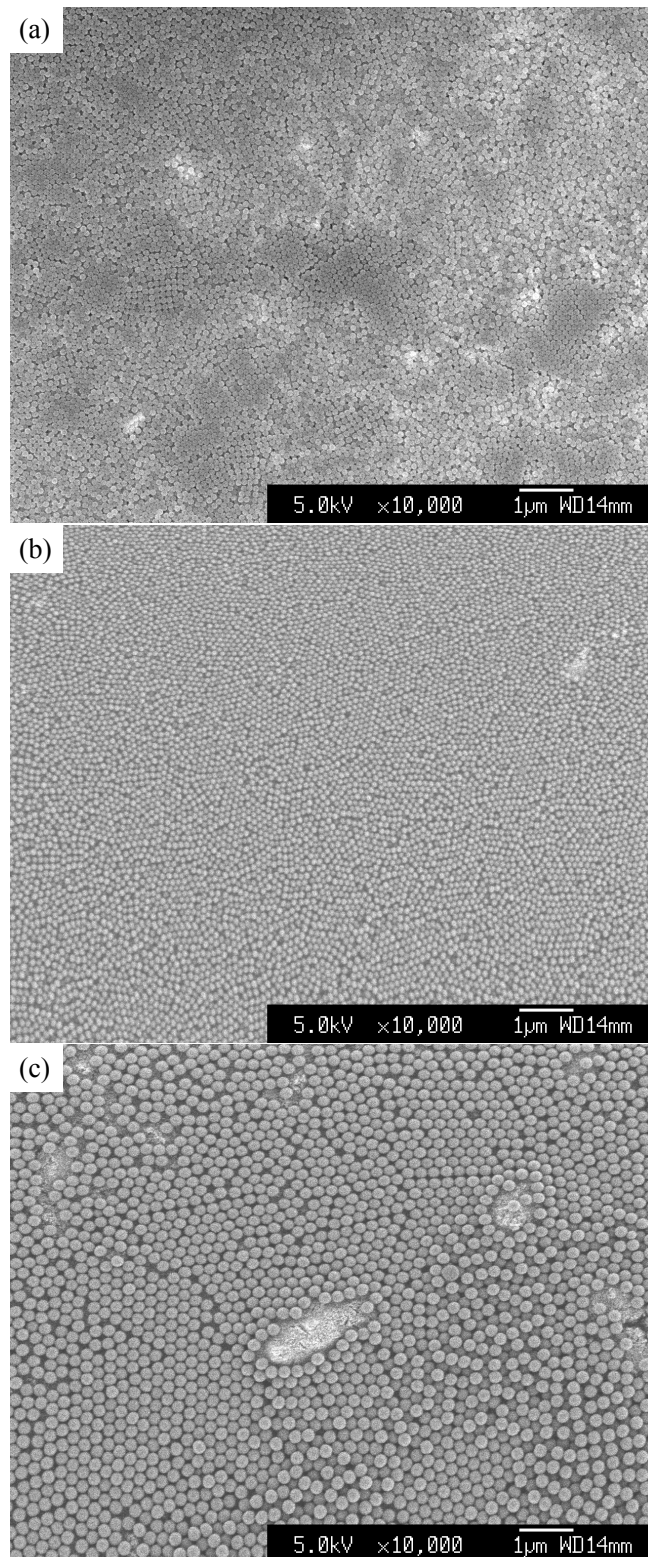


**Figure 3-5.** SEM images of PS beads aligned on the TiO<sub>2</sub> film. The sizes of PS beads are (a) 107 nm, (b) 147 nm, and (c) 336 nm.

### 3.2 Rate equation in photocatalysis

In order to investigate photocatalytic activity, methylene blue (MB) is generally used. [11] Figure 3-6 shows the structural formula of MB in photocatalysis. MB is reduced after receiving the electrons that are excited in TiO<sub>2</sub> by UV irradiation. When MB is exposed in air, MB is oxidized in photocatalytic reaction. Practically, it is known that MB is decomposed with some pathways. [12, 13] However, the process is complicated. In my experiment, I assumed that reactions are mainly reduction and oxidation because absorbance of MB was observed to be back to the initial value. This indicates that MB did not decomposed but just reduced. Then, the rate equation can be written as:

$$\begin{aligned}\frac{d [MB^+]}{dt} &= k_2[MB^+] - k_1[MB] \\ \frac{d [MB]}{dt} &= k_1[MB] - k_2[MB^+]\end{aligned}\tag{3-2}$$

In these equations, square brackets mean concentrations. Here,  $k_1$  and  $k_2$  are rate constants in reduction and oxidation reactions, respectively.  $k_1$  and  $k_2$  are described as also  $\frac{1}{\tau_1}$  and  $\frac{1}{\tau_2}$ , where  $\tau_1$  and  $\tau_2$  are time constants. By solving the system of equations, the concentration of oxidized MB is obtained as:

$$[MB^+] = C_0 \frac{k_2 + k_1 \exp\{-(k_1 + k_2)t\}}{k_1 + k_2}\tag{3-3}$$

$C_0$  indicates the initial concentration of MB. This temporal change of the concentration of MB is observed by monitoring absorbance of MB. Figure 3-5 shows extinction spectra of MB and TiO<sub>2</sub>. MB has the specific peak at 580 nm. In experiment, the absorbance at 580 nm shows that derived from also TiO<sub>2</sub> or Al in fabricating Al on the TiO<sub>2</sub> film. Therefore, the following equations are used to obtain time constants from experimental data. For the reaction without Al, the equation for curve fitting,  $f(t)$ , is written as:

$$f(t) = a + b \frac{k_2 + k_1 \exp\{-(k_1 + k_2)t\}}{k_1 + k_2}\tag{3-4}$$

Here,  $a$  and  $b$  mean background from  $\text{TiO}_2$  and the initial concentration of MB. To evaluate the enhancement of the photocatalytic reaction rate, curve fitting was performed using the following equation:

$$f(t) = A + B \frac{k_2 + k_1 \exp\{-(k_1 + k_2)t\}}{k_1 + k_2} + C \frac{k_2 + Fk_1 \exp\{-(Fk_1 + k_2)t\}}{Fk_1 + k_2} \quad (3-5)$$

Here,  $f(t)$  is a time-dependent function of the MB concentration during the photocatalytic reaction,  $A$  is the background signal,  $B$  and  $C$  indicate the initial concentration of area inside and outside of the enhanced field, respectively, and  $\tau_1$  and  $\tau_2$  are the time constants of the MB color degradation rate with and without Al particles, respectively. Because the photocatalytic activity is almost proportional to light intensity [14], I define the enhancement of the photocatalytic reaction rate as  $F$ . Since the reaction rate in reduction was observed to be an order of magnitude greater than that in oxidation, I fixed  $k_2$  as 0 in this experiment.

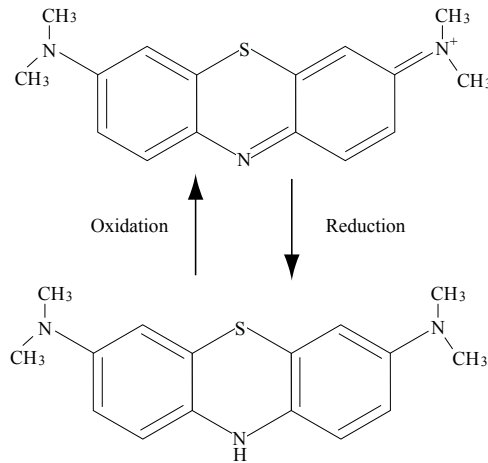


**Figure 3-4.** Structural formula of oxidized and reduced methylene blue.

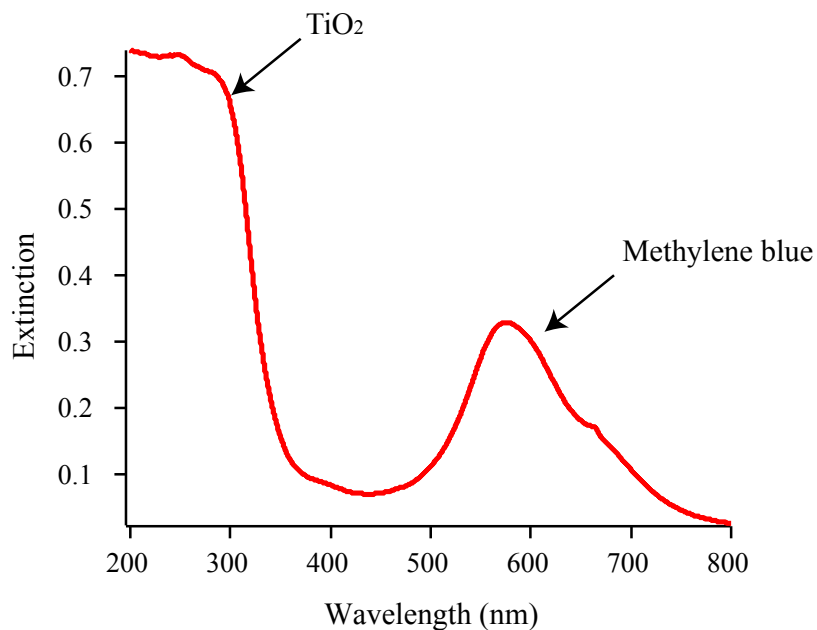


**Figure 3-5.** Extinction spectra of methylene blue on TiO<sub>2</sub>. In UV range, the absorption of TiO<sub>2</sub> is seen. The absorption peak at 580 nm is derived from methylene blue.

### 3.3 Experiment of photocatalysis with aluminum nanoparticles

The experimental setup for observing photocatalysis is shown in Figure 3-8. The photocatalytic reaction was initiated by irradiating the structures with UV light. The UV light source was a laser-driven light source (LDLS EQ-99, Tokyo Instruments, Inc.), which has a broad uniform spectrum from 170 nm to 800 nm. To avoid the effects of visible light, e.g., heat, UV light whose range is from 260 to 340 nm was extracted with a bandpass filter. The total intensity of the UV light was 8.1 mW/cm<sup>2</sup>. For examining wavelength dependence, another narrow bandpass filter with a bandwidth of 10 nm was additionally inserted. The intensity of the irradiation light became 0.57 mW/cm<sup>2</sup> at each wavelength. The absorption of MB was measured using a UV-Vis spectrometer (Shimadzu UV 3600, D2 lamp for UV, Halogen lamp for Vis) with a slit width of 0.2 nm. An absorption spectrum was measured every minute. The UV irradiation was stopped during the spectral measurements. The photocatalytic reaction was monitored using the absorption spectrum of MB centered at 580 nm. The absorption spectra of MB on TiO<sub>2</sub> with irradiation UV light are shown in Figure 3-8. As MB on TiO<sub>2</sub> is irradiated with UV light, the absorbance at 580 nm decreases because MB is reduced by photocatalysis. In

evaluating the reaction rate, each absorbance at 580 nm is plotted on the axis of integrated time of UV irradiation.

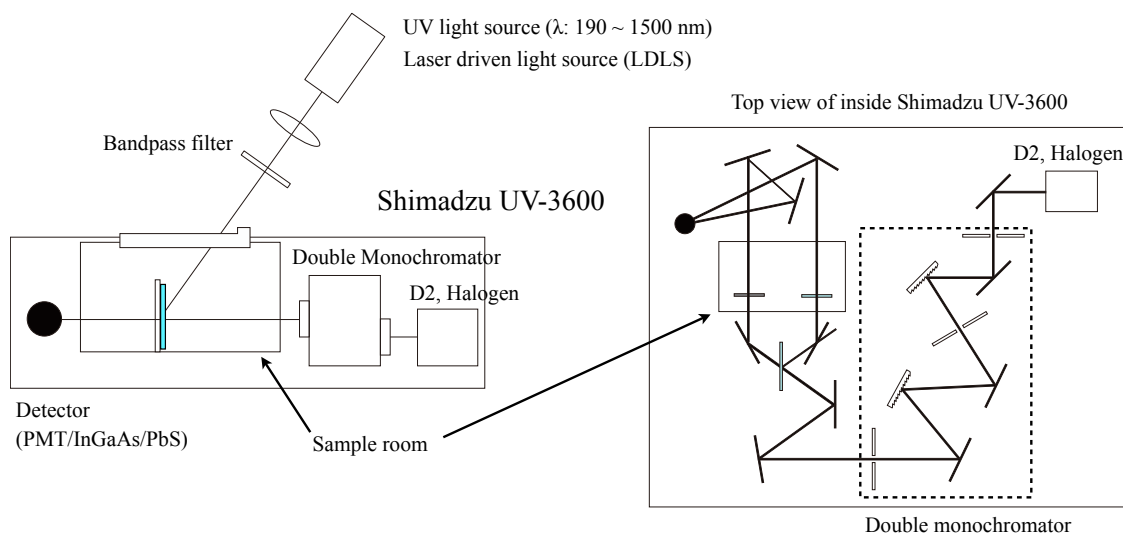


**Figure 3-8.** Optical setup for inducing and observing photocatalysis

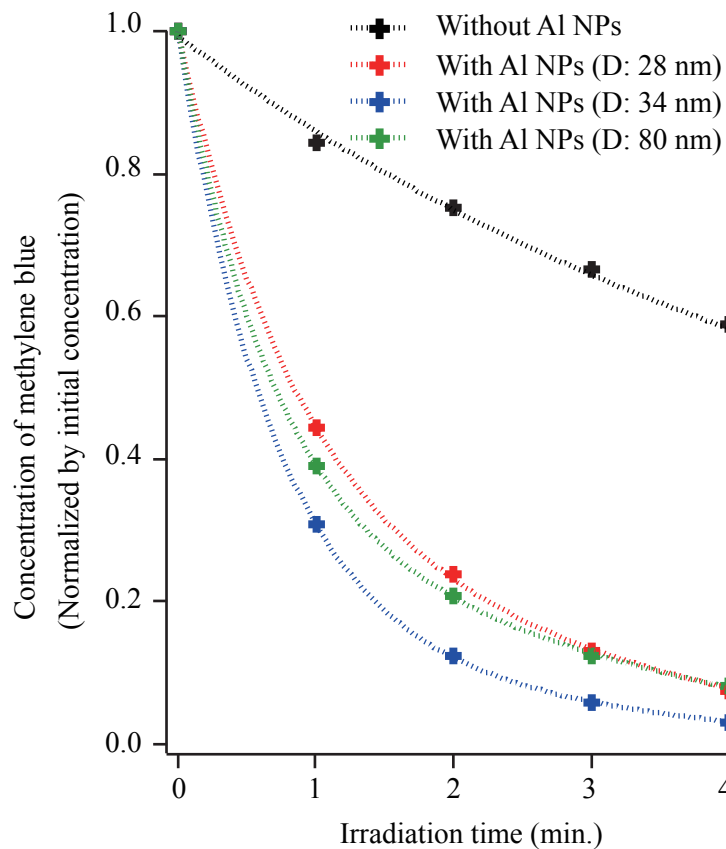
### 3.4 Photocatalysis with and without aluminum nanoparticles

Figure 3-7 shows the observed photocatalytic reaction of  $\text{TiO}_2$  with and without Al nanoparticles under the UV irradiation in the range 260-340 nm. The decay curves indicate the residual reaction rate of MB with respect to integrated irradiation time. The black line indicates the result without Al nanoparticles, whereas colored lines indicate the results with Al nanoparticles. The red, blue, and green colors indicate the rates obtained with Al nanoparticles having lateral sizes,  $D$ , of 28, 34, and 80 nm, respectively. For the 28 nm and 34 nm particles, the shape was approximated as a hemisphere, and for the 80 nm particles, the shape can be considered as a triangle.  $D$  is defined as the diameter of the hemisphere or the side length of the triangle. The height of the structure was the same as the evaporation thickness, that is, 30 nm. The net volume of the Al was actually smaller owing to surface oxidization. The estimated lateral sizes of the Al nanoparticles were 18 nm, 24 nm, and 70 nm.<sup>8</sup> Comparing the decay curves between samples with and without Al nanoparticles, the photocatalytic reaction rates of  $\text{TiO}_2$  with Al nanoparticles were remarkably enhanced. These results demonstrate clearly the plasmonic enhancement of photocatalysis on  $\text{TiO}_2$  by the UV-resonant Al nanoparticles.

The values of  $F$  with respect to lateral size  $D$  are summarized in Table 1. Al nanoparticles with the size of 34 nm showed the larger enhancements than 28 nm and 80 nm Al nanoparticles.

This is because the enhancement effect can be observed the most dominantly at the absorption edge of TiO<sub>2</sub> (320 nm). [15] At shorter wavelengths, TiO<sub>2</sub> shows high quantum efficiency to initiate photocatalytic reactions, while at longer wavelengths, the efficiency is decreased and the higher photon density was required. As a result, 34 nm Al nanoparticles, which have the resonance peak at 320 nm, achieved to the highest enhancements.

The 80 nm particles also show the larger enhancements as high as 12.9 than the 28 nm particles (exhibiting only 9.8). This can be because the 80 nm particles showed relatively high extinction efficiency at the band edge and also because they exhibit the high-integrated scattering efficiency at the wavelength region of 260 nm to 340 nm. Additionally, a triangular metallic nanoparticle in general supports the stronger electric field localized at the corner than a hemispherical metal nanoparticle. Therefore, the 80 nm triangular particle may have the advantage for plasmonic enhancement of photocatalytic reactions compared to the 28 nm hemisphere. In the case of photocatalysts other than TiO<sub>2</sub>, the size of the plasmonic structure needs to be tuned. Furthermore, Table 1 also shows the dependence of the photocatalytic enhancement on nanoparticle size. We note that the enhanced field means the area where the field intensity drops to  $1/e$  from the surface of the metal. In principle, as the diameter of the Al particles reduces, the  $1/e$  distance becomes shorter, while the thickness of the oxide layer increases because of the curvature. The area of the enhanced field therefore decreases dramatically with decreasing particle size, which could explain the size dependence of the photocatalytic enhancement.



**Figure 3-7.** Photocatalytic reactions with (colored) and without (black) Al nanoparticles under irradiation of UV light in the wavelength range of 260–340 nm. Red, blue, and green colors indicate the reaction obtained with Al nanoparticles having lateral sizes  $D = 28$ , 34, and 80 nm, respectively. [1]

**Table 3-1.** Summary of enhancement for each diameter of aluminum nanoparticle [1]

Size of Al NPs, D (nm)	Enhancement of photocatalytic reaction rate (F)
28	$9.8 \pm 0.8$
34	$14.3 \pm 0.9$
80	$12.9 \pm 0.8$

### 3.5 Irradiation wavelength dependence and enhancement mechanism

I investigated the dependence of the photocatalytic enhancement reaction on the irradiation wavelength. Figs. 3-8(a), 3-8(c), and 3-8(e) show the irradiation wavelength dependence of the photocatalytic enhancement for different values of  $D$ . Figs. 3-8(b), 3-8(d), and 3-8(f) show the calculated scattering efficiency corresponding to the structures in Figs. 3-8(a), 3-8(c), and 3-8(e), respectively. The wavelength axis in the simulation shows the converted wavelength which takes into account the effect of the  $\text{TiO}_2$  substrate. The insets in Figs. 3-8(b), 3-8(d), and 3-8(f) show the field distributions at a wavelength of 320 nm, at half the height of the particles. In Fig. 3-8(b) and 3-8(d), distinct scattering peaks at 330 nm and 320 nm were observed for the 28 nm and 34 nm particles. For the 80 nm particles, peaks were not seen because the spectral width was broadened due to the large size of the Al particles. Moreover, judging from the field distributions (insets in Figs. 3-8(b) and Figs. 3-8(d)), plasmon resonances at 330 and 320 nm are assigned to the dipole mode, whereas the shorter one at 280 nm in Figs. 3-8(b) is assigned to the quadrupole mode. For each  $D$ , the wavelength dependence of the enhancement agreed with the calculated scattering efficiency. The higher photocatalytic enhancement at the scattering peaks is consistent with the existence of a stronger near-field confinement. Taking these conditions into account, the spectral similarity of the enhancement and the scattering efficiency suggests that the enhancement of the photocatalytic reaction originates from the plasmonic properties of the Al nanoparticles. We estimated that an effect of “enhanced scattering” is smaller than the plasmonic effect because the particles are aligned in two dimensions and the density is low enough to avoid the effect of interactions between nanoparticles and multiple scattering between

the structures. Other chemical effects on the photocatalytic reaction, for example, charge transfer and forced electron–hole pair separation, are considered to be absent in this system because the Al nanoparticles are surrounded by  $\text{Al}_2\text{O}_3$  thick enough to avoid them.

The values of the enhancement in Figure 3-8 are not consistent with those in Table 3-1. The difference comes from the different intensity of irradiated UV light. With illumination of UV light at the intensity below  $\sim 100 \mu\text{W}/\text{cm}^2$ , the value of the quantum yield is the several percent ( $\sim 28\%$ ). With increasing the intensity of incident light from  $\sim 100 \mu\text{W}/\text{cm}^2$  to  $1 \text{ mW}/\text{cm}^2$ , the quantum yield decreases due to the saturation of absorption by  $\text{TiO}_2$ . According to the non-linearity of the quantum yield, I illustrate the relationship between the intensity of incident UV light and the amount of production as shown in Figure 3-9. The curve indicated in Figure 3-9 is resulting from multiplying the quantum yield by the intensity of the incident light. When the intensity of incident light is  $0.6 \text{ mW}/\text{cm}^2$ , the enhancement of  $\sim 2$  times is obtained resulting from the field enhancement of 10 times. On the other hand, the higher enhancement is obtained when the intensity of the incident light is  $8.1 \text{ mW}/\text{cm}^2$  with the field enhancements of 10 times.

In summary, the enhancement of photocatalytic activity in the deep-UV region was demonstrated using the plasmonic properties of Al nanostructures. A maximum increase to the photocatalytic reaction rate of about 14.3 times was obtained for particle sizes of 34 nm. Also the enhancement of the photocatalytic reaction rate was found to be dependent on plasmon resonance in the UV region, which was consistent with DDA simulation results. This study indicates the capability of utilizing UV plasmonic properties for the enhancement of photocatalyst performance where UV light is to be used. Plasmon-enhanced photocatalysis in the UV range is promising not only for conventional environmental applications but it also represents strategies for acquiring renewable and clean energy sources.

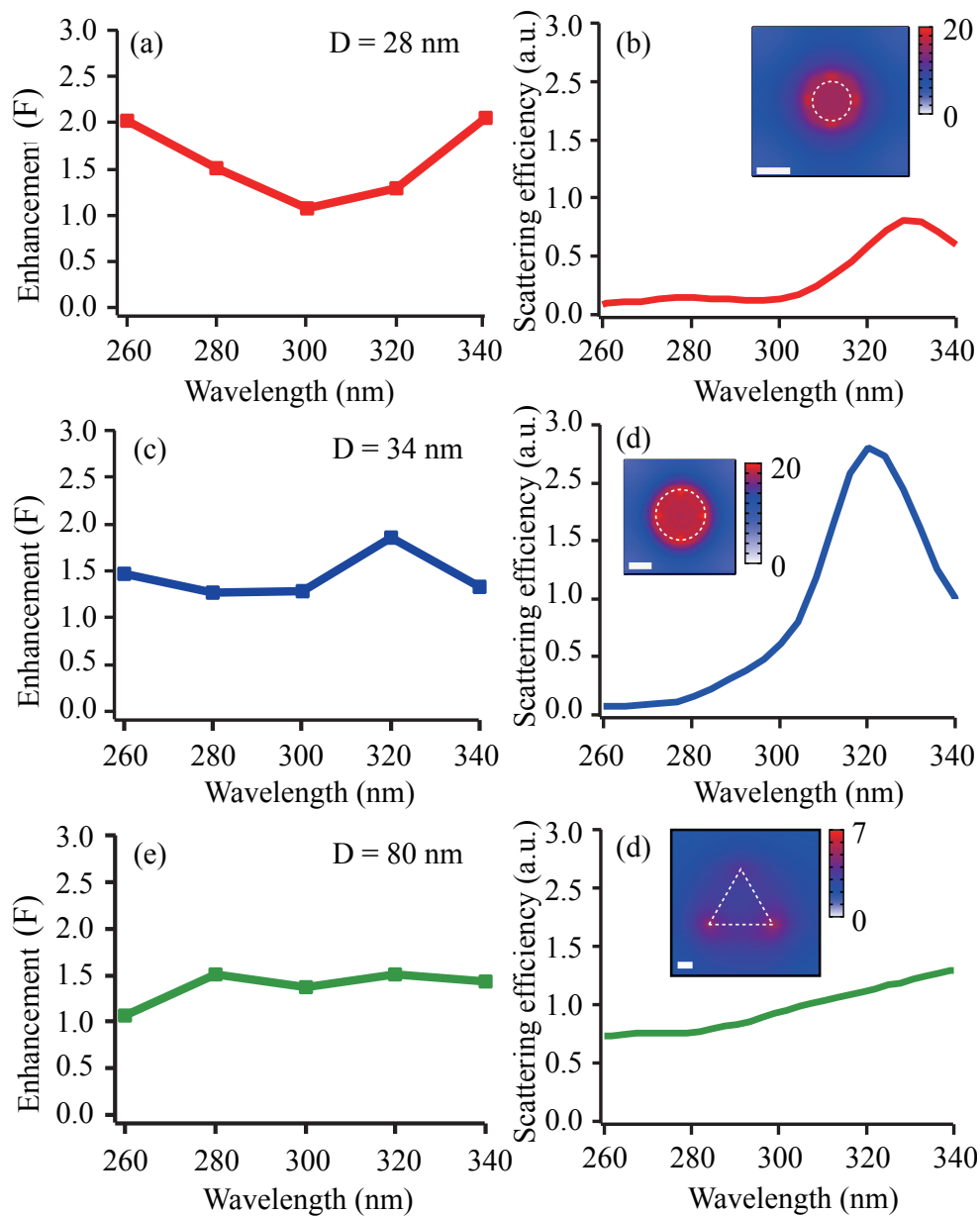


**Figure 3-8.** Wavelength dependence of photocatalytic reaction enhancement. (a), (c), (e) Experimental results with lateral sizes  $D = 28, 34,$  and  $80$  nm. (b), (d), (f) Calculated scattering efficiency of Al nanoparticles corresponding to (a), (c), and (e), respectively. Insets show the cross-sectional view of the near-field distribution at a wavelength of  $320$  nm at the middle height of the particle. The color bar shows the field enhancement  $E_{NF}/E_0$ , where  $E_{NF}$  and  $E_0$  indicate the field intensities of the near-field and the incident light, respectively. White dotted lines in the insets indicate the outlines of Al nanoparticles. The scale bars indicate  $10$  nm. [1]

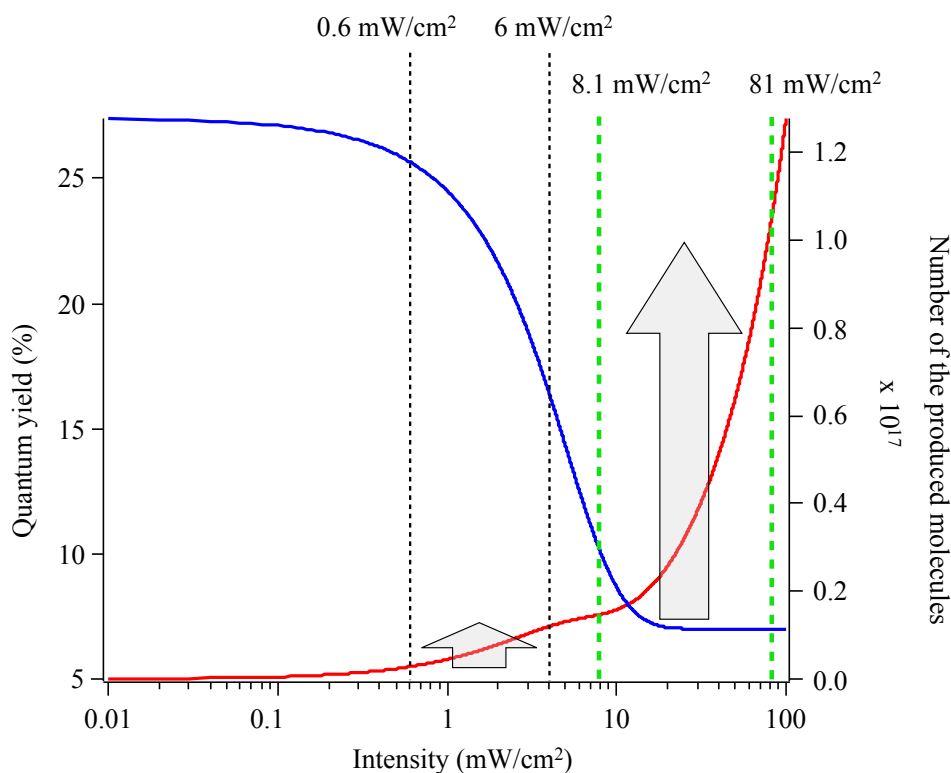


Figure 3-9. Relationship between the quantum yield and the intensity of the incident light (Blue), and relationship between the number of the produced molecules and the intensity of the incident light (Red). Black and green dotted lines indicate the intensity of the incidence and enhanced field that is generated by the incident intensity of  $0.6 \text{ mW/cm}^2$  and  $8.1 \text{ mW/cm}^2$ . Gray arrows indicate enhancements of the number of produced molecules.

## References

- [1] M. Honda, Y. Kumamoto, A. Taguchi, Y. Saito, S. Kawata, "Plasmon-enhanced photocatalysis", *Applied Physics Letters* (in press)
- [2] H.W. Deckman, J.H. Dunsmuir, "Natural lithography", *Applied Physics Letters*, 37, 411 (1982)
- [3] T.R. Jensen, M.D. Malinsky, C.L. Haynes, R.P. Van Duyne, "Nanosphere Lithography: Tunable Localized Surface Plasmon Resonance Spectra of Silver Nanoparticles", *J. Phys. Chem.*

B, 104, 45, 10549–10556 (2000)

[4] M.D. Malinsky, K.L. Kelly, G.C. Schatz, R.P. Van Duyne, "Nanosphere Lithography: Effect of Substrate on the Localized Surface Plasmon Resonance Spectrum of Silver Nanoparticles", *J. Phys. Chem. B*, 105, 2343-2350 (2001)

[5] L.J. Sherry, R. Jin, C.A. Mirkin, G.C. Schatz, R.P. Van Duyne, "Localized Surface Plasmon Resonance Spectroscopy of Single Silver Triangular Nanoprisms", *Nano Lett.*, 6, 9, 2060–2065 (2006)

[6] J.N. Anker, W.P. Hall, O. Lyandres, N.C. Shah, J. Zhao, R.P. Van Duyne, "Biosensing with plasmonic nanosensors", *Nature Materials*, 7, 442-453 (2008)

[7] C.L. Haynes, R.P. Van Duyne, "Plasmon-Sampled Surface-Enhanced Raman Excitation Spectroscopy", *J. Phys. Chem. B*, 107, 7426-7433 (2003)

[8] A. Kosiorek, W. Kandulski, H. Glaczynska, M. Giersig, "Fabrication of nanoscale rings, dots, and rods by combining shadow nanosphere lithography and annealed polystyrene nanosphere masks", *Small*, 1, 4, 439–444 (2005)

[9] N. Denkov, O. Velev, P. Kralchevski, I. Ivanov, H. Yoshimura, K. Nagayama, "Mechanism of formation of two-dimensional crystals from latex particles on substrates", *Langmuir*, 8, 12, 3183–3190 (1992)

[10] Y. Saito, M. Honda, K. Watanabe, A. Taguchi, Y. Song, S. Kawata, "Design of Aluminum Nanostructures for DUV Plasmonics: Blue Shifts in Plasmon Resonance Wavelength by Height Control," *J. Jpn. Inst. Met.*, 77, 1, 27-31 (2013)

[11] K. Hashimoto, "第5版 実験化学講座 25 - 触媒化学, 電気化学-", 社団法人日本化学会, p111-p148 (2007)

[12] C.H. Wu, J.M. Chern, "Kinetics of Photocatalytic Decomposition of Methylene Blue", *Ind. Eng. Chem. Res.*, 45, 6450-6457 (2006)

[13] A. Houas, H. Lachheb, M. Ksibi, E. Elaloui, C. Guillard, J.M. Herrmann, "Photocatalytic degradation pathway of methylene blue in water", *Applied Catalysis B: Environmental*, 31, 145–157 (2001)

[14] Y. Ohko, K. Hashimoto, A. Fujishima, "Kinetics of Photocatalytic Reactions under Extremely Low-Intensity UV Illumination on Titanium Dioxide Thin Films", *J. Phys. Chem. A*, 101, 8057-8062 (1997)

[15] N. Serpone, D. Lawless, R. Khairutdinov, "Size Effects on the Photophysical Properties of Colloidal Anatase TiO<sub>2</sub> Particles: Size Quantization or Direct Transitions in This Indirect Semiconductor?", *J. Phys. Chem.*, 99, 16646 (1995).

- [16] S. Ikeno, T. Kawabata, H. Hayashi, K. Matsuda, S. Rengakuji, T. Suzuki, Y. Hatano, K. Tanaka, "Fabrication of Photocatalytic TiO<sub>2</sub> Films on Pure Aluminum Plates", *Mater. Trans.*, 43, 5, 939 (2002)
- [17] E.D. Palik, "Handbook of Optical Constants of Solids", Academic Press: New York Vol. 1 (1985)
- [18] Y. Ohko, K. Hashimoto, A. Fujishima "Kinetics of Photocatalytic Reactions under Extremely Low-Intensity UV Illumination on Titanium Dioxide Thin Films", *J. Phys. Chem. A*, 101, 8057 (1997) (1998)

## Chapter 4 Oblique angle deposition for aluminum nanoparticles

Oblique angle deposition (OAD) is a powerful method to fabricate metal nanoparticles with controlled sizes, shapes and higher density comparing to nanosphere lithography (NSL). [1-3] Generally, OAD has been used for surface-enhanced Raman spectroscopy (SERS), metal-enhanced fluorescence (MEF), surface-enhanced infrared spectroscopy (SEIRA), LSP sensors and metamaterials. [4-7] I employed OAD for increasing the density of aluminum particles on the TiO<sub>2</sub> film for better enhancement than results that I have shown in the previous chapter. Firstly, I'm going to introduce the method of OAD. Soon after, I show experiments of observing the enhanced photocatalysis and discuss experimental results from the viewpoints of reaction rates, amount of production and the origin of enhancement.

### 4-1. The method of oblique angle deposition

The principle of OAD is shown in Figure 4-1. Aluminum is deposited onto the substrate by thermal evaporation under high vacuum. At the beginning of the deposition, metallic vapor flows to create crystal seeds randomly onto the substrate. As the crystal seeds grow, taller crystals generated shadow behind themselves when the target substrate for deposition is tilted. The metallic crystals at the shadow do not grow. As a result, rough surfaces or metallic particles are created. The deposition thickness determines separation or connection of Al nanoparticles.

Design of the evaporation system for OAD and a picture of the system for the tilting substrates are shown in Figure 4-2. I controlled the angle of the substrates by tuning the inclined angle  $\theta$  indicated in Fig 4-2. The thickness of deposition was monitored by a quartz crystal microbalance (QCM) as shown in Figure 4-2. Structural parameters of diameters, height and density depend on deposition parameters of tilting angle, thickness and deposition rate. With increasing the tilt angle of the substrate,  $\theta$ , the density of nanoparticles becomes low because of the shadowing effect. With increasing the deposition thickness, diameters and heights become larger due to crystal growth.

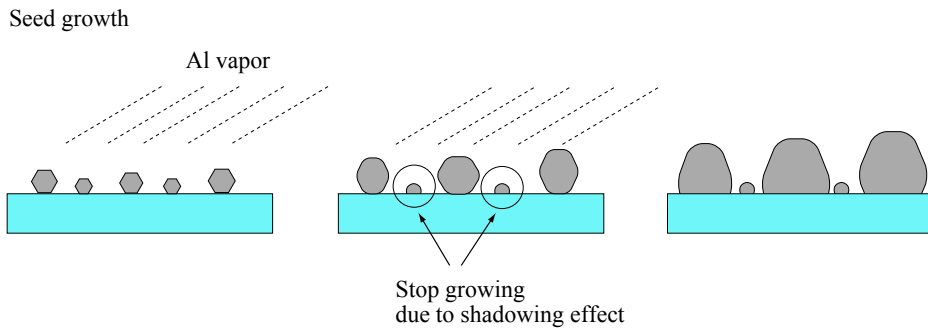


**Figure 4-1.** Principle of particles growth by oblique angle deposition (OAD). When the vapor of aluminum is incident at a certain angle, aluminum seeds were produced at the surface of the substrate. As the size of particles grows, some particles stop to grow due to the shadow of higher particles. Finally, aluminum nanoparticles can be obtained.

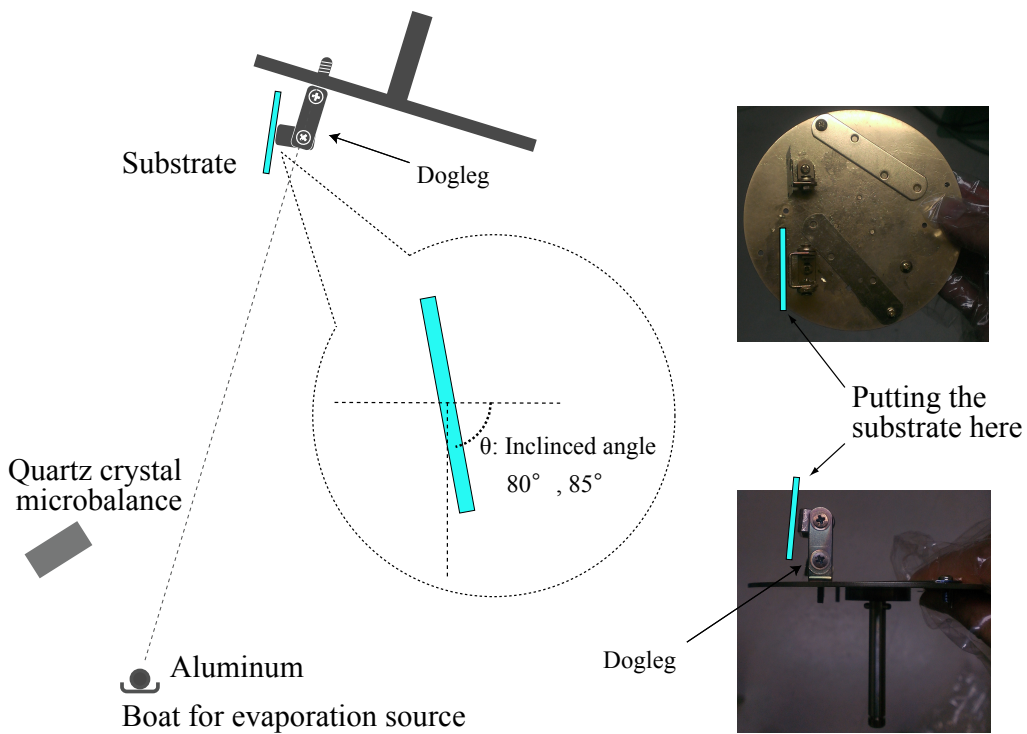


**Figure 4-2.** A system for OAD (left) and pictures of the stage to incline the substrate. (Right) Evaporation source is aluminum put on the tungsten boat. The thickness of deposition is monitored by a quartz crystal microbalance. The vapor of aluminum goes straight to the disk. The substrate is fixed on the small dogleg. Screwing controls the incident angle of aluminum vapor.

In order to confirm the effect of the tilting angles in fabrication of Al nanoparticles, Al was evaporated on the quartz substrate with changing tilting angles from 0 to 80 degrees at the deposition thickness of 30 nm. Figure 4-3 shows AFM images, extinction spectra. Less than 80 degrees of tilt angle, larger diameters and various shapes of aluminum nanoparticles are seen in Figure 4-3 while homogeneous particles are seen above 80 degrees. In agreement with the size and uniformity change, the peak shapes become sharp with increasing the angle. Furthermore, plasmon resonance wavelengths gradually shift to shorter wavelengths. This is because sizes of Al grain become smaller and, consequently Al nanoparticles are formed. These results tell that OAD can be applicable to production of aluminum nanoparticles. In addition, it is indicated that changing the inclined angle of the quartz substrate controls aspect ratio, the diameters and heights of aluminum nanoparticles.

To control diameter and height of Al nanoparticles, Al was evaporated with various deposition parameters. The tilting angles of the substrate were fixed at 80 and 85 degrees because Al nanoparticles were formed with more than 80 degrees. Deposition thickness was changed from 20 nm to 70 nm. Deposition rates were 0.1 and 0.5 Å/s. The vacuum degree inside the chamber was  $\sim 10^{-5}$  Pa. Figure 4-4, 4-5, 4-6, and 4-7 are AFM images of aluminum nanoparticles fabricated by OAD on quartz substrate. From AFM images, I measured averaged particles' diameters and heights by hand.

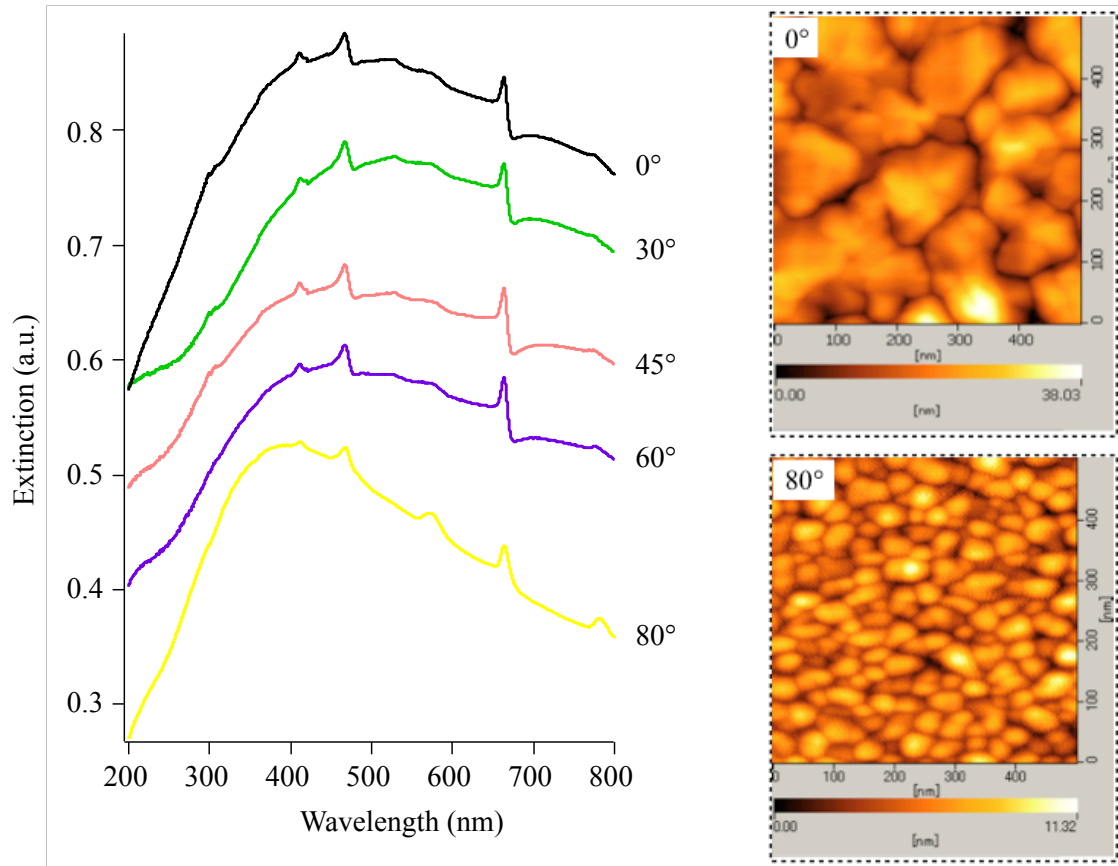


**Figure 4-3.** Extinction spectra of Al deposited with various inclined angles of the substrates (left) and AFM images of Al nanoparticles fabricated with the tilt angles of 0 and 80 degrees (right).

**Table 4-1.** Relationship between structural and deposition parameters.

	diameter	height	density
inclined angle ↑		↑	↓
deposition thickness ↑	↑	↑	↓
deposition rate ↑	↑		↑

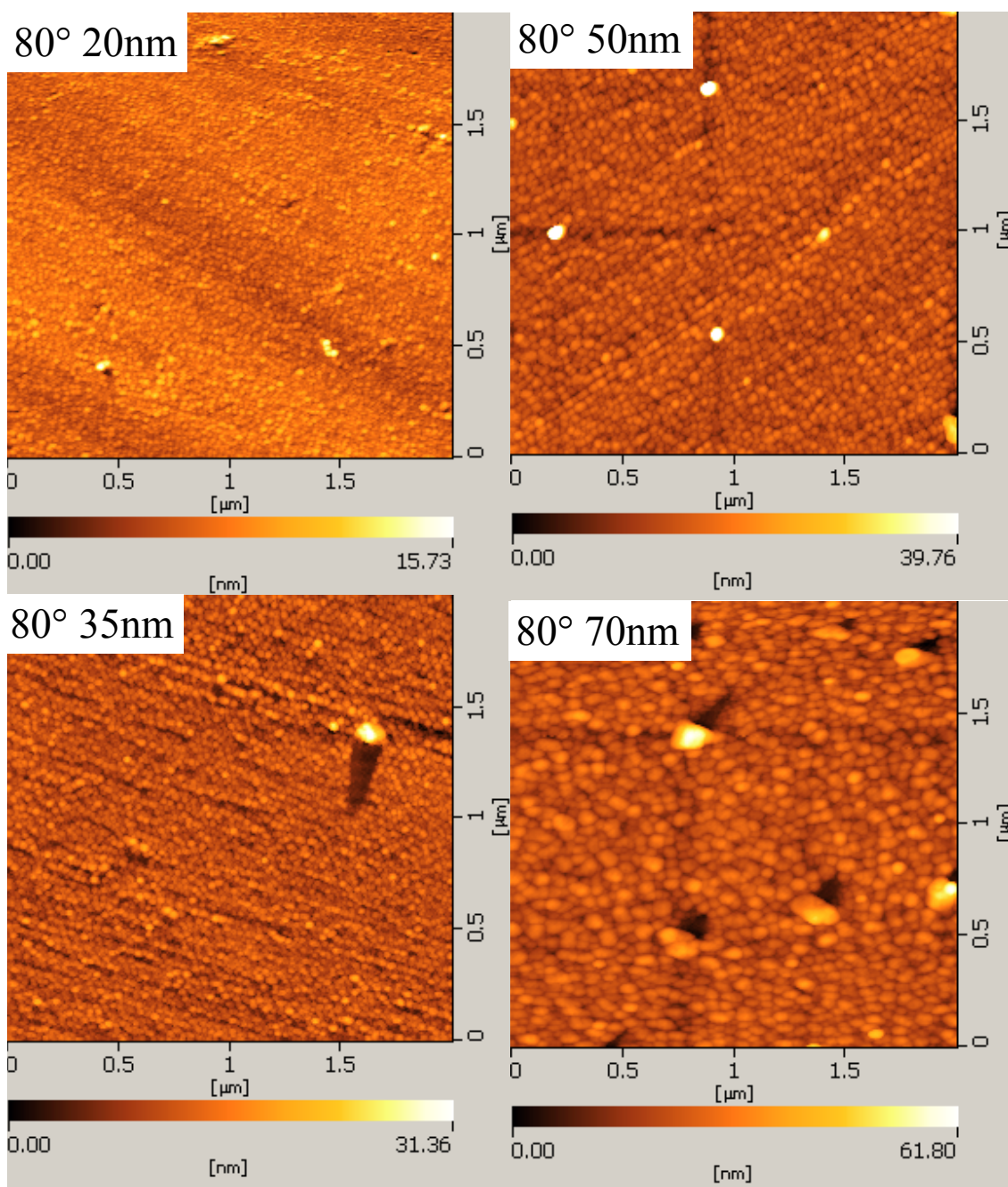


**Figure 4-4.** AFM images of aluminum nanoparticles fabricated by OAD. The tilt angles of 80 degrees. The deposition thicknesses of Al nanoparticles are 20, 35, 50 and 70 nm. The deposition rate was 0.5 Å/s. The colored bars indicate the height of Al nanoparticles.

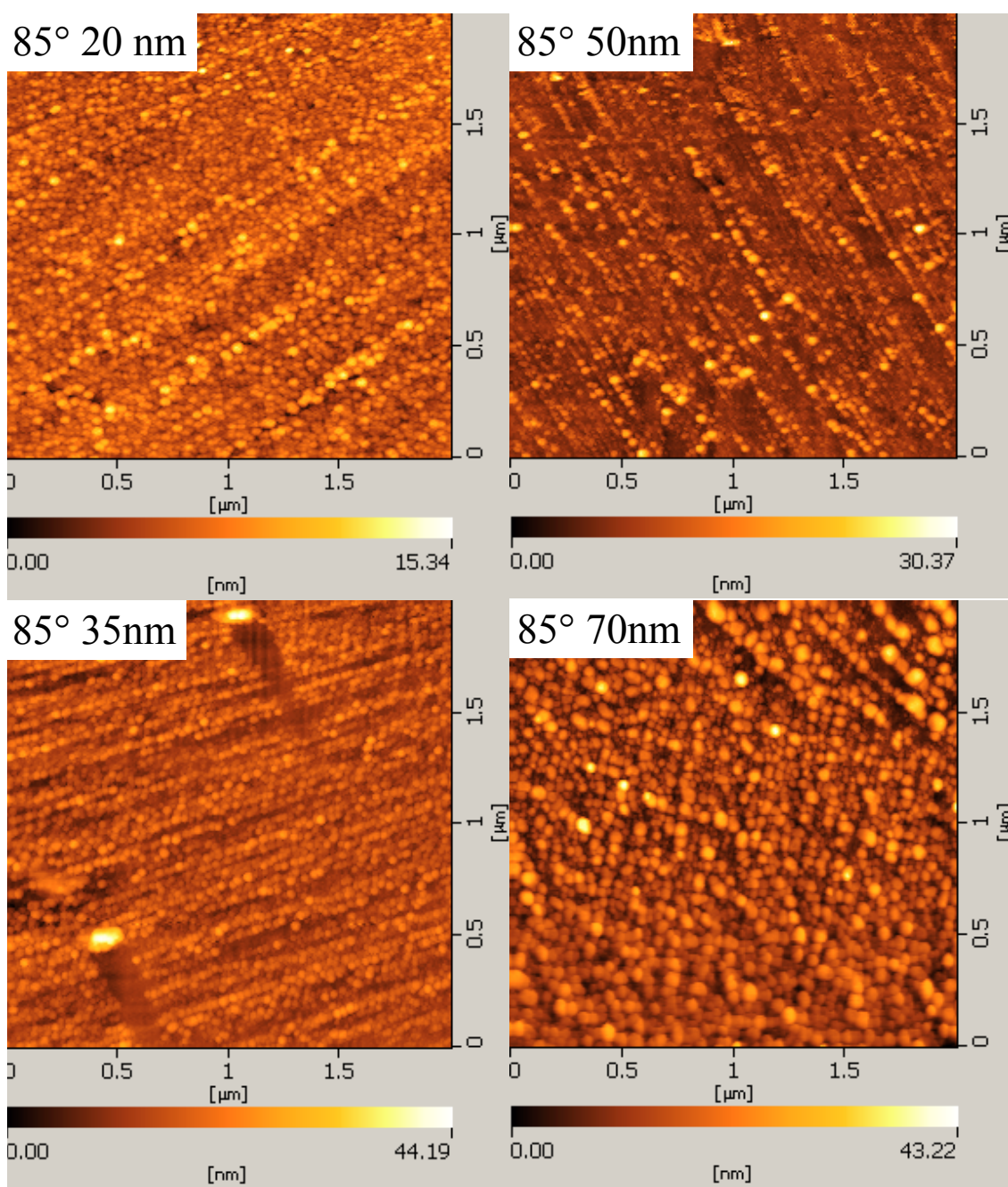


**Figure 4-5.** AFM images of aluminum nanoparticles fabricated by OAD. The tilt angles of 85 degrees. The deposition thicknesses of Al nanoparticles are 20, 35, 50 and 70 nm. The deposition rate was 0.5 Å/s. The colored bars indicate the height of Al nanoparticles.

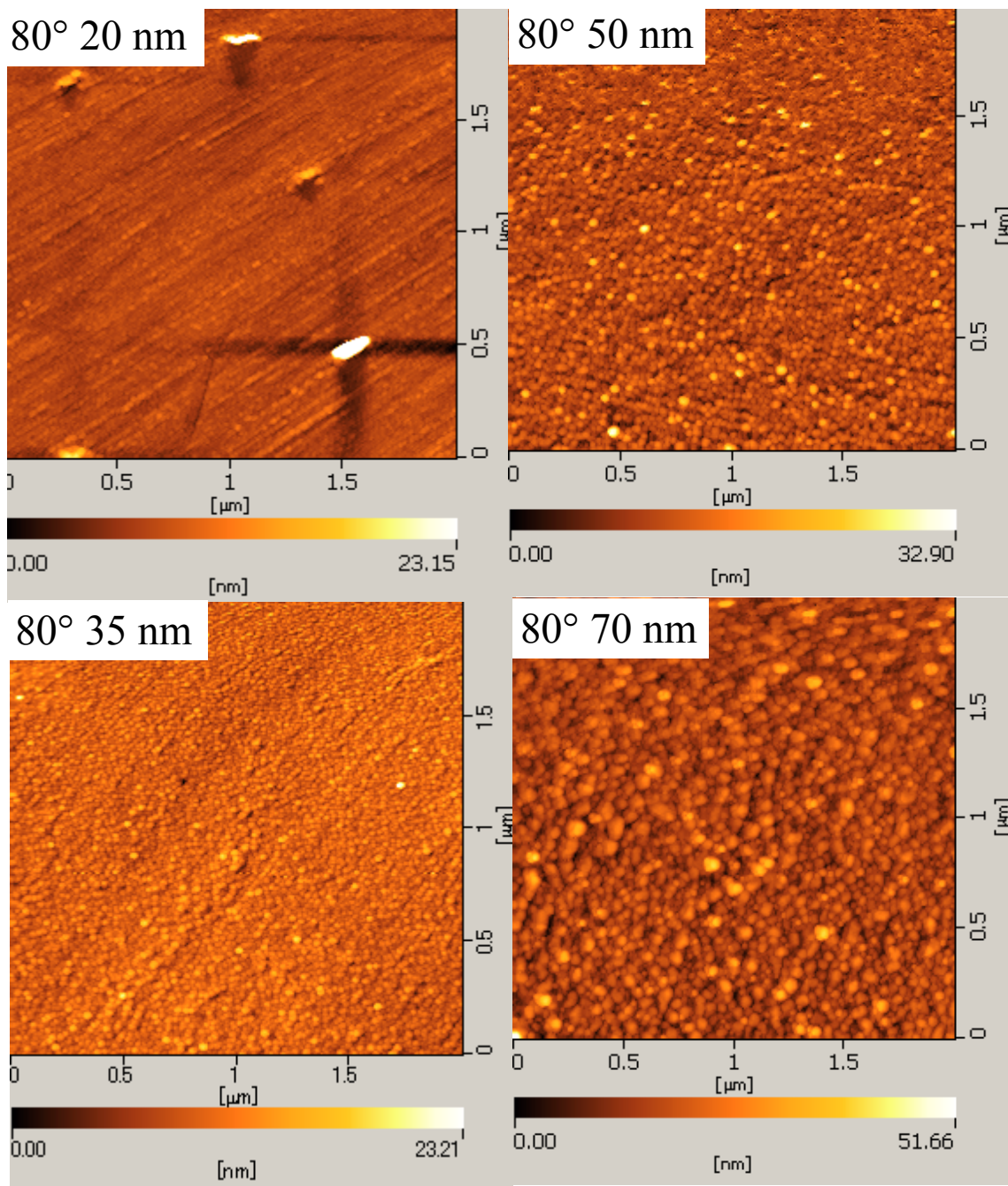


**Figure 4-6.** AFM images of aluminum nanoparticles fabricated by OAD. The tilt angles of 80 degrees. The deposition thicknesses of Al nanoparticles are 20, 35, 50 and 70 nm. The deposition rate was 0.1 Å/s. The colored bars indicate the height of Al nanoparticles.

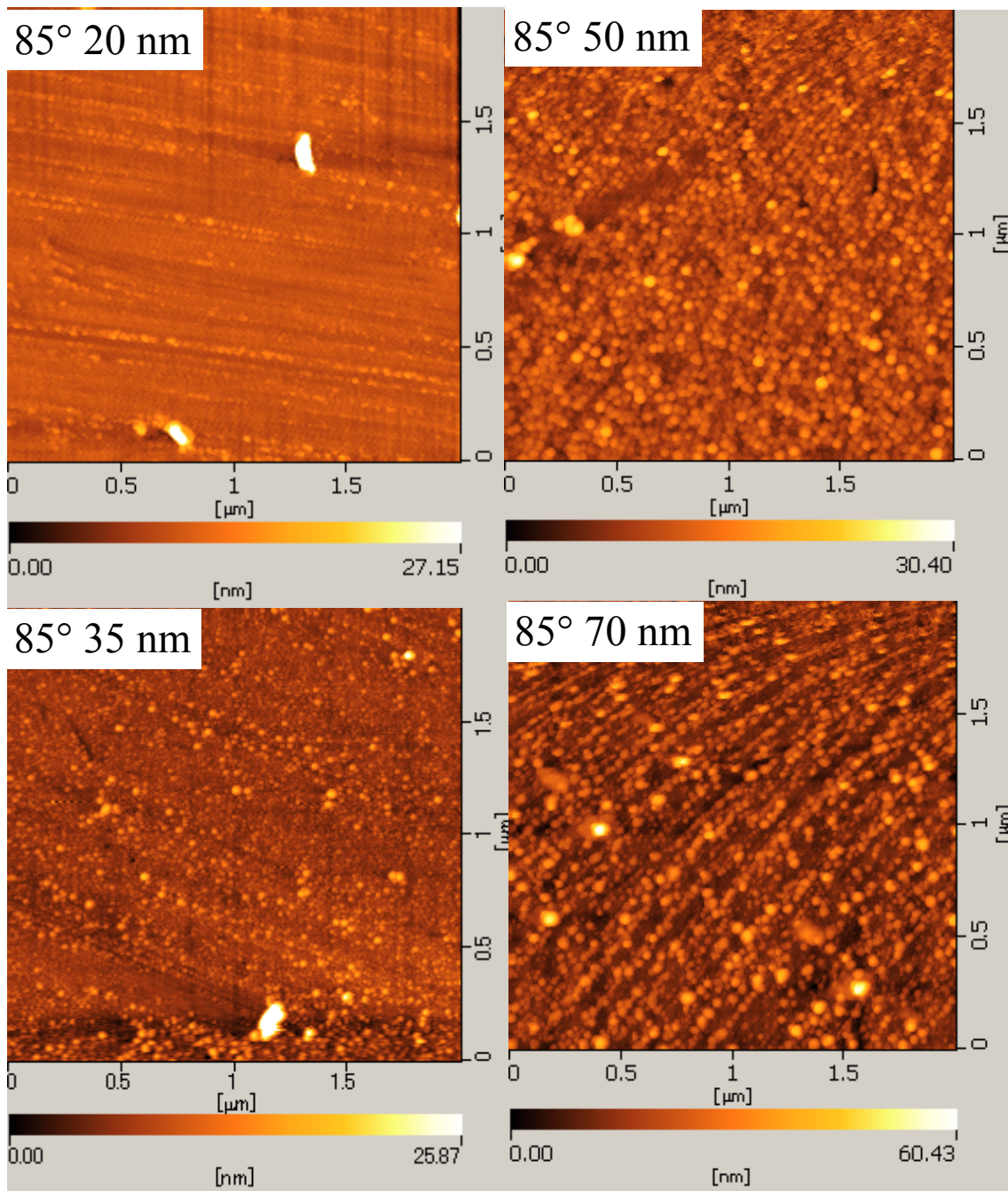


**Figure 4-7.** AFM images of aluminum nanoparticles fabricated by OAD. The tilt angles of 85 degrees. The deposition thicknesses of Al nanoparticles are 20, 35, 50 and 70 nm. The deposition rate was 0.1 Å/s. The colored bars indicate the height of Al nanoparticles.

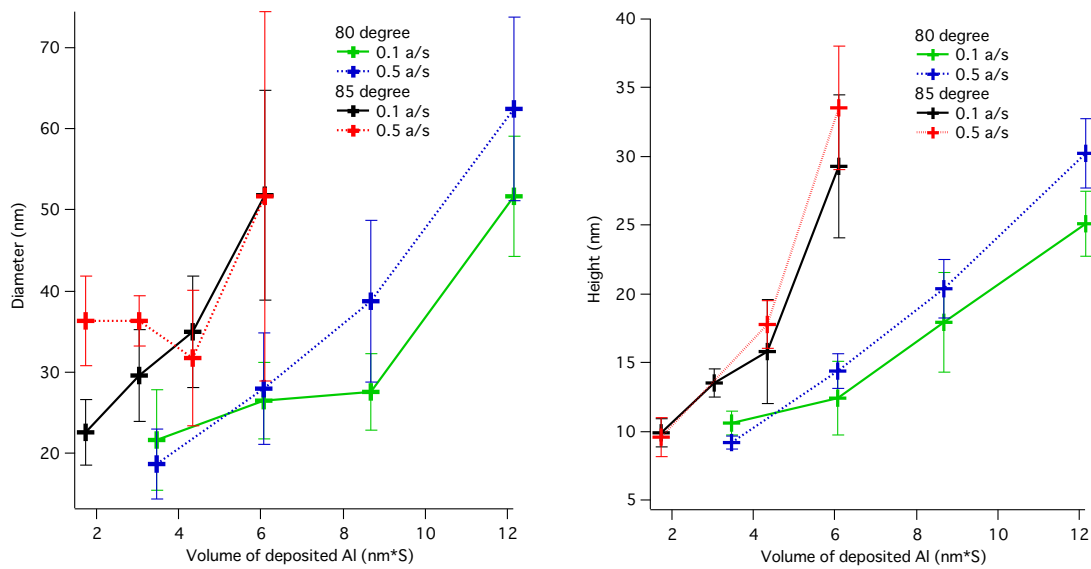


**Figure 4-8.** Relationship between volume of deposited aluminum and diameters of aluminum nanoparticles (left), height (right). Green and blue lines show the results with the tilt angle of 80 degrees, and black and red lines with 85 degrees. Dotted and solid lines mean fabrication at the deposition rate of 0.5 Å/s and 0.1 Å/s.

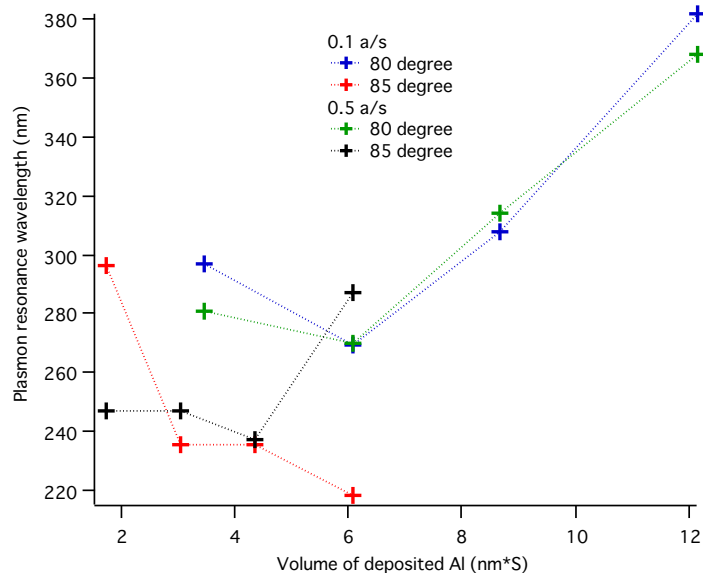


**Figure 4-9.** Relationship between the volume of deposited aluminum and plasmon resonance wavelength. Blue and red marks show plasmon resonance wavelength fabricated with 80 and 85 degrees of tilt angles at the deposition rate of 0.1 Å/s. Green and black marks shows plasmon resonance wavelength fabricated with 80 and 85 degrees of inclines angles at the deposition rate of 0.5 Å/s.

Figure 4-8 show the relationship between the volume of deposited aluminum and structural parameters, diameters and heights. With depositing aluminum, both diameters and height of Al nanoparticles increased. At the early stage of fabrication of aluminum, gradient of increment of diameters and heights tends to be smaller than the later stage. This is derived from the shadow effect. As the heights of particles increase, the area of hidden places by particles becomes larger. The aluminum that is supposed to be deposited in the shadowed area was used for particles' growth. In the early stage of deposition at the inclined angle of 85 degrees and the deposition rate of 0.5 Å/s, the diameter of Al nanoparticles does not change with evaporating Al. This means that only the height increased in the stage. I guess that larger shadowing effect induced height's increment because the condition of higher speed of deposition made Al atoms go to the substrate more straightly. Error bars become larger with deposition of Al. This suggests that uniformity of particles' sizes become worse due to shadowing effect. As particles become taller, shadowing effect getting to be larger, and as a result, more particles stop growing due to neighboring taller particles.

Figure 4-9 is relationship between the volume of deposited aluminum and plasmon resonance wavelength. Plasmon resonance wavelengths are measured by UV-Vis spectrometer. The sizes shown in Figure 4-9 explains the behavior of plasmon resonance wavelengths well. At smaller amount of deposition, plasmon resonance wavelengths shift to shorter wavelengths. This is because the heights of particles numbered up. After that, aluminum nanoparticles grow up in a radial direction and height direction at the same rate. Therefore, plasmon resonance wavelengths just shift to longer wavelength by increasing sizes. With higher inclined angle, density of aluminum nanoparticles becomes small because of the net volume of aluminum decrease with higher angle. With increasing the angle, the height of aluminum nanoparticles tends to increase while the diameter of particles become less than that with smaller angles. The aluminum particles were separated each other enough not to cause longer PRW. This relationship between structural and deposition parameters is summarized in table 4-1. Up and down arrows mean increment and decrement of parameters.

## **4-2. Experiment of enhanced photocatalysis**

With the same way that I showed in chapter three, TiO<sub>2</sub> films were formed by spin-coating. Al nanoparticles were fabricated by OAD methods. The conditions of fabrication are as follows.

- Deposition thickness: 20, 35, 50, 70 nm (monitored by QCM)
- Inclined angle: 80, 85 degrees
- Deposition rates: 0.1, 0.5 Å/s

With aluminum nanoparticles fabricated by OAD, I observed photocatalysis by monitoring the absorbance decay of methylene blue with irradiating UV light whose range was from 260 to 340 nm. Experimental setup for observation of photocatalysis and the way for the evaluation of photocatalytic reaction rates are same with the way in the chapter three.

Figure 4-10, 4-11, 4-12 and 4-13 show photocatalytic reaction with and without aluminum nanoparticles fabricated by OAD. The largest enhancement of reaction rates, 10 times, was obtained with using Al nanoparticles with the diameter of 28 nm and the height of 14.4 nm. The largest amount of production was obtained with Al nanoparticles with the diameter of 26 nm 22.6 nm and height of 9 nm. Comparing the results with the deposition rate of 0.1 Å/s to those with 0.5 Å/s, lower deposition rate lead more production. Overmuch covering of TiO<sub>2</sub> surface by aluminum decreased the amount of reduced MB. For example, 80 degrees of the inclined angle and 0.5Å/s of the deposition rate caused decrement of the amount. The other cases exhibited enhancement of production amount by photocatalysis.

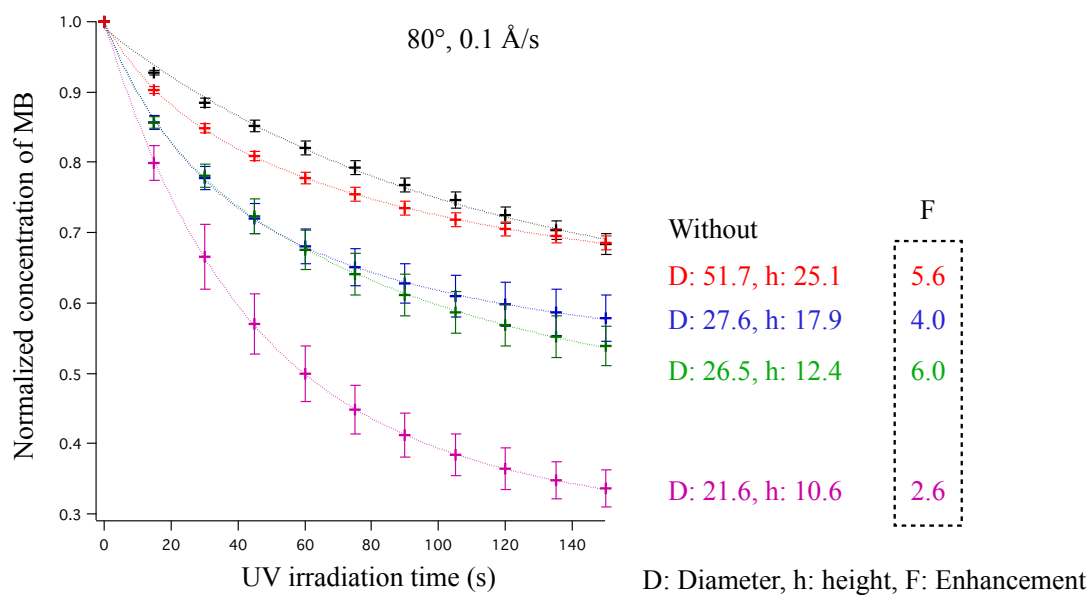


**Figure 4-10.** Photocatalysis with and without aluminum nanoparticles fabricated at the deposition rate of 0.1 Å/s and the tilt angle of 80 degrees. Dotted lines are fitted curves with using equation (3-4) and (3-5). Enhancement at each size of Al nanoparticles is shown in the dotted square.

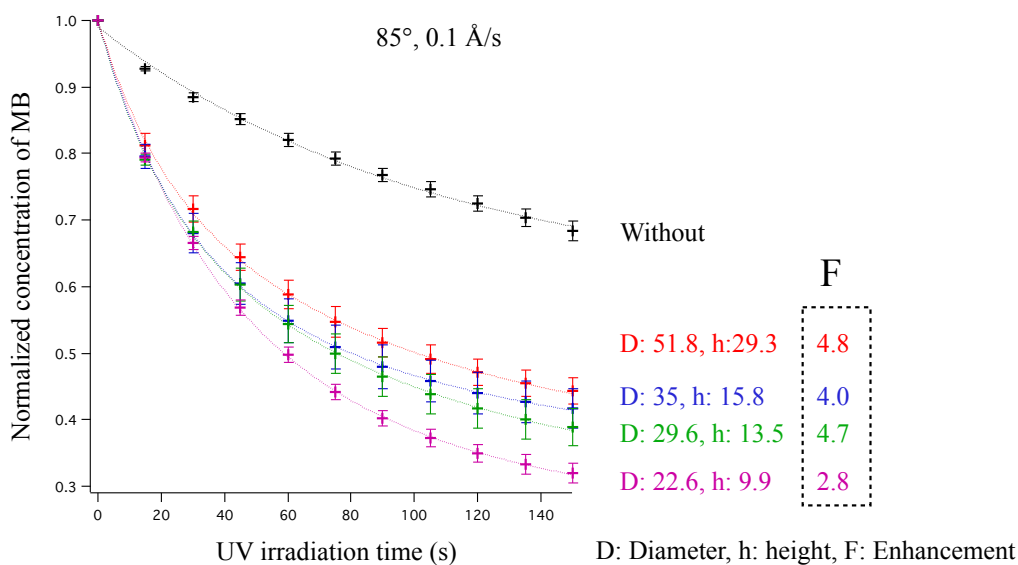


**Figure 4-11.** Photocatalysis with and without aluminum nanoparticles fabricated at the deposition rate of 0.1 Å/s and the tilt angles of 85 degrees. Dotted lines are fitted curves with using equation (3-4) and (3-5). Enhancement at each size of Al nanoparticles is shown in the dotted square.

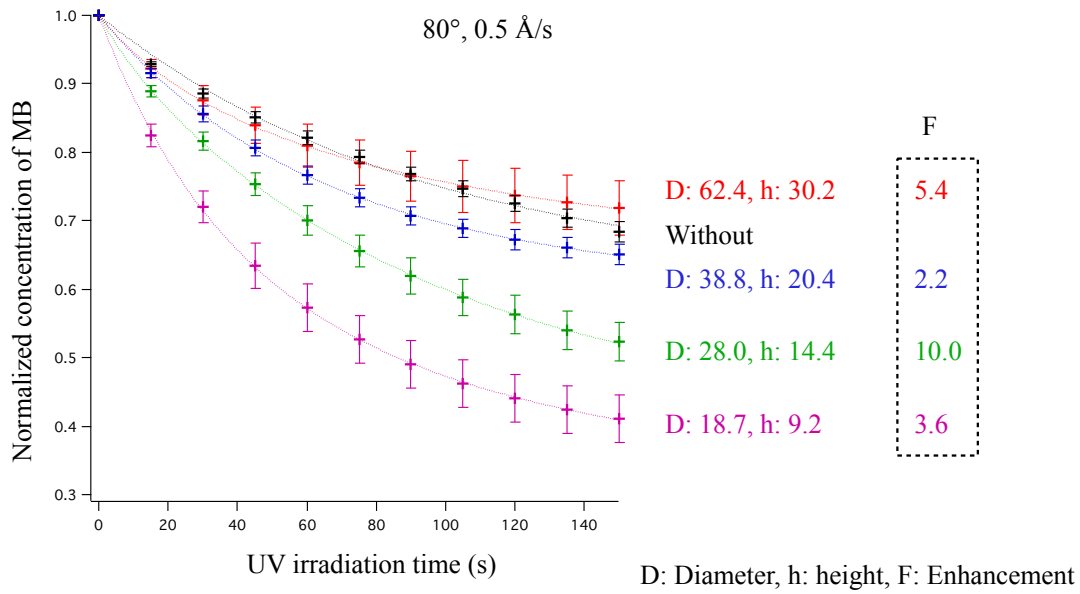


**Figure 4-12.** Photocatalysis with and without aluminum nanoparticles fabricated at the deposition rate of 0.5 Å/s and the tilt angle of 80 degrees. Dotted lines are fitted curves with using equation (3-4) and (3-5). Enhancement at each size of Al nanoparticles is shown in the dotted square.

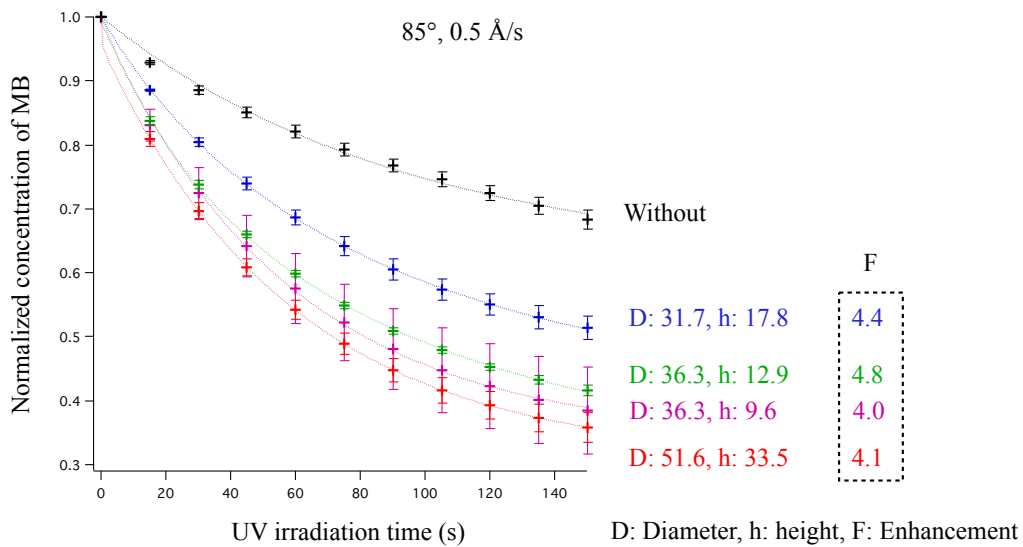


**Figure 4-13.** Photocatalysis with and without aluminum nanoparticles fabricated at the deposition rate of 0.5 Å/s and the tilt angle of 85 degrees. Dotted lines are fitted curves with using equation (3-4) and (3-5). Enhancement at each size of Al nanoparticles is shown in the dotted square.

### 4-3. Discussion of experimental results

Relationship between deposited volume of Al and enhancements are examined as shown in Figure 4-14. The values of enhancements,  $F$ , were obtained through curve fitting with using equation (3-5). The volume of deposited Al was calculated by multiplying deposition thickness by the sine of the inclined angle. The enhancement of reaction rates is not proportional to the volume of posited Al. This suggests contribution of chemical effects was negligible, which is reasonable from the viewpoint of oxidized layer at the Al's surface. Possible reasons of enhancement are two, localized field or multiple scattering.

The enhancement is mainly attributed to near-field enhancement. When plasmon resonance wavelength matches to the absorption edge of  $\text{TiO}_2$ , the maximum enhancement as large as 10 times was obtained. At the wavelength of the absorption edge of  $\text{TiO}_2$ , multiple scattering is impossible to occur because almost of scattering light are absorbed by  $\text{TiO}_2$  due to the skin depth of a few nanometers. As shown in Figure 4-14, when the size of Al nanoparticle is close to 28 nm that is the most efficient for plasmon excitation, enhancement took the maximum. Furthermore, this behavior is very similar with calculated results shown in Figure 2-11.

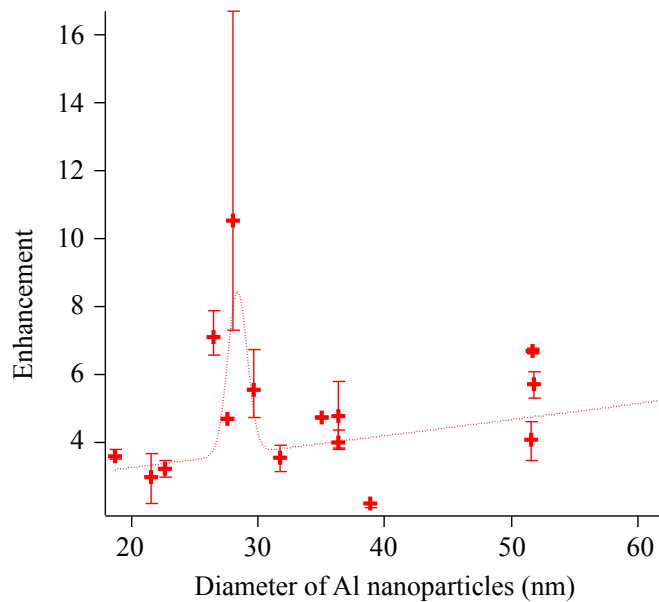
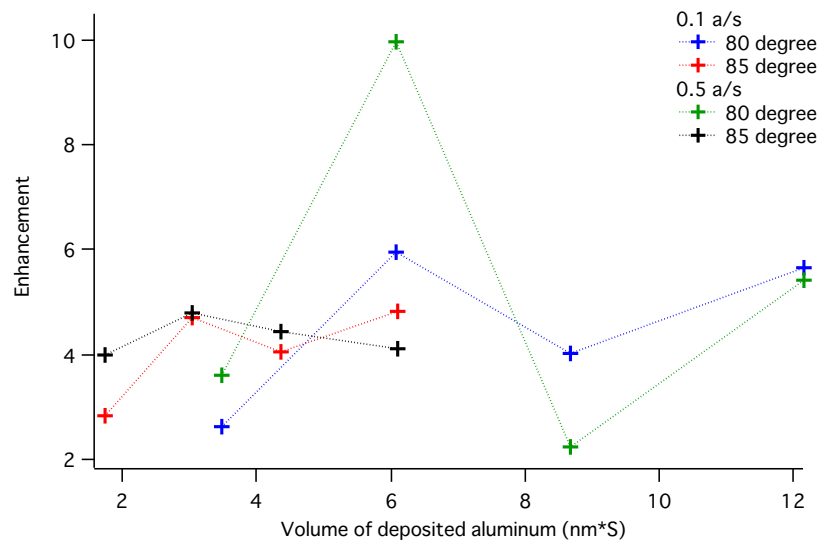


**Figure 4-14.** Relationship between the volume of deposited aluminum and enhancement (upper) and relationship between the diameter of Al nanoparticles and enhancement of the reaction rates (lower). In the left figure, marks are connected by dotted lines. In the right figure, the dotted curve represents fitted curve by a gauss function. S indicated in the left figure means the area of the substrate. Blue and red marks show enhancements with the condition of 80 and 85 degree of the tilt angle at the deposition rate of 0.1 Å/s. Blue and red marks show enhancements with the condition of 80 and 85 degrees of the inclined angle at the deposition rate of 0.5 Å/s.

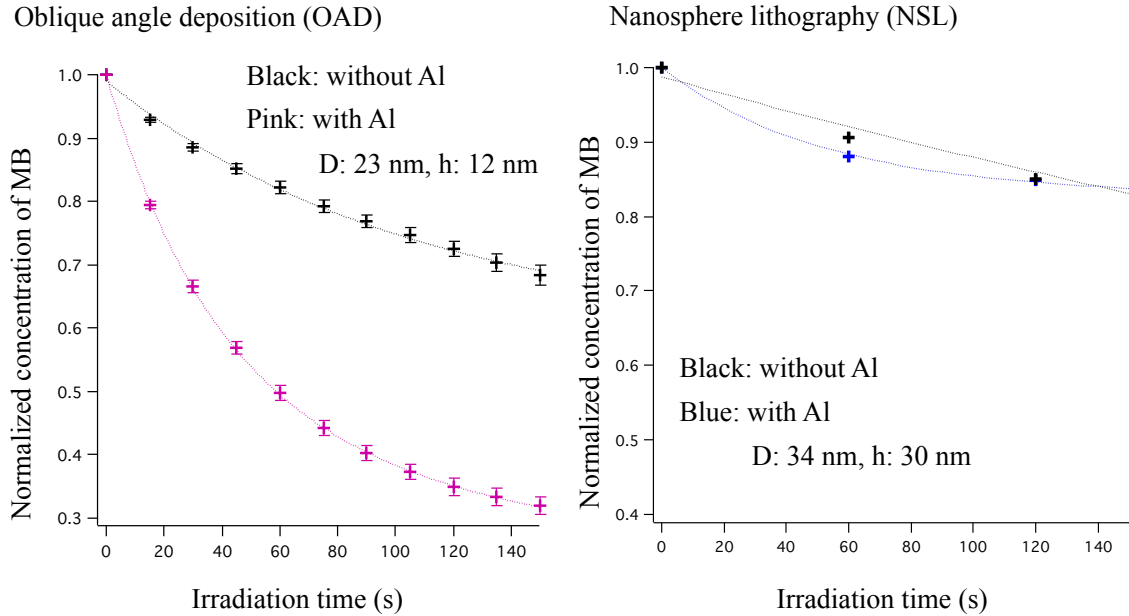


**Figure 4-15.** Photocatalytic reactions with and without aluminum nanoparticles fabricated by oblique angle deposition (OAD) (left) and Nanosphere lithography (NSL) (right)

Figure 4-15 displays photocatalytic reactions with and without aluminum nanoparticles. In Figure 4-15, aluminum nanoparticles are fabricated by OAD (left) and NSL (right). It is obvious that the amount of the product by photocatalysis increased with employing OAD. By NSL, single aluminum nanoparticles enhance photocatalysis higher than that by OAD because Al nanoparticles fabricated by NSL have much more sharp edges than those by OAD. Though the enhancement of single particles fabricated by OAD is slightly smaller than that by NSL, OAD brought higher activity. The densities of Al nanoparticles fabricated by NSL and ODA were  $1 \times 10^{14}/\text{m}^2$  and  $8 \times 10^{14}/\text{m}^2$ , respectively. Comparing ODA to NSL, the density and enhancement of reaction rates became  $\sim 8$  times larger and half. By these two effects, on the whole, production amount was considered to increase by  $\sim 4$  times, in OAD comparing to NSL.

I want to emphasize that photocatalysis with Al nanoparticles fabricated by OAD should be suitable for wide-filed applications. On the other hand, Al nanoparticles fabricated by NSL gave us the capability of photocatalytic reaction in local area. We need to select the way for fabrication of aluminum nanoparticles in concert with use.

## References

- [1] Y. He, J. Fu, Y. Zhao, "Oblique angle deposition and its applications in plasmonics", *Front. Phys.*, 9, 1, 47-59 (2014)
- [2] L. Abelmann, C. Lodder, "Oblique evaporation and surface diffusion", *Thin Solid Films*, 305, 1-21 (1997)
- [3] S.J. Jang, Y.M. Song, H.J. Choi, J.S. Yu, Y.T. Lee, "Structural and optical properties of silicon by tilted angle evaporation", *Surface & Coatings Technology* 205, S447–S450 (2010)
- [4] P. Negri, R.A. Dluhy, "Ag nanorod based surface-enhanced Raman spectroscopy applied to bioanalytical sensing", *Journal of Biophotonics*, 6, 1, 20–35 (2013)
- [5] C.L. Leverette, S.A. Jacobs, S. Shanmukh, S.B. Chaney, R.A. Dluhy, Y.P. Zhao, "Aligned Silver Nanorod Arrays as Substrates for Surface-Enhanced Infrared Absorption Spectroscopy", *Applied Spectroscopy*, 60, 8, 906-913 (2006)
- [6] Y.J. Jen, A. Lakhtakia, C.W. Yu, C.T. Lin, "Vapor-deposited thin films with negative real refractive index in the visible regime", *Optics Express*, 17, 10, 7784-7789 (2009)
- [7] D.A. Gish, F. Nsiah, M.T. McDermott, M.J. Brett, "Localized Surface Plasmon Resonance Biosensor Using Silver Nanostructures Fabricated by Glancing Angle Deposition", *Anal. Chem.*, 79, 11, 4228–4232 (2007)

## Conclusion and future perspective

In this research, enhancement of photocatalysis has been achieved with employing plasmons in UV range. The plasmon resonance wavelength at the absorption edge of  $\text{TiO}_2$  was found to be effective to enhance photocatalysis. I selected aluminum (Al) as a plasmonic material because the plasmon resonance wavelength is in UV range. In addition, the passive layer of  $\text{Al}_2\text{O}_3$  covers Al to protect from being damaged. In order to obtain aluminum nanoparticles, I firstly utilized nanosphere lithography (NSL), which is one of the conventional ways to produce Al nanoparticles. I obtained 244 nm of plasmon resonance wavelength by controlling particles' height. This is the shortest plasmon resonance wavelength achieved before. With Al nanoparticles, I experimentally confirmed that aluminum nanoparticles enhanced photocatalysis on  $\text{TiO}_2$ . The enhancement of reaction rates was  $\sim 14$  times. By simulations by discrete dipole approximation (DDA) method, it was found that the observed enhancements are attributed to plasmonic property of Al nanoparticles. Because Al nanoparticles are covered by passive layers, chemical effects are considered to be negligible. Furthermore, the number of Al nanoparticles increased by oblique angle deposition (OAD) method to increase the enhanced area. As a result, the amount of photoproduct increased by a factor of 4 while the enhancement of the reaction rate was 10 times. Though OAD decreased the reaction rate comparing to NSL, the amount of production increased. I emphasize that it's necessary to choose NSL or OAD to suit the use. When a plenty of production is required or reactants are placed for longer time on  $\text{TiO}_2$  surface, e.g.  $\text{H}_2$  production, OAD is better. When reactants circulate quickly, NSL is better.

In this dissertation, the plasmonic property of Al nanoparticles was suggested to affect the enhancement of photocatalysis. However, the enhancement mechanism is still not clear. To make it clear, experimental investigation is needed. For example, near-field mapping by scanning optical microscopy or surface-enhanced Raman scattering spectroscopy of  $\text{TiO}_2$  may reveal contribution of plasmonic effect. The quantitative evaluation of the enhancement also should be done. Furthermore, in the future, the enhancement of photocatalysis should be tested through hydrogen production or decomposition of toxic compounds because reaction rates depend on chemical species. Fabrication of dense aluminum nanoparticles is a key for the enhancement of not only photocatalysis but also sensitivity of gas- and bio-sensors.

# List of publications

## Original papers

1. **Mitsuhiro Honda**, Yuika Saito, Nicholas I Smith, Katumasa Fujita, Satoshi Kawata, "Nanoscale heating of laser irradiated single gold nanoparticles in liquid" *Optics Express*, vol. 19, pp.12375-12383 (2011)
2. Yuika Saito, **Mitsuhiro Honda**, Koichi Watanabe, Atsushi Taguchi, Yujian Song, and Satoshi Kawata,, "Design of Aluminum Nanostructures for DUV Plasmonics: Blue Shifts in Plasmon Resonance Wavelength by Height Control," *J. Jpn. Inst. Met.*, Vol. 77, No. 1, pp. 27-31 (2013).
3. **Mitsuhiro Honda**, Yasuaki Kumamoto, Atsushi Taguchi, Yuika Saito, Satoshi Kawata, "Plasmon-enhanced photocatalysis", *Applied Physics Letters*, 104, 061108 (2014)

## International conferences

1. **Mitsuhiro Honda**, Yuika Saito, Nicholas I Smith, Katsumasa Fujita, Satoshi Kawata, "Local temperature measurement of a laser-irradiated gold nanoparticle in liquid" *The 8th Asia-Pacific Workshop on Nanophotonics and Near-Field Optics (APNFO)* August 2011
2. **Mitsuhiro Honda**, Yuika Saito, Nicholas I Smith, Katsumasa Fujita, Satoshi Kawata , "Nanoscale Heating of Laser-irradiated Single Gold Nanoparticles" *4th International Symposium on Atomically Controlled Fabrication Technology* November 2011
3. **Mitsuhiro Honda**, Yuika Saito, Nicholas I Smith, Katsumasa Fujita, Satoshi Kawata, "Local temperature measurement of laser-irradiated single gold nanoparticles" *International Symposium on NanoPhotonics* December 2012

## **Domestic conferences**

1. Mitsuhiro Honda, Yuika Saito, Katsuya Ishitani, Prabhat Verma, Satoshi Kawata, "Photopolymerization of Fullerenes in and outside of SWNT" The Japan Society of Applied Physics, The 70th Autumn meeting September 2009
2. Mitsuhiro Honda, Yuika Saito, Nicholas I Smith, Satoshi Kawata, "Local temperature measurement of laser-irradiated gold nanoparticles by white light scattering spectroscopy", Annual meeting of the Spectroscopical Society of Japan November 2010

## Acknowledgements

I would like to express my deepest gratitude to **Prof. Satoshi Kawata**. His enormous support and insightful comments were invaluable during the course of my study. I learned not only the way to do research but also a personality as a scientist. He also taught me how to enjoy science and what science is. It's a great honor to study and learn science under Prof. Kawata. I believe that these experiences will be primary assets for me in the future.

My deepest appreciation goes to **Associate Prof. Yuika Saito**. I started to train under her supervising since I was a B4 student. She gave me thousands of favorable comments, suggestions, criticisms, and warm encouragements. Moreover, I learned experimental techniques, skills, and importance of conscientious effort and love for experimental instruments from her attitude.

I'd like to thank to **Prof. Yasushi Inouye**, **Prof. Yoshimasa Kawata**, and **Associate Prof. Dino Wilson Agerico Tan** for giving me so many useful comments and advices when I polished my dissertation.

I would like to thank **Dr. Yasuaki Kumamoto** for kind teaching and discussion both in my public and my private life. He shows great patience in helping me everytime with my research.

Special thanks also go to **Associated Prof. Katsumasa Fujita** for giving me insightful comments. Through talking with him, I learned correct and efficient communication. Also his interesting talk about ordinaries of life made my life in LaSIE happy.

I would like to thank **Assistant Prof. Satoru Shoji**. He gave me a lot of advices about how to attract the attention of Prof. Kawata.

I would like to express my gratitude to **Dr. Atsushi Taguchi** for giving me many advices in meeting.

I want to thank **Dr. Almar F. Palonpon** for correcting English in my paper. I enjoyed research life, thanks to his kindness.

I would like to show all my gratefulness to **Dr. Kyoko Masui** because she continuously supported me in all aspects since I was an undergraduate student. Her help and kindness always encouraged me. My presentation technique improved so much, thanks to her many advices.

I want to thank **Yoshito Okuno, Yasuo Yonemaru, Dr. Masaya Okada and Ryuji Shimomura** for their support and advice in my studies and life. Owing to their kind help, I had an invaluable experience at last in my private life. Such kind of experiences made me refresh and my research go well. In addition, it was so fun to talk about blue jokes with them. I had a very very good time in PhD course at Osaka University thanks to them.

I wish to thank **Soh Fujiwara** and **Kana Kobayashi** for helping my experiment. Even though we just spend a short time together, they have been very helpful.

I want to express my thanks to all members in LaSIE.

Finally I wish to record my sincere appreciation to my parents and the other families for their financial and mental support.

Mitsuhiro HONDA, December 2013